UNIVERSIDADE DE LISBOA
FACULDADE DE CIÊNCIAS
DEPARTAMENTO DE FÍSICA

Implementation of a Michelson Interferometer for Length Metrology

Renato Pires Alegria

Mestrado Integrado em Engenharia Física

Dissertação orientada por:
Prof. Dr. Alexandre Pereira Cabral

2022

Acknowledgements

First and foremost, I would like to thank my teacher and supervisor, Dr. Alexandre Cabral, for the guidance, dedication and patience, whose knowledge and vast experience were fundamental for the whole project.

I wish to express my sincere gratitude to the Instituto de Astrofísica e Ciências do Espaço for the unique opportunity to collaborate in the development of this project, it was truly an exceptional project and an incredible feat of engineering. I would also like to express my gratitude towards the team at the Laboratório de Ótica, Laser e Sistemas of the Department of Physics from the Faculty of Sciences of the University of Lisbon, for taking me in and helping with everything that was necessary. A special thanks to Dr. Manuel Abreu for his help in the many problems that surged.

To my colleagues with who I shared many of the problems that surged I thank them for their help and patience, above all to Inês Leite for introducing me to LabVIEW and for all the help in the laboratory.

Last but not least I would like to thank my parents, Filomena Alegria and João Alegria, for their relentless support through all these years and for motivating me to always keep moving forward.

Abstract

In optical instrumentation it is necessary to have an accurate knowledge of the performance of the tools used to displace and align optical components, particularly of translation stages, therefore a high accuracy calibration is fundamental. The objective of this thesis was to study, design, implement and test an optical metrology instrument capable of performing such high accuracy calibrations. The technique that guarantees high accuracy in the calibration of displacements is optical metrology with interferometry.

In order to achieve the objective of developing and building an interferometer the work was divided in several phases. We start with a brief review about the theory necessary to understand the functioning of an interferometer reviewing also the state of the art of interferometry, afterwards we study the uncertainty model to determine the requirements of the interferometer's components and of the ones to monitor atmospheric conditions. To finish the theoretical part of the work we define possible optical setups for the interferometer, concluding with the necessary signal processing.

Preceding the assembly of the interferometer a prototype was developed. During this phase a few problems were corrected and the displacement of a translation stage was analysed, then a 3D model of the interferometer was built, a crucial step for the following engineering part of the thesis. The system was calibrated, achieving an uncertainty level under 50 nanometers for displacements under 100 millimeters and 1 micrometer for displacements under 4 meters. Following the calibration of the system several tests were conducted that serve as an example to the possible uses of the measurement system.

The performance of the implemented system was capable of going beyond the initial requirements achieving an accuracy of:

$$U_d[\mathrm{m}] = (6.3{\times}10^{-9} + 2.7{\times}10^{-7}{\times}d)[\mathrm{m}] \tag{1}$$

It was also possible to perceive the importance of a high accuracy measurement system in the characterization of positioning systems.

Keywords: Length Metrology, Optics, Interferometry, Quadrature, Polarization

Resumo

Em instrumentação ótica é crucial ter um conhecimento exato não só da posição, mas também do deslocamento dos componentes óticos. As ordens de grandeza necessárias vão desde os milímetros até aos nanometros. De modo a posicionar e deslocar os componentes com a melhor exatidão e precisão possíveis não o podemos fazer à mão, é necessário recorrer a mesas de translação. Existem inúmeros tipos de mesas de translação motorizadas com gamas de funcionamento diferentes, para deslocamentos inferiores ao milímetro as mesas de translação recorrem a elementos piezoelétricos e para deslocamentos superiores ao milímetro as mesas de translação recorrem a motores de passo ou de corrente contínua.

O principal problema destes instrumentos é a falta de conhecimento sobre as suas verdadeiras capacidades. Muitas das vezes o fabricante atribui uma incerteza ao modelo de mesas de translação que oferece, contudo, esta incerteza representa o pior dos casos possível o que significa que o produto adquirido pode ter melhor desempenho. Para resolver este problema e conhecer corretamente o comportamento de uma mesa de translação é necessário realizar uma calibração. Para além de fundamentais para as mesas de translação, as calibrações também beneficiam outros instrumentos óticos, tais como os sensores de deslocamento. Estes sensores também são genericamente caracterizados pelo fabricante, portanto sofrem do mesmo problema que as mesas de translação. Para tirar partido de todo o potencial de um sensor de deslocamento será necessário, mais uma vez, realizar uma calibração.

Visto que as calibrações são um aspeto recorrente surge a necessidade de ter um instrumento capaz de as realizar. Existem imensas maneiras de obter deslocamentos pequenos, é possível atingir o regime dos nanometros com, por exemplo, sensores capacitivos ou piezoelétricos, no entanto a gama dinâmica destes sensores é bastante limitada, a técnica que tem a maior gama dinâmica e é frequentemente utilizada em metrologia de precisão é a interferometria. Hoje em dia existem várias técnicas e inúmeras configurações possíveis em interferometria, o que nos permite ajustar o sistema de medição de acordo com as nossas necessidades, otimizando o desempenho do interferómetro e mantendo a complexidade do sistema o menor possível.

De acordo com a uso típico de mesas de translação em projetos de instrumentação em astrofísica e considerando as mesas de translação disponíveis no mercado, definiram-se os requisitos de incerteza que o interferómetro tem de cumprir. De modo a construir um interferómetro que cumpra os objetivos propostos este trabalho foi dividido em sete partes distintas.

Na primeira parte a interferometria é introduzida, em seguida abordamos a relevância de cadeias de rastreabilidade e passamos para a revisão dos conceitos básicos da radiação eletromagnética que nos permitem compreender o fenómeno da interferência, tal como a equação do campo elétrico e as diferentes polarizações que este campo pode ter. Uma vez abordada a radiação eletromagnética introduzimos a notação de Jones de modo a facilitar a manipulação das várias equações necessárias, o que nos vai finalmente levar à explicação da interferência e às condições necessárias para que aconteça. Para concluir

revemos o estado da arte das três componentes fundamentais de um interferómetro: a fonte de luz utilizada, o índice de refração do ar e o tipo de deteção do interferómetro, atribuindo especial atenção a este último aspeto.

Na segunda parte é abordado o problema da incerteza do modelo introduzido previamente, o que implica a definição dos requisitos mínimos para a incerteza dos três módulos do interferómetro. A fonte de luz é limitada pelo comprimento de coerência e definimos que necessitamos de um laser de He-Ne estabilizado. Quanto ao índice de refração e ao modulo de deteção fazemos um balanço de incerteza de modo a equilibrar a incerteza destas duas componentes de igual forma, o que nos leva a concluir que para o modulo de deteção necessitamos de quadratura. Relativamente ao índice de refração obtemos as incertezas com que temos de determinar as suas três componentes: a pressão, a temperatura e a humidade relativa do ar.

Na terceira parte estudamos a quadratura. Após definido o método de deteção existem várias configurações possíveis para o interferómetro, pelo que quatro configurações relevantes são analisadas e em seguida comparadas de acordo com as suas vantagens e desvantagens. No final a escolha da melhor configuração não passa só por uma questão ótica, mas também mecânica, uma vez que as componentes têm de ser posicionadas e ajustadas manualmente e todos estes alinhamentos são complexos.

Na quarta parte analisamos o processamento de sinal necessário para extrair a diferença de fase dos dois feixes que estão em quadratura. Começamos por caracterizar e corrigir os sinais detetados, em seguida explicamos como não é necessário ter uma diferença de fase de 90° para obtermos a quadratura e passamos para a otimização de alguns aspetos do processamento de sinal explicado inicialmente. Para concluir abordamos o processo do desdobramento da fase e as implicações que este tem na frequência de amostragem.

Na quinta parte realizamos a montagem do interferómetro. Começamos por testar o modelo com um protótipo, o que nos permitiu concluir que as retrorreflexões e a divergência do laser eram um problema. De modo a corrigir as retrorreflexões introduzimos um isolador de Faraday na montagem e quanto à divergência do laser utilizamos um expansor de feixe. Após ter corrigido estes dois problemas testámos o protótipo com uma mesa de translação para verificar se o processamento de sinal estava corretamente implementado, os resultados obtidos indicam que os problemas que surgem devido ao processamento de sinal eram mínimos e tratamos de os corrigir de imediato. Em seguida passamos para o desenho do interferómetro a montar, entre os vários esquemas que consideramos escolhemos o que facilitava a montagem e otimizava a área disponível para o posicionamento os componentes. Nesta fase percebemos também como lidar com diversos problemas da montagem tal como o facto do feixe passar duas vezes pelo polarizador e o posicionamento do divisor de feixe polarizado no seu suporte. Após definir um esquema realizou-se um modelo 3D em SolidWorks para visualizar melhor a montagem e o posicionamento de cada componente. Quanto à montagem abordamos duas técnicas de alinhamento de feixes laser e concluímos com uma explicação detalhada do posicionamento de cada componente no interferómetro. Finalmente explicamos uma implementação simplificada do processamento de sinal utilizado em LabVIEW.

A sexta parte compreende não só a calibração do interferómetro, mas também a sensibilidade do sistema a perturbações exteriores. Relativamente à sensibilidade do interferómetro percebemos que o sistema de estabilização da mesa utilizada é ótimo na atenuação dos ruídos exteriores e concluímos também que as condições ideais para a realização da calibração seriam durante a noite pois desejamos estar nas melhores condições possíveis para compreender os limites de funcionamento do interferómetro. Verificamos também que existe alguma deriva no sistema, no entanto os valores obtidos não excediam meia franja, contudo é prudente que as medições sejam efetuadas no menor intervalo de tempo possível. Quanto à calibração do interferómetro concluímos que a menor incerteza possível do instrumento é de

$6.2\,\mathrm{nm}$, no entanto este valor foi limitado pela mesa de translação utilizada para a calibração. Com a calibração verificamos que estas incertezas são melhores do que os requisitos propostos no início e conseguimos obter a incerteza do interferómetro para qualquer deslocamento que pode ser aproximada pelo seguinte ajuste linear:

$$U_d[\mathrm{m}] = (6.3{\times}10^{-9} + 2.7{\times}10^{-7}{\times}d)[\mathrm{m}] \tag{2}$$

Para concluir, na sétima parte o interferómetro foi utilizado na calibração de várias mesas de translação. Estas calibrações passam primeiro pela determinação da repetibilidade da origem e em seguida pela repetibilidade de deslocamentos ao longo do percurso das mesas de translação. Uma vez que o erro de deslocamento é conhecido (e linear) podemos corrigi-lo ao ajustar o fator de conversão tensão/deslocamento dos controladores das mesas, otimizando assim o desempenho destas para condições ainda melhores que as especificadas pelo fabricante.

Palavras-chave: Metrologia de Comprimento, Ótica, Interferometria, Quadratura, Polarização

Contents

List of Figures

List of Tables

List of Abbreviations, Acronyms and Symbols

Abbreviations and Acronyms

BIPM	*Bureau International des Poids et Mesures*
BS	Beamsplitter
DAQ	Data Acquisition
DC	Direct Current
ESA	European Space Agency
IA	*Instituto de Astrofísica e Ciências do Espaço*
L-45P	Linear -45° Polarization
L+45P	Linear +45° Polarization
LC	Laser Cavity
LCP	Left Circular Polarization
LHP	Linear Horizontal Polarization
LVP	Linear Vertical Polarization
meas	Relative to the measurement arm of the interferometer
OA	Optical Axis
obt	Obtained
OPD	Optical Path Difference
PBS	Polarizing Beamsplitter
PI	Physik Instrumente
POL	Polarizer

RCP . . . . Right Circular Polarization

ref . . . . Relative to the reference arm of the interferometer

req . . . . Required

RR . . . . Retroreflector

SI . . . . International System of Units

SN . . . . Serial Number

WF . . . . Wavefront

WP . . . . Waveplate

Symbols

Sign	Description	Unit
α	Quadrature phase offset to the desired 90°	°
δ	Phase corresponding to the OPD between both arms of the interferometer	rad
δ_u	Unwrapped value of δ	rad
$\Delta\nu_{Cs}$	Caesium frequency	Hz
$\Delta\phi$	Phase difference between both components of the electric field	°
$\Delta\varphi$	Phase difference between the electric fields of both interferometer arms	°
ε_0	Vacuum permittivity	F/m
ϵ	Least squares residual	–
η	Angle between an optical component axis and the x axis	°
θ	Laser beam divergence	rad
λ	Wavelength	m
ξ	Type of waveplate retardation applied	rad
σ	Standard deviation	–
ϕ	Initial phase of the electric field	°
ψ	Net electric field angle with the x axis	–
ω	Angular frequency	rad/s
a	Acceleration	$\mathrm{m/s^2}$
B, C, D, E, F	Elliptical fit parameters obtained by the least square method	–
c	Speed of light in vacuum	m/s
d	Displacement	m
d'	Distance	m

Sign	Description	Unit
E	Electric Field	$\mathrm{V/m}$
f	Frequency	Hz
f_s	Sampling frequency	Hz
I	Irradiance	$\mathrm{W/m^2}$
$\boldsymbol{j}_{ij}$	Jones matrix element $\boldsymbol{j}$ corresponding to i column and j row	–
J	Jones matrix	–
k	Wave number	$\mathrm{m^{-1}}$
L_c	Coherence length	m
n	Refractive index of air	–
N_f	Number of fringes	–
N	Number of total samples acquired	–
p	Voltage offset of the detected x polarization	V
P	Ambient pressure	kPa
q	Voltage offset of the detected y polarization	V
$\vec{\mathrm{r}}$	Position vector	m
r	Gain ratio between both detectors	–
R	Amplitude of a sinusoidal wave	–
R'	Radius of curvature of a wavefront	–
RH	Ambient relative humidity	$\%$
T	Ambient temperature	$^\circ\mathrm{C}$
t	Time	s
U	Expanded uncertainty corresponding to a 95% confidence interval (k=2) [1]	–
v	Velocity	$\mathrm{m/s}$
V	Ideally detected voltage	V
V^d	Detected voltage	V
V^c	Corrected voltage	V
x, y, z	Cartesian coordinates	m

Chapter 1

Introduction

1.1 Motivation

In optical instrumentation it is crucial to have a very accurate knowledge of the position and the displacement of optical components, the orders of magnitude necessary range from the millimeters to the nanometers, one million times smaller. To effectively place and move components with such high accuracies it is necessary to resort to motorized translation stages, instruments that have multiple operating ranges. For sub-millimetric displacements the stages use piezoelectric elements that expand or contract to cause a displacement, while for super-millimetric displacements the translation stages use stepper or DC motors.

The primary obstacle when using any translation stage is the lack of knowledge about it's specifications, usually the manufacturer will attribute an uncertainty to a model of translation stages even though this uncertainty represents the "worst case scenario" and the product acquired can have a better performance. To resolve this problem and better estimate the uncertainty of the acquired instrument it is necessary to calibrate the stage. Besides translation stages, displacement sensors aren't optimally characterized by the manufacturers, to take full advantage of the sensor's measuring capabilities and reach the maximum performance possible the information indicated by the manufacturer is never enough, a calibration must be performed.

Considering calibrations are a fundamental aspect of displacement measurements, there arises the need to have an instrument capable of performing such tasks. There are many ways to perform sub-millimetric displacement measurements, it is possible to reach the nanometer regime using, for example, capacitive sensors or piezoelectric sensors, among many other options [2], however the dynamic range of these instruments is very limited. The technique that has the largest dynamic range and is widely used in precision metrology is interferometry.

There already exist countless possible interferometer configurations and that allows us to tailor the measurement system to our needs in order to optimize the instrument's performance while keeping the complexity as small as possible. The innovation provided by this work is not a new interferometry method but a detailed study of the theory, system modelling and uncertainty determination in order to build the best possible interferometer according to our needs.

1.2 Objectives

In light of the typical usage of translation stages in projects related to instrumentation in astrophysics, particularly in the instrumentation group of the *Instituto de Astrofísica e Ciências do Espaço* (IA), and taking into consideration the uncertainty of typical translation stages provided by regular suppliers [3, 4], the uncertainty requirements for the interferometer were defined and are present in table 1.1 and represented in figure 1.1. In uncertainty and traceability chains it is common to consider a margin of an order of magnitude between the uncertainty of the measurement instrument and the equipment to calibrate so the requirements defined were set accordingly.

Table 1.1: Uncertainty requirements for the interferometer, one decade smaller than the working range of the average translation stage used in astronomy and astrophysics.

Displacement [mm]	0.1	0.5	10	25	100	500	1000	4000
Uncertainty [μm]	0.01	0.025	0.01	0.025	0.1	0.5	1	5

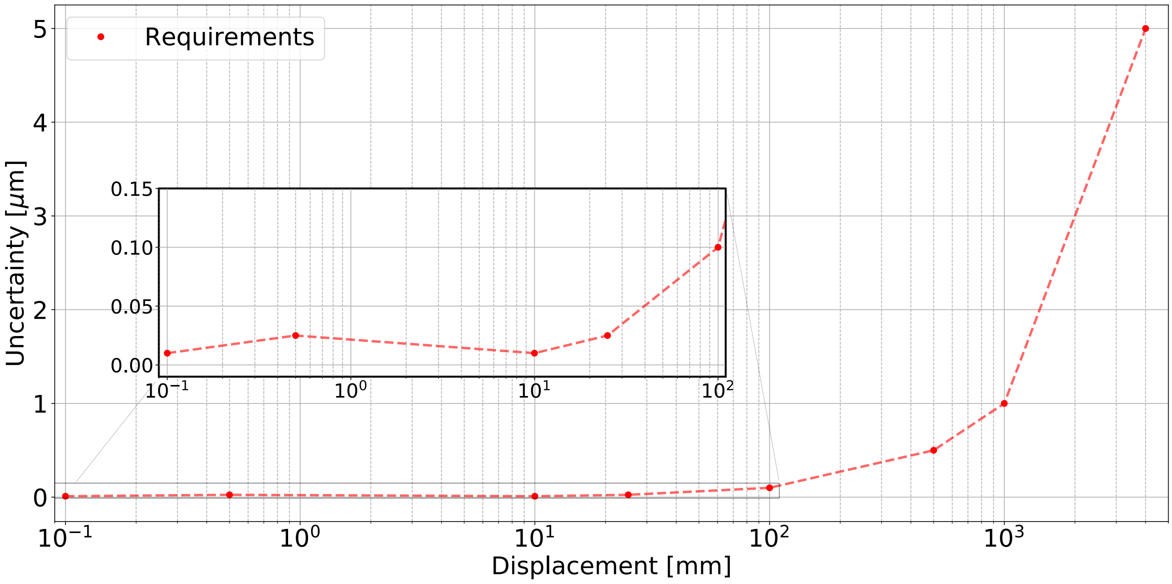

Figure 1.1: Graphical representation of the uncertainty requirements for the interferometer, present in table 1.1.

In order to build an interferometer that complied with the uncertainty requirements of table 1.1 several steps were required, ranging from the study of the physics of interferometry to the engineering of the system comprising the design, integration, assembly and testing. This thesis reflects every stage required to build the interferometer.

1.3 Structure

This work is organized in 9 chapters:

- ▷ **Chapter 1 -** Introduction

  Thesis motivation, objectives and structure.

- ▷ **Chapter 2 -** Interferometry

  Brief review about fundamental concepts of interferometry.

- ▷ **Chapter 3 -** Uncertainty Model for Length Measurements with a Michelson Interferometer

  Study about the uncertainty model for a Michelson interferometer and estimation of the necessary uncertainties to comply with the requirements.

- ▷ **Chapter 4 -** Evaluation of Optical Configurations

  Comparison of multiple optical configurations and definition of the one to be assembled.

- ▷ **Chapter 5 -** Signal processing

  Detailed explanation of the signal processing necessary to calculate the displacement.

- ▷ **Chapter 6 -** System Design, Implementation and Integration

  Preliminary studies performed on a prototype followed by the assembly of the final interferometer with a brief overview of an implementation of the signal processing in LabVIEW.

- ▷ **Chapter 7 -** Interferometer Calibration

  Interferometer sensitivity to external perturbations and calibration.

- ▷ **Chapter 8 -** Translation Stage Calibration

  Calibration of the homing mechanism and displacement of multiple translation stages.

- ▷ **Chapter 9 -** Conclusions

  Important aspects of all the work done.

Chapter 2

Interferometry

Interferometry, as the name suggests, is a technique used to measure based on the interference phenomenon, in this case displacements will be measured. Interference takes place when two coherent waves overlap and interact with each other, in this work the interference between two electromagnetic waves was studied.

2.1 Michelson's Interferometer

When trying to prove the existence of a medium for light to propagate, the famous ether [5], Michelson developed an interferometer that would later inherit his name. This was the first interferometer developed used later for displacement metrology and the principle of operation is still the same that is currently used.

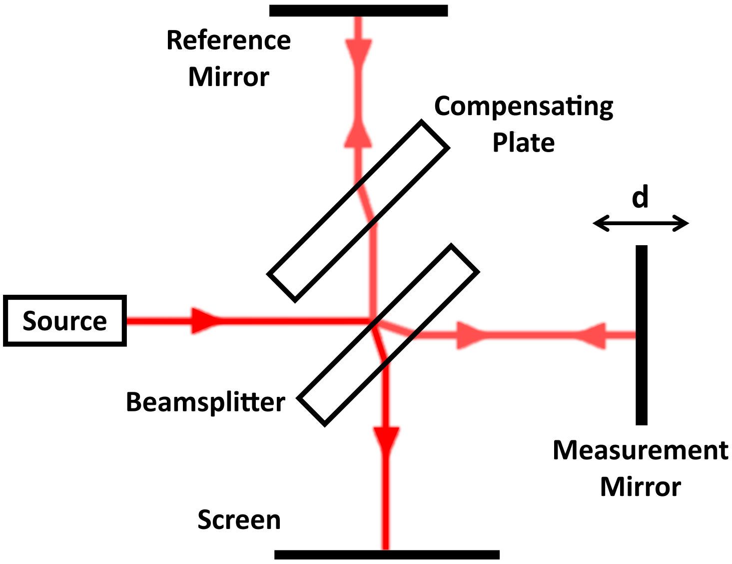

Figure 2.1: Michelson's interferometer schematic.

Although the physics behind interferometry is detailed in section 2.6 we can see in figure 2.1 that by splitting the light beam into two different paths, Michelson controlled the phase difference of the two beams by displacing one of the mirrors. It is possible, according to equation 2.19, to know the phase difference by counting the number of fringes displayed on the screen. This conclusion yields an equation that relates the mirror's displacement with the number of fringes:

$$d = \frac{\Delta\varphi}{2\pi}\frac{\lambda}{2n} = \frac{N_f}{2}\frac{\lambda}{n} \tag{2.1}$$

Where d represents the displacement of the mirror, $\Delta\varphi$ the phase difference between the electric fields of both interferometer arms, λ the wavelength of the laser source in use, n the refractive index of air and N_f the number of fringes displayed on the screen.

It is important to note that using this method only relative displacements can be measured, absolute measurements are impossible with this approach.

2.2 Traceability

In order for the measurements performed with interferometry to be universally acceptable, they need to be traceable to the International System of Units (SI). The *Bureau International des Poids et Mesures*, BIPM, is responsible for defining and maintaining the units of the SI and has defined the unit of length, the meter, as:

"The fixed numerical value of the speed of light in vacuum c to be 299 792 458 when expressed in the unit $\mathrm{m\,s^{-1}}$*, where the second is defined in terms of the caesium frequency* $\Delta\nu_{Cs}$*"*[6]

Considering that the meter is defined by the speed of light and it is possible to relate the speed of light to the wavelength of a laser using $c = \lambda f$, any interferometer can perform a traceable measurement by knowing the wavelength of the radiation source in use [7], as the speed of light has no uncertainty [8].

2.3 Electromagnetic Radiation

Nowadays it is known that visible light is only a small part of the electromagnetic spectrum, specifically corresponding to the radiation with a wavelength between 380 nm and 750 nm. It is composed of an electric and a magnetic field oscillating orthogonally to the axis of propagation, which implies that light is a traverse wave. Although both fields propagate together it is usually enough to refer only the electric field [9], which as proved by Arago and Fresnel, is composed of two orthogonal components that do not interfere [10]. It follows that the electric field of a light wave propagating along the z axis has both x and y components.

To obtain an equation for the electric field it is necessary to solve the wave equation:

$$\nabla^2\vec{\mathrm{E}}(\vec{\mathrm{r}}, t) = \frac{1}{c^2}\frac{\partial^2\vec{\mathrm{E}}(\vec{\mathrm{r}}, t)}{\partial t^2} \tag{2.2}$$

Although the electric field is a real quantity it is often convenient to express the solution using a complex notation, so we have the following expressions for one component of the electric field vector:

$$E_x = \mathrm{Re}\left[E_{0x}e^{i(\omega t - \vec{\mathrm{k}}\cdot\vec{\mathrm{r}} + \phi_x)}\right] = E_{0x}\cos(\omega t - \vec{\mathrm{k}}\cdot\vec{\mathrm{r}} + \phi_x) \tag{2.3}$$

Another important aspect of the wave equation is linearity. Due to this property we can conclude that the electric field obeys the superposition principle, that is, the sum of two solutions is also a valid solution, which means the total electric field can be composed of multiple superposed electric fields.

2.4 Polarization

Polarization is a property of traverse waves, it indicates the direction in which the net electric field oscillates. As was studied in Chapter 4, polarization plays a very important role in interferometry.

When dealing with multiple superposed waves one can say light is not polarized since there is no apparent pattern to the net electric field oscillations, but when dealing with one single electromagnetic wave there are few possibilities for the polarization, these are called degenerate polarization states:

$\rightarrow$ $E_x = 0$ **or** $E_y = 0$

If the electric field has only one component then the polarization can be either vertical (figure 2.2a) or horizontal (figure 2.2b).

$\rightarrow$ $E_{0x} \neq 0$ **and** $E_{0y} \neq 0$ **and** $\Delta\phi \in \{0°; 180°\}$

If both components exist and are in phase then the polarization will have a certain degree (figure 2.2c). There is the particular case when both fields have the same amplitude (figure 2.2d).

$\rightarrow$ $E_{0x} = E_{0y} \neq 0$ **and** $\Delta\phi \in \{-90°; +90°\}$

If both components have the same amplitude and the phase difference is either $-90°$ or $+90°$ the polarization is left circular (figure 2.2e) or right circular (figure 2.2f), respectively.

When none of the above cases apply we are left with elliptical polarization:

$\rightarrow$ $E_{0x} = E_{0y} \neq 0$ **and** $\Delta\phi \notin \{-90°; +90°\}$ **;** $E_{0x} \neq E_{0y} \neq 0$ **and** $\Delta\phi \notin \{0°; 180°\}$

If the amplitudes are equal but the phase difference is not $\pm 90°$ the polarization will be elliptical with a tilt (figure 2.2g). Otherwise if the amplitudes are different and the phase difference is neither 0° nor 180° the polarization will always be elliptical (figure 2.2h), with or without a tilt.

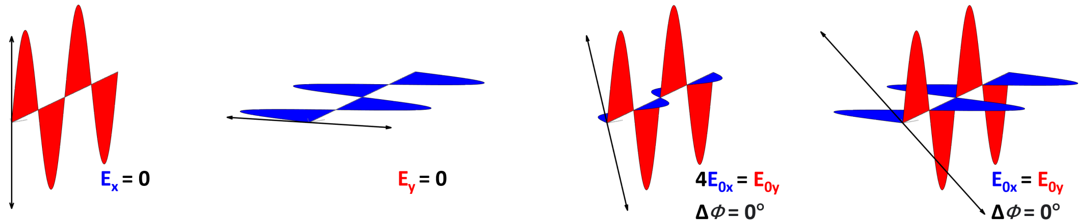

(a) Vertical polarization. (b) Horizontal polarization. (c) -76° polarization. (d) -45° polarization.

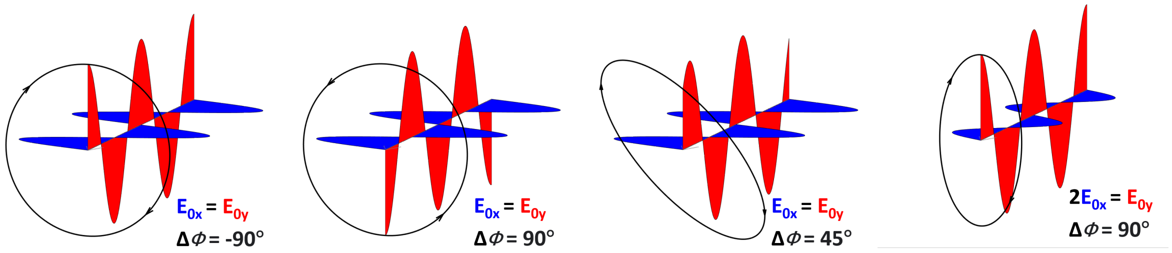

(e) Left circular polarization. (f) Right circular polarization. (g) Elliptical polarization with 45° phase difference. (h) Elliptical polarization with different amplitudes.

Figure 2.2: Electric field polarizations.

The polarization of the electric field can be changed in two different ways, either by filtering the desired linear polarization with a polarizer or by delaying one component of the electric field with a waveplate.

Polarizers are essential when dealing with non-polarized electric fields because the transmitted electric field will only have the components aligned with the polarizer's axis, this means these components can also be used to filter linear polarizations from circularly or elliptically polarized electric fields. Polarizers operate either by absorbing the electric fields not aligned with its axis, or by splitting the two polarization components spatially by means of a reflection.

Waveplates are useful when the electric field is already polarized. In addition to being the main tool to achieve circular or elliptical polarizations these components also allow rotations of linear polarizations without the losses of a polarizer. There are different types of waveplates varying on the delay given to the polarizations, half waveplates are used to rotate linear polarization while quarter or octadic waveplates are used to delay one component of the electric field, delay which depends on the angle between the optical axis and the waveplate's fast and slow axis.

2.5 Jones Notation

When characterizing any optical setup it is convenient to use a proper notation to facilitate the calculations. Several notations have been developed, however, considering the radiation in study is completely polarized and coherent, Jones Notation was used [11].

In Jones matrix calculus the electric field vector is represented by a 2×1 matrix, where the (1,1) component is the x electric field and the (2,1) component is the y electric field:

$$\vec{\mathrm{E}} = \begin{bmatrix} E_x \\ E_y \end{bmatrix} = \begin{bmatrix} E_{0x}e^{i\phi_x} \\ E_{0y}e^{i\phi_y} \end{bmatrix} = \begin{bmatrix} E_{0x} \\ E_{0y}e^{i\Delta\phi} \end{bmatrix} \tag{2.4}$$

Any optical component is represented by a 2×2 matrix, with each $\boldsymbol{j}_{ij}$ element depending on the type of component:

$$\mathbf{J} = \begin{bmatrix} \boldsymbol{j}_{11} & \boldsymbol{j}_{12} \\ \boldsymbol{j}_{21} & \boldsymbol{j}_{22} \end{bmatrix} \tag{2.5}$$

When light passes through the optical component the resulting electric field vector is given by the left multiplication of the component matrix by the incident electric field vector:

$$\vec{\mathrm{E}}_{\mathrm{out}} = \mathbf{J}\vec{\mathrm{E}}_{\mathrm{in}} \tag{2.6}$$

If light passes through multiple components, for example components 1, 2 and 3 with Jones matrices $\mathbf{J_1}$, $\mathbf{J_2}$ and $\mathbf{J_3}$, respectively, the resulting electric field vector after all three components is given by:

$$\vec{\mathrm{E}}_{\mathrm{out}} = \mathbf{J_3}\mathbf{J_2}\mathbf{J_1}\vec{\mathrm{E}}_{\mathrm{in}} \tag{2.7}$$

Usually the electric field vectors and the Jones matrices are normalized, thus the electric field vector is given by:

$$\vec{\mathrm{E}}(\psi, \Delta\phi) = \begin{bmatrix} \cos\psi \\ e^{i\Delta\phi}\sin\psi \end{bmatrix} \tag{2.8}$$

Where ψ is the angle between the x axis and the net electric field (ignoring the phase difference) and $\Delta\phi$ is the phase difference between both components of the electric field, defined as:

$$\Delta\phi = \phi_y - \phi_x \tag{2.9}$$

Using equation 2.8 we can calculate the Jones vectors for the degenerate polarization states:

$$\vec{\mathrm{E}}_{\text{LHP}} = \begin{bmatrix} 1 \\ 0 \end{bmatrix} \qquad \vec{\mathrm{E}}_{\text{L+45P}} = \frac{1}{\sqrt{2}} \begin{bmatrix} 1 \\ 1 \end{bmatrix} \qquad \vec{\mathrm{E}}_{\text{L-45P}} = \frac{1}{\sqrt{2}} \begin{bmatrix} 1 \\ -1 \end{bmatrix}$$

$$\vec{\mathrm{E}}_{\text{LVP}} = \begin{bmatrix} 0 \\ 1 \end{bmatrix} \qquad \vec{\mathrm{E}}_{\text{RCP}} = \frac{1}{\sqrt{2}} \begin{bmatrix} 1 \\ i \end{bmatrix} \qquad \vec{\mathrm{E}}_{\text{LCP}} = \frac{1}{\sqrt{2}} \begin{bmatrix} 1 \\ -i \end{bmatrix}$$

The Jones matrix for a linear polarizer at an η angle with the x axis is:

$$\mathbf{J}_{\text{POL}}(\eta) = \begin{bmatrix} \cos^2\eta & \sin\eta\cos\eta \\ \sin\eta\cos\eta & \sin^2\eta \end{bmatrix} \tag{2.10}$$

The Jones matrix for any type of waveplate with its fast axis at an η angle with the x axis is:

$$\mathbf{J}_{\text{WP}}(\eta;\xi) = \begin{bmatrix} \cos\frac{\xi}{2} + i\sin\frac{\xi}{2}\cos 2\eta & i\sin\frac{\xi}{2}\sin 2\eta \\ i\sin\frac{\xi}{2}\sin 2\eta & \cos\frac{\xi}{2} - i\sin\frac{\xi}{2}\cos 2\eta \end{bmatrix} \tag{2.11}$$

Where the type of waveplate is defined by the ξ parameter. For a half waveplate we have $\xi = \pi$, for a quarter waveplate $\xi = \pi/2$ and for an octadic waveplate $\xi = \pi/4$.

The Jones matrix for an ideal 50/50 beamsplitter is:

$$\mathbf{J}_{\text{BS}} = \frac{1}{\sqrt{2}} \begin{bmatrix} 1 & 0 \\ 0 & 1 \end{bmatrix} \tag{2.12}$$

For an ideal polarizing beamsplitter we have two different Jones matrices, one for each output beam:

$$\mathbf{J}_{\text{PBS}_x} = \begin{bmatrix} 1 & 0 \\ 0 & 0 \end{bmatrix} \qquad \mathbf{J}_{\text{PBS}_y} = \begin{bmatrix} 0 & 0 \\ 0 & 1 \end{bmatrix} \tag{2.13, 2.14}$$

Finally, it is also possible to express the phase difference corresponding to the optical path difference of light (δ):

$$\mathbf{J}_{\text{OPD}} = e^{i\delta} \begin{bmatrix} 1 & 0 \\ 0 & 1 \end{bmatrix} \tag{2.15}$$

2.6 Interference and Irradiance

Interference is a phenomenon and cannot be measured directly, it does nonetheless affect the irradiance of the electromagnetic radiation, defined as the radiant energy flux per unit area ($\mathrm{W/m^2}$):

$$I = \frac{c\varepsilon_0}{2} |\vec{\mathrm{E}}_{\text{net}}|^2 \tag{2.16}$$

If the net electric field is composed of two superposed electric fields we have from equation 2.16:

$$I = \frac{c\varepsilon_0}{2} |\vec{\mathrm{E}}_1 + \vec{\mathrm{E}}_2|^2 = \frac{c\varepsilon_0}{2} (|\vec{\mathrm{E}}_1|^2 + |\vec{\mathrm{E}}_2|^2 + 2\vec{\mathrm{E}}_1 \cdot \vec{\mathrm{E}}_2) \tag{2.17}$$

In the last term of equation 2.17 we can express the dot product as:

$$\vec{\mathrm{E}}_1 \cdot \vec{\mathrm{E}}_2 = |\vec{\mathrm{E}}_1||\vec{\mathrm{E}}_2| \cos(\Delta\varphi) \tag{2.18}$$

Simplifying equation 2.17 with equation 2.18 yields:

$$I = I_1 + I_2 + 2\sqrt{I_1 I_2}\,\cos(\Delta\varphi) \tag{2.19}$$

The last term of equation 2.19 is designated interference term due to its dependence on the phase difference between both overlapped electric fields. Varying this phase difference it is possible to obtain a minimum and a maximum of irradiance, each minimum-maximum pair correspond to a fringe.

Using Jones notation the irradiance can be calculated (aside from constants) by:

$$I = \vec{\mathrm{E}}^{*}_{\mathrm{net}}\vec{\mathrm{E}}_{\mathrm{net}} \tag{2.20}$$

Where * is the conjugate transpose operator.

2.7 Coherence

For two light beams to interfere it is not only necessary that they are overlapped but also that they are coherent. Coherence is a property that correlates two waves spatially and temporally, if the waves are not correlated in both ways the interference pattern will not be uniform.

Spatial coherence is defined as the ability of two source points to interfere when there is no time delay [12]. This means that if the source's directionality is good then spatial coherence will not be a problem for interference.

Temporal coherence is the time span that a wave continues to resemble a sinusoid of a single frequency [12]. Since there is a certain time interval for coherence it is possible to define the maximum length over which light is coherent. This length is correlated to the power spectrum of the source and can be defined based on the spectral width at full-width at half-maximum (FWHM) [13]:

$$L_c = \frac{2ln(2)}{\pi n}\frac{\lambda^2}{U_\lambda} = \frac{2ln(2)}{\pi n}\frac{c}{U_f} \tag{2.21}$$

Where L_c is the coherence length, λ the wavelength of the laser source in use, n the refractive index of air, c the speed of light, U_λ the uncertainty of the wavelength and U_f the uncertainty of the frequency of the laser source in use.

2.8 The Michelson Interferometer as a Displacement Sensor

Ever since Michelson's first steps in interferometry several improvements have been made, not only to the components themselves but also to the techniques applied. At the time Michelson used a white light source for his experiment because he required a small coherence length, but the need for higher coherence lengths led to the development of lasers. Ever since 1960 lasers were optimized and were later adopted for interferometry because of the fine wavelength properties they possess.

For the refractive index, as is detailed in section 3.3, several mathematical models have been developed to determine its value (for air) based on multiple variables such as temperature, pressure and humidity.

The feature that splits interferometry in two different fields is the detection of the number of fringes. There is a homodyne detection method that uses a single frequency laser and there is a heterodyne detection method that requires a two frequency laser.

Several different interferometric configurations have been developed using homodyne or heterodyne detection [14, 15, 16], so the approach to any problem requiring an interferometer should be to first determine the requirements and afterwards to choose a configuration optimized for such requirements.

2.8.1 Homodyne Detection

Using a single frequency source the detection is done by counting the number of fringes, like Michelson did, although nowadays it is possible to use detectors for this purpose. The conversion from number of fringes to phase difference is as simple as a multiplication by 2π:

$$\Delta\varphi = 2\pi N_f \tag{2.22}$$

This is the simplest type of detection and it leads to some of the most basic interferometric configurations. Another advantage this detection reveals is that the detector can be single-point with the goal of detecting the increase or decrease of the irradiance in the center of the interference pattern, this allows for fast processing when compared to a CCD array. The problem with such a simple setup is the lack of directional sensitivity, it is very complicated, and occasionally impossible, to know in which direction the measurement mirror is moving. Another concern with this detection method is the fact that any fluctuation on the source's intensity is mistakenly reflected in a measurement of displacement.

Since the detection is simply done by evaluating the irradiance, thus counting an integer number of fringes, the resolution of this detection method is usually limited at one fringe.

2.8.2 Quadrature

To resolve the directional sensitivity problem of simple homodyne detection the quadrature of the electric field needs to be performed, which requires polarization manipulation, unlike the last case.

By taking advantage of the two different polarizations of light, it is possible to detect the direction of the motion by delaying one of the polarizations 90° and then detecting the two polarizations in two separate detectors. For simplicity lets assume the irradiance is a perfect cosine of amplitude R that depends only on the phase difference introduced in the measurement arm of the interferometer (δ):

$$I = R\cos(\delta) \tag{2.23}$$

By delaying the vertical polarization 90° and detecting both polarizations separately we would have:

$$I_x = R\cos(\delta) \qquad I_y = R\cos\left(\delta - \frac{\pi}{2}\right) = R\sin(\delta) \tag{2.24, 2.25}$$

The direction of the displacement becomes evident when comparing both signals, if the displacement is positive, δ will be positive and we will detect the following signals:

$$V_x = R\cos(\delta) \qquad V_y = R\sin(\delta) \tag{2.26, 2.27}$$

If the displacement is negative, δ will be negative and we will detect:

$$V_x = R\cos(\text{-}|\delta|) = R\cos(|\delta|) \qquad V_y = R\sin(\text{-}|\delta|) = \text{-}R\sin(|\delta|) \tag{2.28, 2.29}$$

This translates graphically into figures 2.3a and 2.3b, respectively.

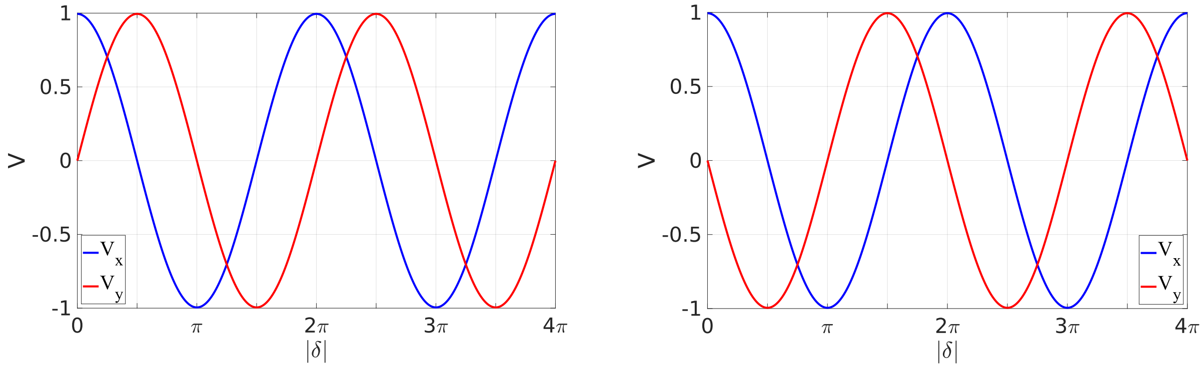

(a) Detected signals for a positive displacement ($\delta > 0$) with R=1.

(b) Detected signals for a negative displacement ($\delta < 0$) with R=1.

Figure 2.3: Quadrature schematics.

To calculate the value of δ we can use equations 2.24 and 2.25:

$$\frac{I_y}{I_x} = \frac{R\sin(\delta)}{R\cos(\delta)} = \tan\delta \;\Rightarrow\; \delta = \arctan\frac{I_y}{I_x} \tag{2.30}$$

There are many ways to achieve the 90° offset with different combinations of optical components, this inevitably leads to different ways to achieve quadrature. Another advantage this method reveals over simple homodyne detection is the smaller impact of laser fluctuations, but, due to the increased complexity, this interferometer requires more optical components and a minimum of two detectors.

As for resolution this method proves to be better than simple homodyne detection because there is access to the phase of the interfering light beams. This gives a resolution of some tenths to hundredths of a fringe.

2.8.3 Heterodyne Detection

When the polarizations of the used laser have a slightly different frequency, f_1 and f_2, the interference term of equation 2.17 becomes:

$$2\vec{\mathrm{E}}_1 \cdot \vec{\mathrm{E}}_2 \propto 2\cos(f_1)\cos(f_2) = \cos(f_1 + f_2) + \cos(f_1 - f_2) \tag{2.31}$$

Since optical frequencies are too fast to be processed by the existing electronics, any term that has an optical frequency ($|\vec{\mathrm{E}}_1|^2$, $|\vec{\mathrm{E}}_2|^2$ and the term associated to $\cos(f_1 + f_2)$) becomes an average. The remaining term is detectable because the difference of the optical frequencies of the laser is of some MHz, thus the irradiance is proportional to:

$$I \propto I_0 \cos(2\pi(f_1 - f_2)t + \delta) \tag{2.32}$$

In this case directional sensitivity is inherent to the method because of the Doppler shift induced by the moving mirror. By creating a reference before the interferometer it is possible to know if the shift in frequency was positive or negative which determines if the mirror is moving in one or the other direction. The main disadvantage of heterodyne detection is the complexity involved, there is the need for a heterodyne laser source, the detection and signal processing involved require high speeds and the components are expensive.

Considering that the phase of the interfering beam is known with more accuracy than in the quadrature method, heterodyne detection is the most accurate measurement reaching the thousandths of a fringe.

Although it has the highest resolution it is not always a better choice over the other detection methods because measuring a long displacement with a heterodyne interferometer can induce errors and will take a long time, due to the high resolution. When a homodyne interferometer has enough resolution and complies with every requirement it is always better to choose the less complex option.

2.9 Chapter Conclusions

Having reviewed all the theory necessary to comprehend interferometry and the state of the art of the technologies available, it is now possible to define the requirements for each component of the interferometer in order to comply with the uncertainty requirements of figure 1.1. This can be done by performing a detailed analysis of the uncertainty of equation 2.1 and afterwards balancing the three crucial parameters of the interferometer: the wavelength, the refractive index and the detection of the number of fringes.

Chapter 3

Uncertainty Model for Length Measurements with a Michelson Interferometer

An excellent mathematical model for a first approach to the uncertainty problem is expressed in equation 2.1, repeated below:

$$d = \frac{N_f}{2}\frac{\lambda}{n} \tag{3.1}$$

Where N_f represents the number of fringes, λ the wavelength of the used laser source and n the refractive index of air. In order to comply with the requirements of figure 1.1 the uncertainties of these three quantities needs to be estimated.

According to the Guide to the expression of Uncertainty in Measurement (GUM) [1] and to the Evaluation of the Uncertainty of Measurement in Calibration (EA-4/02) document [17], the uncertainty is given by:

$$U_d = \sqrt{\left[\frac{\lambda}{2n}\right]^2 U_{N_f}^2 + {N_f}^2 \left(\left[\frac{U_\lambda}{2n}\right]^2 + \left[-\frac{\lambda U_n}{2n^2}\right]^2\right)} \tag{3.2}$$

Equation 3.2 reveals that the uncertainties of figure 1.1 will depend on the uncertainty of the three variables: the number of fringes (U_{N_f}), the wavelength (U_λ) and the refractive index (U_n). It is also possible to conclude that the uncertainty of the number of fringes is not affected by the changes in the displacement, contrary to the other two variables, this implies the uncertainty of the number of fringes will have more impact on small displacements, while the other two uncertainties will dominate bigger displacements. The process to determine the maximum possible values of U_{N_f}, U_λ and U_n is to first evaluate any critical limitations to the system (such as the coherence length), and then maximize the remaining variables evenly.

3.1 Laser Source Restrictions

As mentioned in chapter 1 the interferometer must operate at a distance of 4 m, this implies the coherence length must be greater than four meters. Equation 2.21 reveals the relation between the coherence length and the frequency stability of the source, thus it is possible to determine the frequency uncertainty.

$$U_f = \frac{2\,ln(2)}{\pi \cdot 1.000\,271}\frac{299\,792\,458}{8} \approx 17\,\text{MHz} \tag{3.3}$$

By evaluating what manufacturers offer we concluded that there were two options for an homodyne detection system: either a non-stabilized or a stabilized He-Ne laser. As an example, the HNL series of red He-Ne lasers offered by ThorLabs [3] has a frequency stability that ranges from $1090\,\mathrm{MHz}$ (HNL008LB model) to $250\mathrm{MHz}$ (HNL210LB model). The frequency stabilized laser has a frequency stability of 2 MHz.

Since the need is for less than $17\,\mathrm{MHz}$, non-stabilized lasers were not an option. To convert frequency uncertainty to wavelength uncertainty, knowing that the wavelength of the stabilized laser is 632.991 nm, we have:

$$U_\lambda = U_f \frac{\lambda^2}{c} \approx 2.7\,\mathrm{fm} \tag{3.4}$$

3.2 Number of fringes and refractive index

To estimate the uncertainties of the number of fringes and the refractive index an uncertainty budget was calculated for every displacement of figure 1.1. For all the displacements the uncertainties of the two variables were iteratively lowered until the total uncertainty was lower than the requirement, while ensuring U_{N_f} and U_n contributed evenly to the total uncertainty. The results obtained are represented in table 3.1.

Table 3.1: Estimation of the maximum uncertainties required for the number of fringes and the refractive index. The total uncertainty obtained and the required uncertainty are also represented for comparison.

d [mm]	U_{N_f}	$U_n \times 10^{-7}$	$U_{d_{obt}}$ [μm]	$U_{d_{req}}$ [μm]
0.1	0.02	700	0.0094	0.01
0.5	0.055	350	0.025	0.025
10	0.02	7	0.0094	0.01
25	0.055	7	0.025	0.025
100	0.22	7	0.099	0.1
500	1.1	7	0.49	0.5
1000	2.2	7	0.99	1
4000	11	8.5	4.9	5

Table 3.1 reveals that the uncertainties of the number of fringes and the refractive index vary according to the displacement. The target uncertainty for the number of fringes and the refractive index was defined as the minimum values displayed in table 3.1, thus the uncertainty of the number of fringes must be smaller than 0.02 and the uncertainty of the refractive index must be smaller than $7{\times}10^{-7}$.

In figure 3.1 we can see the requirements already defined previously in figure 1.1, the optimized value of the uncertainty for each displacement, where all the components of the uncertainty have the same weight (corresponding to table 3.1), and the final value of the uncertainty where the critical displacement of the optimized case ($10\,\mathrm{mm}$) fixed the minimum value of the uncertainty for every displacement.

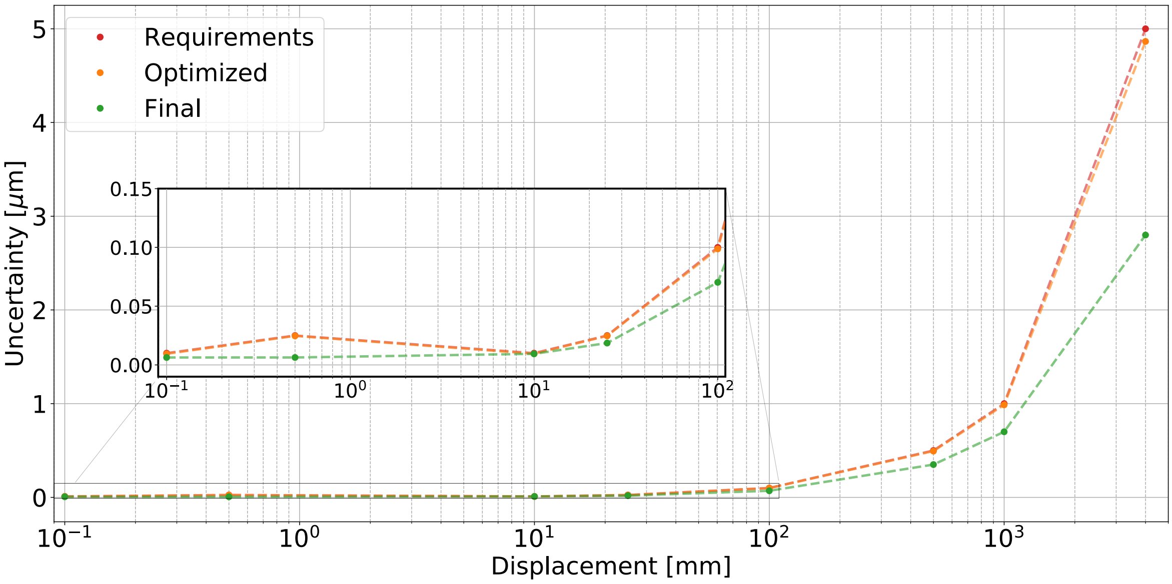

Figure 3.1: Estimated uncertainty of the interferometer.

3.3 Refractive index mathematical model

The refractive index is a function of temperature, pressure and relative humidity. Several improvements of its estimation have been done over the years [18]. Such complex mathematical models are too intricate for a simple approach so NIST developed a simplified version, the NIST Shop Floor refractive index calculation [19]:

$$n = 1 + \frac{7.86\times10^{-4}P}{273+T} - 1.5\times10^{-11}RH(T^2+160) \tag{3.5}$$

Where T is temperature in °C, P is pressure in kPa and RH is relative humidity in percentage (between 0 and 100).

Knowing the required uncertainty for the refractive index ($U_n = 7\times10^{-7}$) the uncertainties of the temperature, pressure and relative humidity were estimated while trying to maintain the weight of each component equal, as was done in section 3.2. For the uncertainty calculations it was considered $T = 20\,°\mathrm{C}$, $P = 101.3\,\mathrm{kPa}$ and to avoid measuring relative humidity it was assumed $RH = 50\,\% \pm 50\,\%$, with these conditions we obtained $U_T = 0.4\,°\mathrm{C}$ and $U_P = 150\ \mathrm{Pa}$ and it was also possible to balance these uncertainties evenly, in a way that each component contributed approximately 33 % to the total uncertainty of the refractive index.

3.4 Chapter Conclusions

Considering the direction of the displacement must be known, and the necessary accuracy in the number of fringes was 0.02, simple homodyne detection was excluded. The two remaining options were quadrature or heterodyne detection. As mentioned before, one of the disadvantages of heterodyne detection is when a long displacement needs to be measured, so the natural choice for the detection method was quadrature.

For the laser source it was already demonstrated that any non-stabilized laser does not have enough coherence length for the interferometer to operate at a distance of 4 m so the only possibility was a stabilized laser.

Finally, to calculate the refractive index the temperature and pressure must be measured and stable during the measurements. To achieve the uncertainties required ($U_T = 0.4\,^{\circ}\mathrm{C}$ and $U_P = 150\ \mathrm{Pa}$) a common laboratory thermometer and barometer are enough. As for stabilization, pressure is usually stable in the time interval needed for measurements and for temperature one possible solution is to average its value at the beginning and at the end of the measurement and use the variation as the uncertainty. With respect to the relative humidity, although it can be measured and used for the calculations it doesn't need to be considered because using $RH = 50\,\% \pm 50\,\%$ is enough to achieve the required uncertainty on the refractive index.

Having concluded that quadrature is necessary the next step was to defined an optical configuration for the interferometer.

Chapter 4

Evaluation of Optical Configurations

It was already mentioned that quadrature can be accomplished in many different ways, this leads to a large number of optical configurations, each one with advantages and disadvantages. Four different optical configurations were studied due to their peculiarities [20, 21, 22, 23], with the intent of defining the one that would be assembled. To correctly evaluate each configuration first there is the need to evaluate if the phase difference introduced between each polarization totals 90°, this is easily proven using Jones notation, and is detailed in appendix A. After knowing that the configurations function as intended one can consider the advantages and disadvantages each configuration possesses and the physical/optomechanical limitations.

4.1 Quadrature with two polarizing beamsplitters

The Field Guide to Displacement Metrology [20] proposes a unique configuration that uses two polarizing beamsplitters.

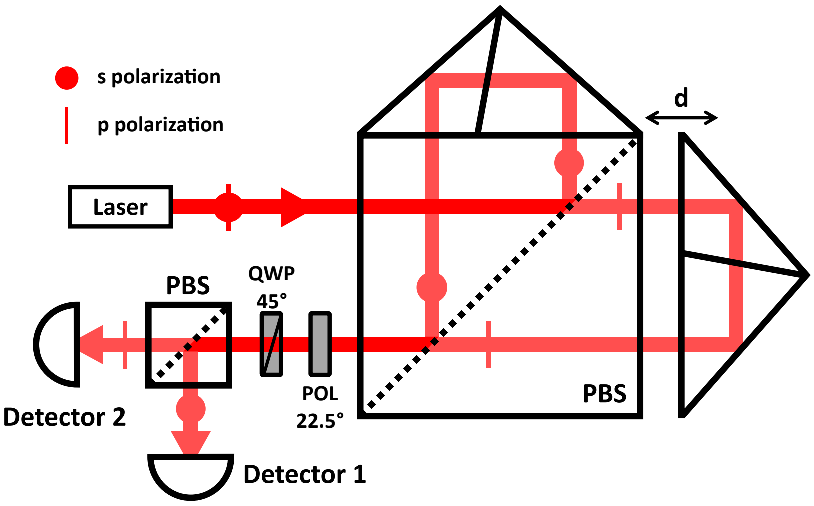

Figure 4.1: Schematic of a quadrature Michelson interferometer using two polarizing beamsplitters.

Besides the use of two polarizing beamsplitters, another interesting aspect of this configuration is that the 90° offset between polarizations is given by two consecutive components: the polarizer and the waveplate. By analysing the optical configuration with Jones notation it is possible to conclude that the offset between the two irradiances (equation A.5) is indeed 90°.

Although it proves quite simplistic there is a critical disadvantage in this configuration, equation A.5 reveals that the amplitude of the irradiance is quite small which is a problem since it would affect the detection efficiency.

4.2 Quadrature with a non-polarizing beamsplitter

Bai *et al.* [21] present a quadrature configuration that uses a non-polarizing beamsplitter.

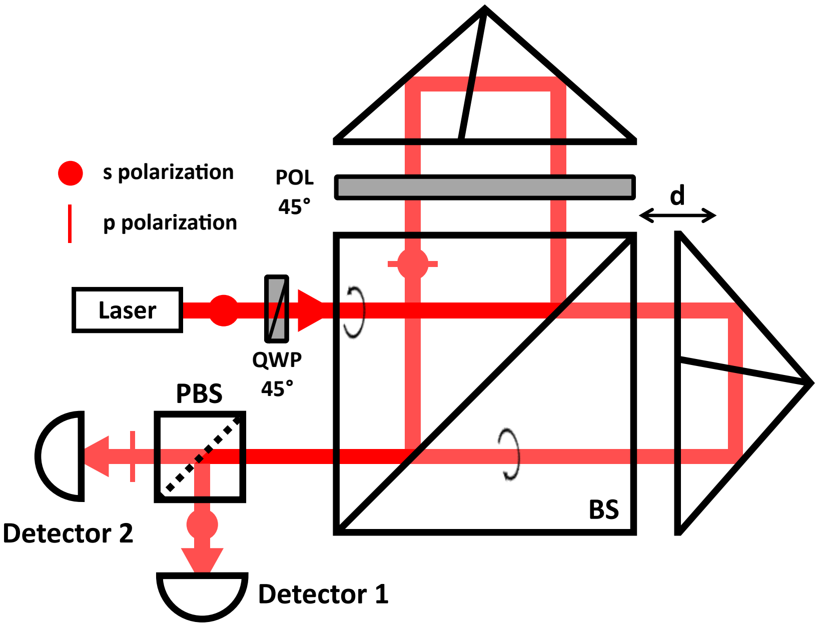

Figure 4.2: Schematic of a quadrature Michelson interferometer using a non-polarizing beamsplitter.

In spite of the different optical component positioning this configuration also proves relevant because there are no elements between the two beamsplitters, so the detection module (composed by the final polarizing beamsplitter and the two detectors) is independent from the rest of the interferometer.

Equation A.9 proves that the phase difference is the desired 90° and we can also conclude that the amplitude of the irradiance increased 2.6 times, which is significant.

4.3 Quadrature with two quarter waveplates

The University of Minnesota reveals an optical configuration that does not use polarizers [22] thus the following configuration will not suffer the unnecessary attenuation of the last two cases. Due to the light beam passing twice through a beamsplitter the minimum attenuation possible is 1/4 of the initial value. Equation A.13 confirms this statement, proving that the excessive attenuation of the previous cases was only due to the presence of a polarizer.

The positioning of the quarter waveplates in this configuration is not ideal, experimentally the area to build the interferometer was limited and having to position a quarter waveplate between two components twice would inevitably increase the size of the assembly.

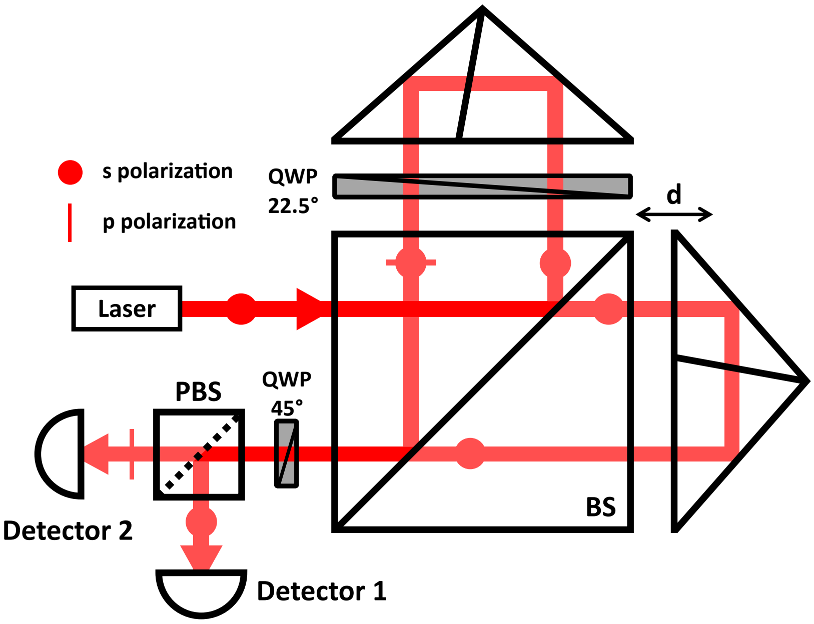

Figure 4.3: Schematic of a quadrature Michelson interferometer using two quarter waveplates.

4.4 Quadrature with an octadic waveplate

Gregorčič *et al.* propose a simple configuration that only requires one octadic waveplate.

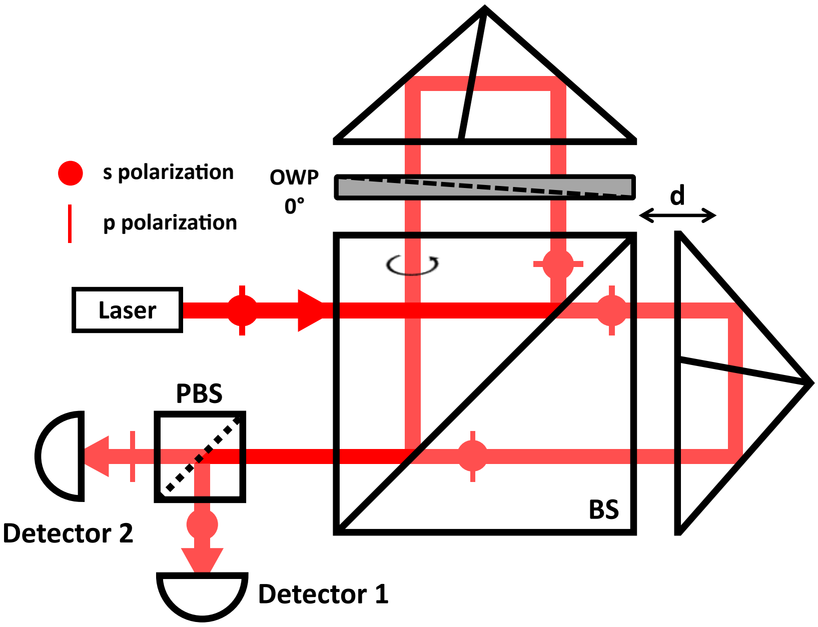

Figure 4.4: Schematic of a quadrature Michelson interferometer using an octadic waveplate.

Equations A.13 and A.17 are identical thus the irradiance is exactly the same as in the last case. The fact that there is only the need for one optical component to apply the 90° offset is excellent when comparing this configuration with all the previously studied, but despite the ease of assembly of the configuration the octadic waveplate is not a common component and often times must be custom made.

4.5 Configuration Evaluation

After comparing the amplitude of the irradiances, the first configuration (figure 4.1) was excluded considering that the other three cases have amplitudes 2.6 to 3.4 times bigger. In the remaining cases the irradiance gain was not significant enough to exclude the second configuration. Since the octadic waveplate was not available the last configuration (figure 4.4) was also excluded.

Between the second and the third configurations the optomechanical parts are a key point of the selection. In figure 4.3 there exists a component between both beamsplitters that is not present in the second configuration, figure 4.2, where the detection module is independent from the rest of the interferometer. The fact that the second configuration allows more flexibility in the positioning of the detection module, which will make the interferometer smaller, was the reason why the third configuration was excluded, even though it had a 32 % irradiance gain.

4.6 Chapter Conclusions

Defining an optical configuration is not only an optical problem but optomechanical concerns must also be taken into account. There is always an experimental side to the assembly of an instrument that must not be forgotten and the necessary alignments need to be very carefully and accurately done, which is no simple task. The only missing subject of the interferometer, before the assembly, is the signal processing necessary to count the number of fringes.

Chapter 5

Signal Processing

The signal processing required to extract the number of fringes from two quadrature signals was divided in three different sections. Initially the acquired signals must be stripped of all offsets, turning into perfect sinusoidal functions, the method used for the corrections was proposed by Peter L. M. Heydemann [24] in 1981 and later explored by Wu *et al.* [25] in 1996. Using the corrected signals the phase difference introduced by the optical path difference between the two arms of the interferometer is calculated, afterwards the phase is unwrapped to become a continuous value and the calculation of the number of fringes follows by dividing the unwrapped phase by 2π, as equation 2.22 suggests.

5.1 Detected Signals

The acquired signals at the detectors differ from equations 2.26 and 2.27. The discrepancies include offsets, different gains, the phase difference applied will never be exactly 90° and these differences vary with time. The detected signals V_x^d and V_y^d can be expressed as:

$$V_x^d = R\cos(\delta) + p \qquad\qquad V_y^d = \frac{R}{r}\sin(\delta - \alpha) + q \qquad (5.1, 5.2)$$

Where R represents the amplitude of the sinusoids, r the different gain of each detector, α the phase difference error to 90° and p and q the different offsets of each signal.

Graphically, by displaying the Lissajous figure of each signal (figures 5.1a and 5.1b), the parameters are easily visualized. It is fundamental that these effects are corrected, otherwise the phase difference cannot be extracted by directly correlating the two signals as equation 2.30 revealed.

5.2 Signal Correction

The ideal signals can be expressed as a function of the detected signals by inverting equations 5.1 and 5.2:

$$V_x = V_x^d - p \qquad\qquad V_y = \frac{1}{\cos\alpha}[(V_x^d - p)\sin\alpha + r(V_y^d - q)] \qquad (5.3, 5.4)$$

To determine the r, α, p and q parameters an elliptical fit must be performed over the detected signals. Since the ideal signals describe a circumference of radius R, we have:

$$V_x^2 + V_y^2 = R^2 \qquad (5.5)$$

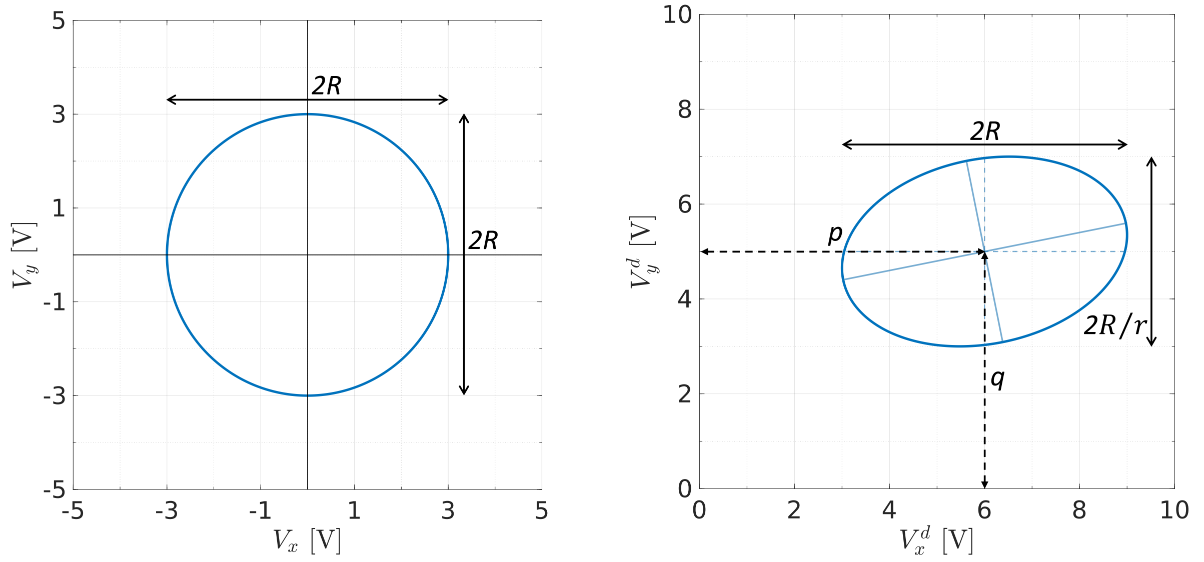

(a) Lissajous figure of the ideal signals 2.26 and 2.27 with R=3.

(b) Lissajous figure of the detected signals 5.1 and 5.2 with R=3, p=6, q=5, r=1.5, α=-10°.

Figure 5.1: Lissajous figures of ideal and detected signals.

Using equations 5.3 and 5.4 we get:

$$(V_x^d - p)^2 + \left[\frac{(V_y^d - q)r + (V_x^d - p)\sin\alpha}{\cos\alpha}\right]^2 = R^2 \tag{5.6}$$

Which can be expressed as the equation of an ellipse:

$$V_x^{d^2} + BV_y^{d^2} + CV_x^d V_y^d + DV_x^d + EV_y^d + F = 0 \tag{5.7}$$

With the following change of variables:

$$B = r^2 \tag{5.8a}$$
$$C = 2r\sin\alpha \tag{5.8b}$$
$$D = -2p - 2qr\sin\alpha \tag{5.8c}$$
$$E = -2qr^2 - 2pr\sin\alpha \tag{5.8d}$$
$$F = p^2 + q^2r^2 + 2pqr\sin\alpha - R^2\cos^2\alpha \tag{5.8e}$$

Using equations 5.8a, 5.8b, 5.8c and 5.8d we can now calculate r, α, p and q:

$$r = \sqrt{B} \tag{5.9a}$$
$$\alpha = \arcsin\left(\frac{C}{2\sqrt{B}}\right) \tag{5.9b}$$
$$q = \frac{2E - DC}{C^2 - 4B} \tag{5.9c}$$
$$p = \frac{DC^2 - 2EC}{2C^2 - 8B} - \frac{D}{2} \tag{5.9d}$$

Since equation 5.7 describes an ellipse, to estimate the parameters B, C, D and E we can use the least squares method. The objective of this method is to minimize the difference between the predictions of the determined model and the actual value used to estimate it, the residual. Knowing that the fit will not be perfect, equation 5.7 will not equal zero, but for each V^d_{xi}, V^d_{yi} pair it will equal its residual (ϵ_i), so for N acquired samples we have:

$$V^{d^2}_{xi} + BV^{d^2}_{yi} + CV^d_{xi}V^d_{yi} + DV^d_{xi} + EV^d_{yi} + F = \epsilon_i \qquad i \in [1, N] \tag{5.10}$$

The estimated parameters need to be chosen so that the sum of the squared residuals is as small as possible, which is achieved if the gradient of the sum of the squared residuals is null:

$$\frac{\partial}{\partial x_j}\sum_{i=1}^{N}\epsilon_i^2 = 0 \qquad x_j = B, C, D, E, F; \;\; i \in [1, N] \tag{5.11}$$

From equation 5.11 result 5 different equations with 5 different variables that can be expressed by the following system of equations:

$$XX^T \begin{bmatrix} B \\ C \\ D \\ E \\ F \end{bmatrix} = -X\sum_{i=1}^{N} V^{d^2}_{xi} \qquad X = \begin{bmatrix} \sum_{i=1}^{N} V^{d^2}_{yi} \\ \sum_{i=1}^{N} V^d_{xi}V^d_{yi} \\ \sum_{i=1}^{N} V^d_{xi} \\ \sum_{i=1}^{N} V^d_{yi} \\ N \end{bmatrix} \tag{5.12}$$

5.2.1 Phase Difference Error

Correcting the phase difference error and assuming the desired 90° is incorrect considering the experimental error is not being altered and errors would be introduced in the displacement. To solve this problem a different approach was taken, this does not affect the calculation of the parameters explained previously.

If the signals are corrected with the exception of the phase difference error we have:

$$V^c_x = R\cos\delta \qquad\qquad V^c_y = R\sin(\delta - \alpha) \tag{5.13, 5.14}$$

By using the same reasoning as in equation 2.30 we get:

$$\frac{V^c_y}{V^c_x} = \frac{\sin(\delta - \alpha)}{\cos\delta} \Rightarrow \delta = \arctan\left(\frac{1}{\cos\alpha}\frac{V^c_y}{V^c_x} + \tan\alpha\right) \tag{5.15}$$

Two new terms related to the phase difference error appear in the equation. This suggests that it is possible to achieve quadrature without having a 90° phase difference between each polarization, although being close to 90° is desired due to the effect of α on the equation being minimal, while when the phase difference tends to 0° (α tends to 90°) its effect is critical and a miscalculation of the parameter would introduce bigger errors.

5.3 Arctangent Function Limitations

When the argument of the arctangent function is a quotient there is a problem with the cancellation of signals. This means that there is no possible way to distinguish the cases when V_x and V_y are both positive or negative, and also the cases when both signals are different, these redundancies are detailed in figure 5.2.

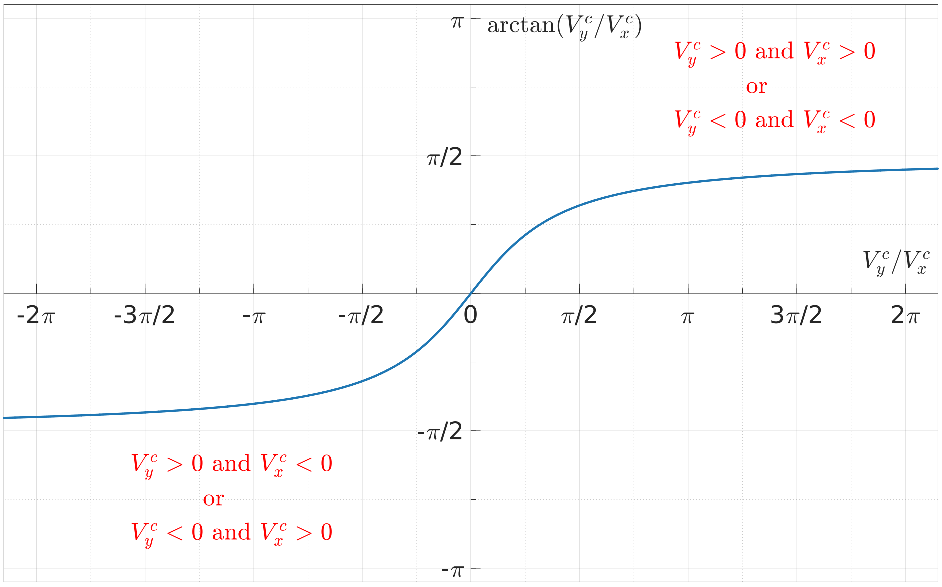

Figure 5.2: Graphical representation of the arctangent function range limitation and ambiguities.

To span the four quadrants and have no redundancy there is the need to use a function appropriate to this case. The four quadrant inverse tangent, also known as atan2, is defined as:

$$\operatorname{atan2}(y,x) = \begin{cases} \arctan\left(\frac{y}{x}\right) & \text{if } x > 0, \\ \arctan\left(\frac{y}{x}\right) + \pi & \text{if } x < 0 \text{ and } y \geq 0, \\ \arctan\left(\frac{y}{x}\right) - \pi & \text{if } x < 0 \text{ and } y < 0, \\ \frac{\pi}{2} & \text{if } x = 0 \text{ and } y > 0, \\ -\frac{\pi}{2} & \text{if } x = 0 \text{ and } y < 0, \\ \text{undefined} & \text{if } x = 0 \text{ and } y = 0 \end{cases} \tag{5.16}$$

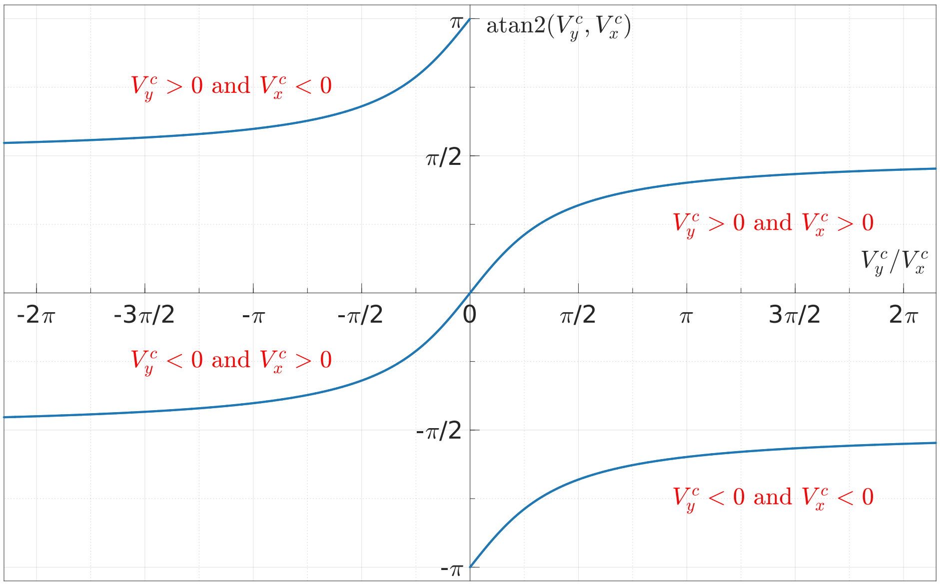

Figure 5.3: Graphical representation of the four quadrant inverse tangent function.

As figure 5.3 shows, the atan2 function has a range of 2π, spanning the four quadrants and also overcoming the previous redundancies. This indicates that the atan2 function is an ideal substitute for the arctangent function. We can now rewrite the phase as:

$$\delta = \text{atan2}(V_y^c + V_x^c \cos\alpha \sin\alpha, V_x^c \cos\alpha) \tag{5.17}$$

5.4 Phase Unwrapping

Phase unwrapping consists on the accumulation of the total phase, which is particularly important when dealing with functions with a limited range such as the atan2 function. Without accumulating the total phase it would be impossible to have displacements bigger than a fringe because the phase would be limited to $]-\pi;\pi]$.

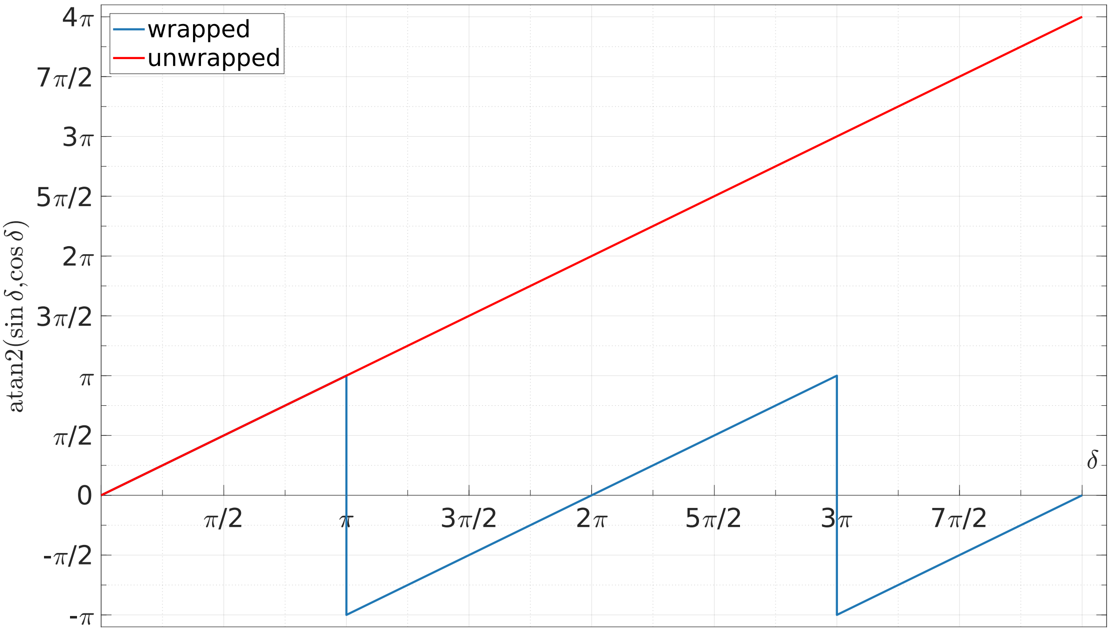

Figure 5.4: Comparison of the wrapped and unwrapped atan2 functions.

Figure 5.4 emphasizes the wrapped phase's discontinuities. It follows that a simple way to unwrap the phase is to use an algorithm that adds or subtracts 2π every time the phase difference changes more than π. One possible definition for such an algorithm operating over an array of phases (δ) with N elements is:

$$\delta_u[i] = \begin{cases} \delta[i] - \left\lfloor \dfrac{\delta[i] - \delta_u[i\text{-}1]}{2\pi} + 0.5 \right\rfloor \times 2\pi & \text{if } 1 \geq i \geq N-1, \\ \delta[i] & \text{if } i = 0 \end{cases} \tag{5.18}$$

5.4.1 Implications of phase unwrapping in the sampling frequency

Although equation 5.18 proves to be a simple solution to unwrap the phase it creates concerns over the number of samples per fringe. Figure 5.5 reveals that if the number of samples per fringe is smaller than two it is impossible to know if there was a change in the direction of the movement.

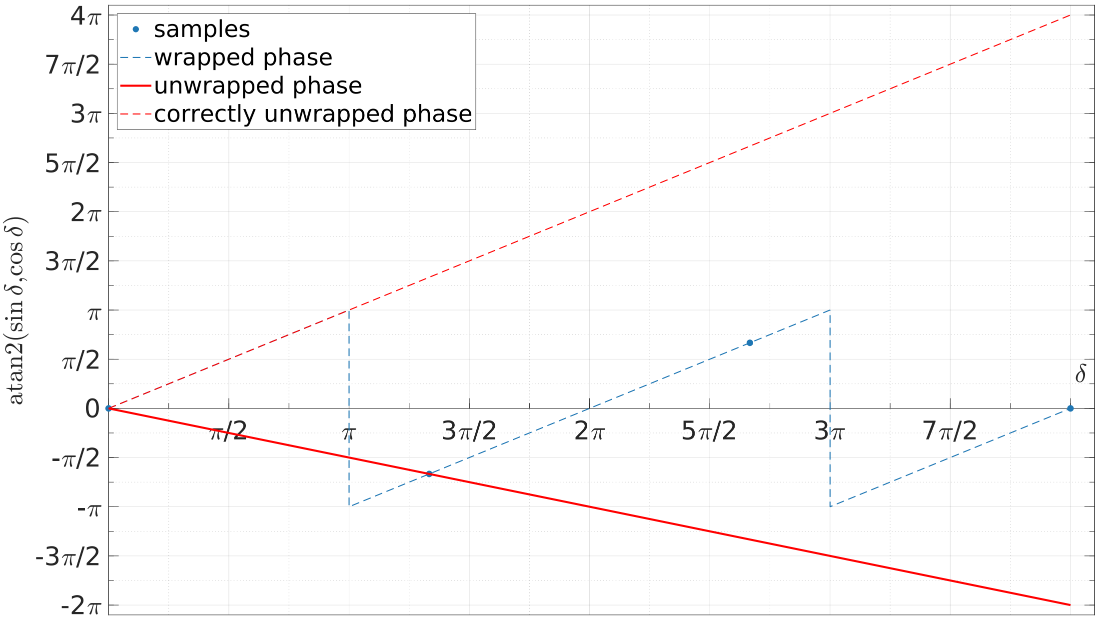

Figure 5.5: The unwrapping of figure 5.4 is repeated but with a small amount of samples. It is possible to see that the algorithm cannot correctly unwrap the phase and assumes the wrong direction for the movement.

Using equation 3.1, the stage's velocity in fringes per second is:

$$v_{fringes/s} = \frac{2n}{\lambda} v_{m/s} \tag{5.19}$$

Since the number of samples per fringe needs to be bigger than two the sampling frequency is given by:

$$f_s > 2 \times \frac{2n}{\lambda} v_{m/s} \tag{5.20}$$

5.5 Chapter Conclusions

Although the signal processing to extract the number of fringes from two quadrature signals already existed, several improvements were done, namely the correction of the phase difference error. Another very important aspect that we take from this chapter is the limitation of the sampling frequency imposed by the phase unwrapping (equation 5.20) because it defines the necessary sampling frequency for the interferometer to operate correctly.

Having discussed all the critical aspects of the system the assembly of the interferometer can now be considered.

Chapter 6

System Design, Implementation and Integration

Before projecting the interferometer a prototype was assembled to test some important aspects of the laser source in the chosen configuration. Once the prototype was tested and a stage was studied, the system was projected and different ways to assemble the chosen configuration were studied according to the available materials. After defining the position of every element of the interferometer with the use of a 3D model the system was assembled. Finally, the data acquisition and signal processing were implemented in LabVIEW.

6.1 Preliminary Design

Before designing the interferometer a prototype was assembled (figure 6.1) according to the configuration chosen in chapter 4. This first step was crucial because it was possible to verify that the configuration worked as intended experimentally and the prototype also allowed the study of critical aspects of the interferometer, such as retroreflections and the beam divergence. After all these factors were corrected the movement of a translation stage was studied in order to test the signal processing of chapter 5.

6.1.1 Retroreflections

The first conclusion noted during the assembly of the prototype was the impact of the retroreflections in the alignment of any optical component. Every surface will reflect the incident light to some degree, in the particular case when the optical surface is normal to the incident beam the reflection will be coincident with the incident beam, which becomes a serious concern because the reflection will fall into the laser cavity destabilizing the laser, not only changing its wavelength but also damaging the laser itself.

The solution to this problem is the introduction of a Faraday Isolator immediately after the laser. A Faraday Isolator uses Faraday rotators to change the polarization of light, this change in polarization is non-reciprocal, unlike in polarizers or in waveplates, so the direction of the beam influences the change in polarization. With a Faraday Isolator after the laser, aligned in a way that its own reflections do not fall into the laser cavity, any retroreflection in the interferometer that is incident on the Faraday Isolator is filtered while the laser beam passes through the component “unaffected”, ensuring the stability of the laser.

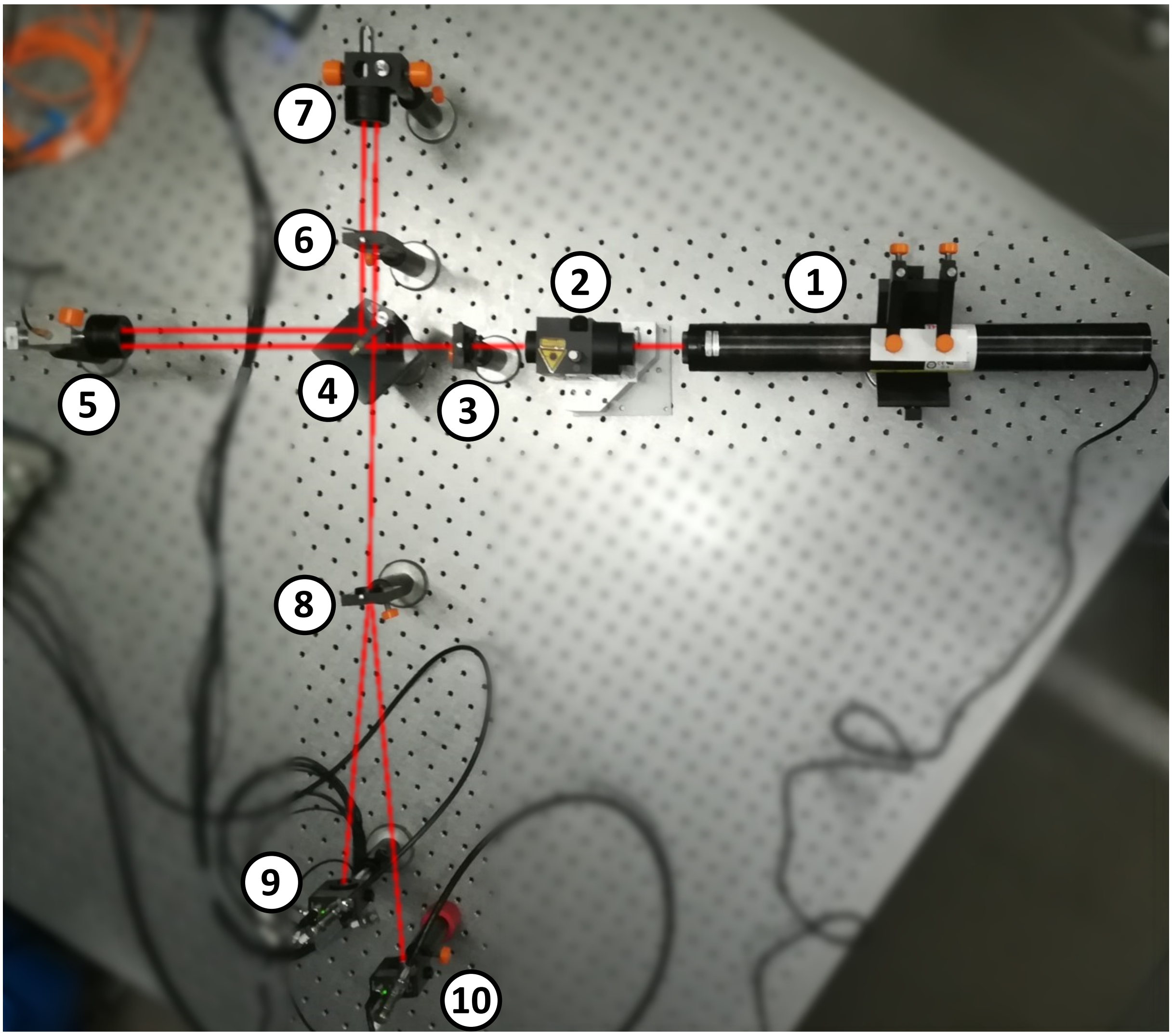

Figure 6.1: Assembled prototype to study the chosen configuration. 1-Laser; 2-Faraday Isolator; 3-Quarter Waveplate; 4-Beamsplitter; 5-Measurement Retroreflector; 6-Polarizer; 7-Reference Retroreflector; 8-Wollaston Prism; 9-Vertical Polarization Detector; 10-Horizontal Polarization Detector.

6.1.2 Divergence

By using a stabilized He-Ne laser we guaranteed that even with an optical path difference of 8 m interference can still be detected, however the beam emitted by the laser is not collimated, it had a divergence that although small (1.8 mrad) was a problem for long optical paths. The diameter of the laser beam after the cavity was 0.5 mm, but at the end of the 4 m measurement arm the diameter of the beam grew to be 16 mm. This was a problem due to the detectors being 3.6 mm sided squares and also because the two interfering beams had extremely different wavefront curvature radii.

Using a Beam Expander with a magnifying power of 4 times the divergence of the laser beam was reduced at the cost of increasing its diameter, a disadvantage overcame by placing the beam expander as close to the laser source as possible. As figures 6.2a and 6.2b reveal, with the beam expander it was possible to reduce the laser beam diameter at the end of the measurement arm (4 m) from the previous 16 mm to 4 mm, it was also possible to adjust the beam expander in a way that the laser beam was collimated, which ensured it mostly fit inside both detectors' windows.

(a) Beam divergence without the beam expander.

(b) Beam divergence with the beam expander.

Figure 6.2: Comparison of the beam divergence with and without the beam expander, 4 m away from the interferometer.

After guaranteeing that the laser beam's diameter was close the detectors' window size a study was conducted about the interference pattern created in the detector plane, detailed in appendix B, in order to evaluate the possible advantages of using a diaphragm to limit the number of fringes. The conclusions revealed that there would only be benefits to using a diaphragm for displacements over 1.5 m, which did not justify the use.

6.1.3 Prototype Testing

Once the prototype was assembled and the problems with the retroreflections were corrected, the piezoelectric element in figure 6.1 that had a maximum displacement of 13 μm was replaced by a translation stage with a maximum displacement of 25 mm. Four different measurements were recorded for two different velocities (0.1 mm/s and 1 mm/s) and accelerations (1 mm/s^2 and 10 mm/s^2) in order to test the signal processing of chapter 5 and to study the effects of different velocities and accelerations on the displacement. The acquired data is represented in figures 6.3 through 6.6 and also in table 6.1.

In figure 6.3 the effect of increasing the acceleration is quite evident, figure 6.4 shows that with a smaller acceleration the defined velocity of 1 mm/s is reached further in time, the same happens with the deceleration. Although figure 6.5 reveals that the change in acceleration for a smaller velocity has no impact the beginning of the movement is more abrupt, this situation is better comprehended when considering the velocity graph, figure 6.6. The first steps of the stage cause the velocity to increase past the desired quantity, while in the other case this problem does not arise.

Table 6.1: Displacement error (in μm) to the stage's indicated value of 25 mm.

a [mm/s^2] v [mm/s]	10	1
1	2.7	1.8
0.1	0.45	0.9

The four different displacements of table 6.1 indicate that for high velocities the displacement is further away from the indicated value by the stage's software, this suggests that at this point the signal processing was not being correctly implemented because there should not be an impact of the velocity of the stage on the displacement measured. Although there are discrepancies in the measurement these errors represent less than 0.02 % of the total displacement, when considering that the measurements were done without much rigour and with a prototype we can conclude that the properly assembled interferometer can only have better results.

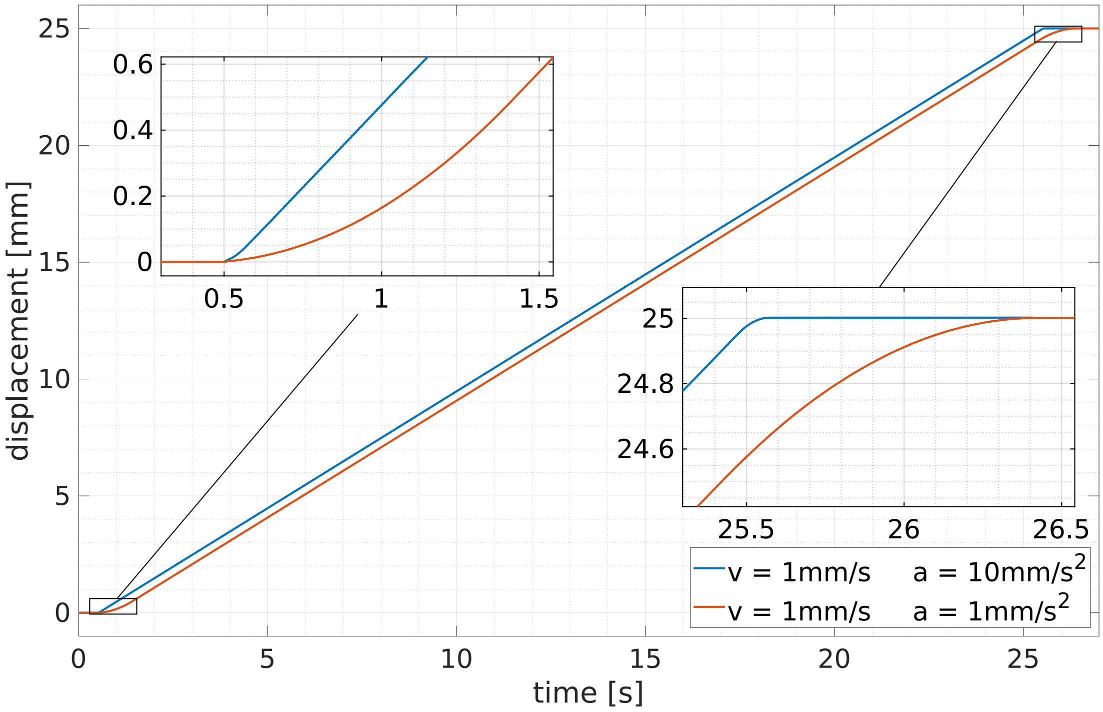

Figure 6.3: Displacement measurements for a velocity of $1\,\mathrm{mm/s}$ while changing the acceleration of the translation stage.

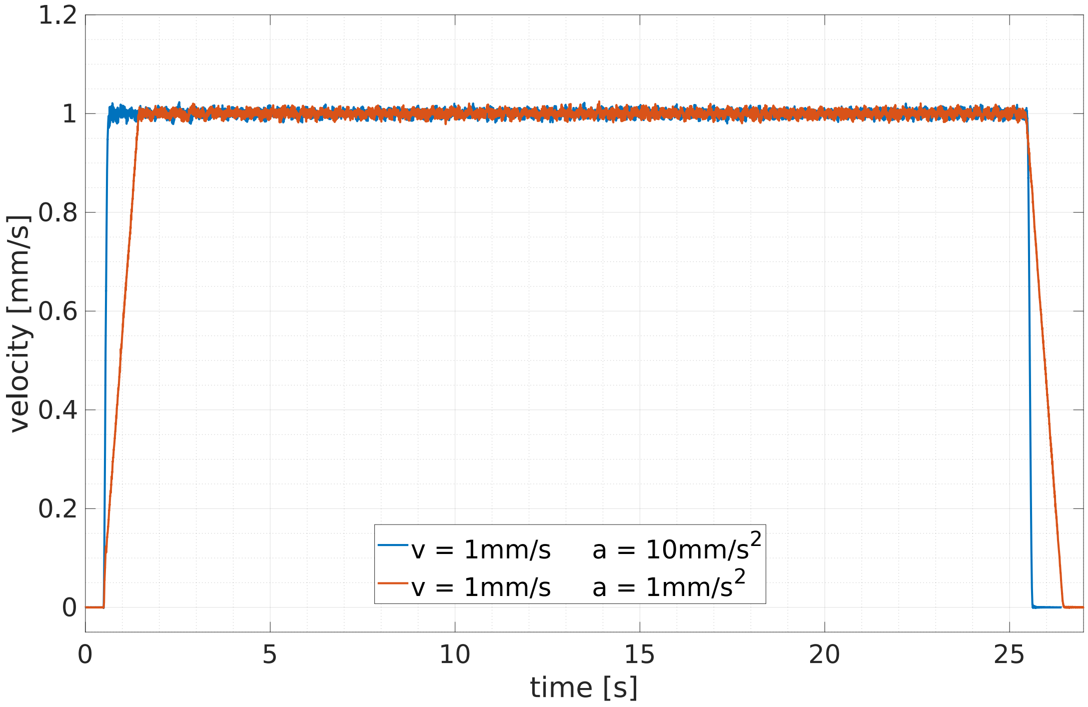

Figure 6.4: Calculation of the velocity by differentiating the displacement arrays of figure 6.3 and applying a moving average of 1000 elements.

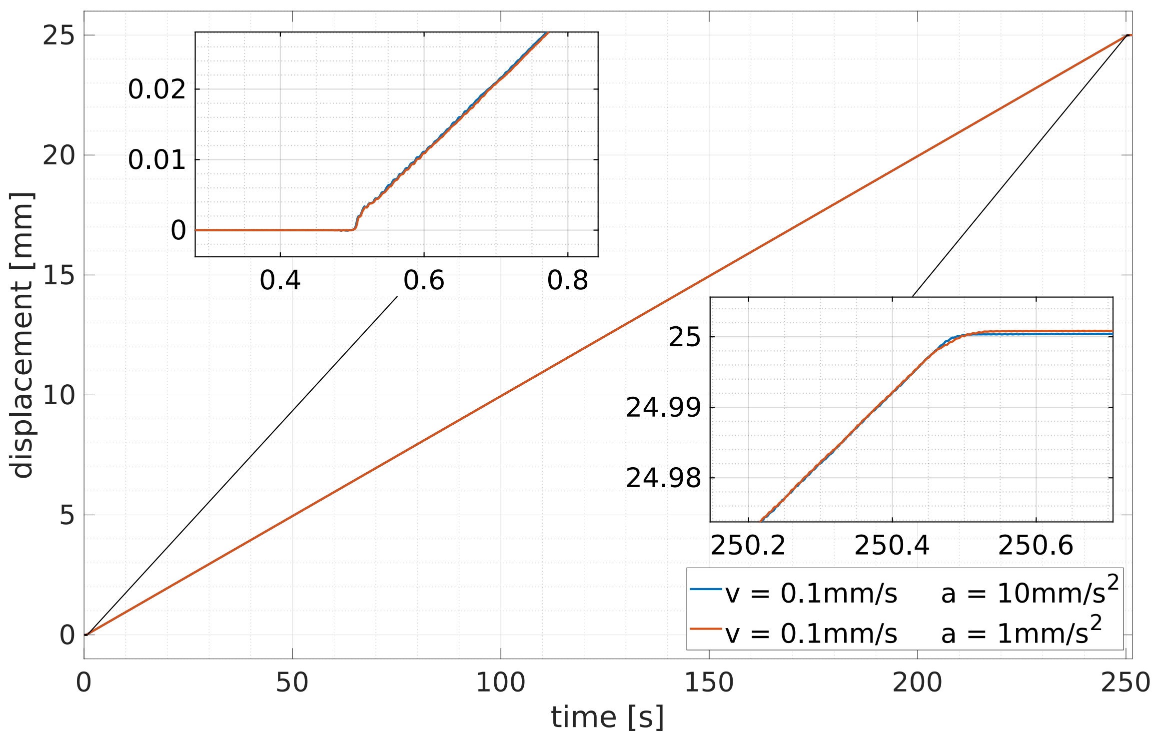

Figure 6.5: Displacement measurements for a velocity of $0.1\,\mathrm{mm/s}$ while changing the acceleration of the translation stage.

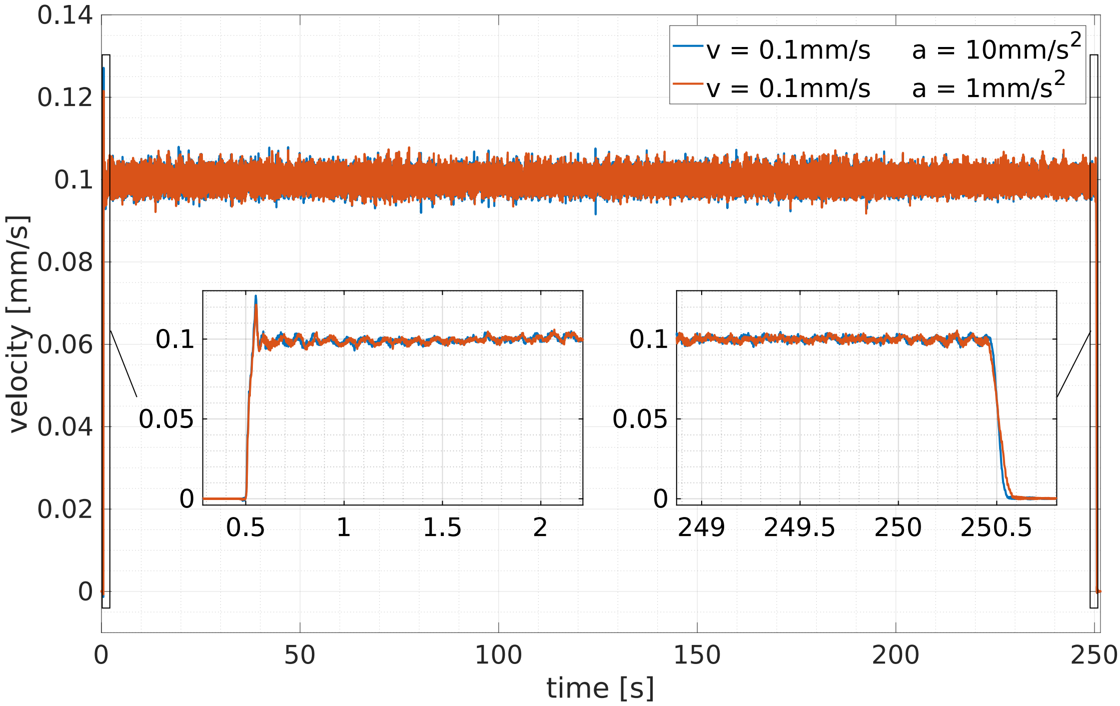

Figure 6.6: Calculation of the velocity by differentiating the displacement arrays of figure 6.5 and applying a moving average of 1000 elements.

6.2 Optomechanical System Design

When designing the system, the limitations imposed by the available materials were taken into consideration. The optical table used in the interferometer was a 460 mm × 300 mm rectangle, so the laser (a 400 mm long cylinder) could not be aligned with the rest of the interferometer. This constraint imposed the use of at least one mirror to redirect the laser beam. Following the definition of the components to be used in the assembly of the interferometer, the height of the laser beam was defined according to the height of the highest component, the Faraday Isolator, whose optical axis was 100 mm above the surface of the table. Once the optical axis' height was defined, two spacers were made to raise the laser and the mirrors 50 mm and a block was used to raise the beamsplitter's support 30 mm, the rest of the optical components were placed on vertically adjustable supports.

After all the necessary materials to be used in the assembly were defined multiple schematics were planned for the disposition of the components on the optical table, shown in figure 6.7.

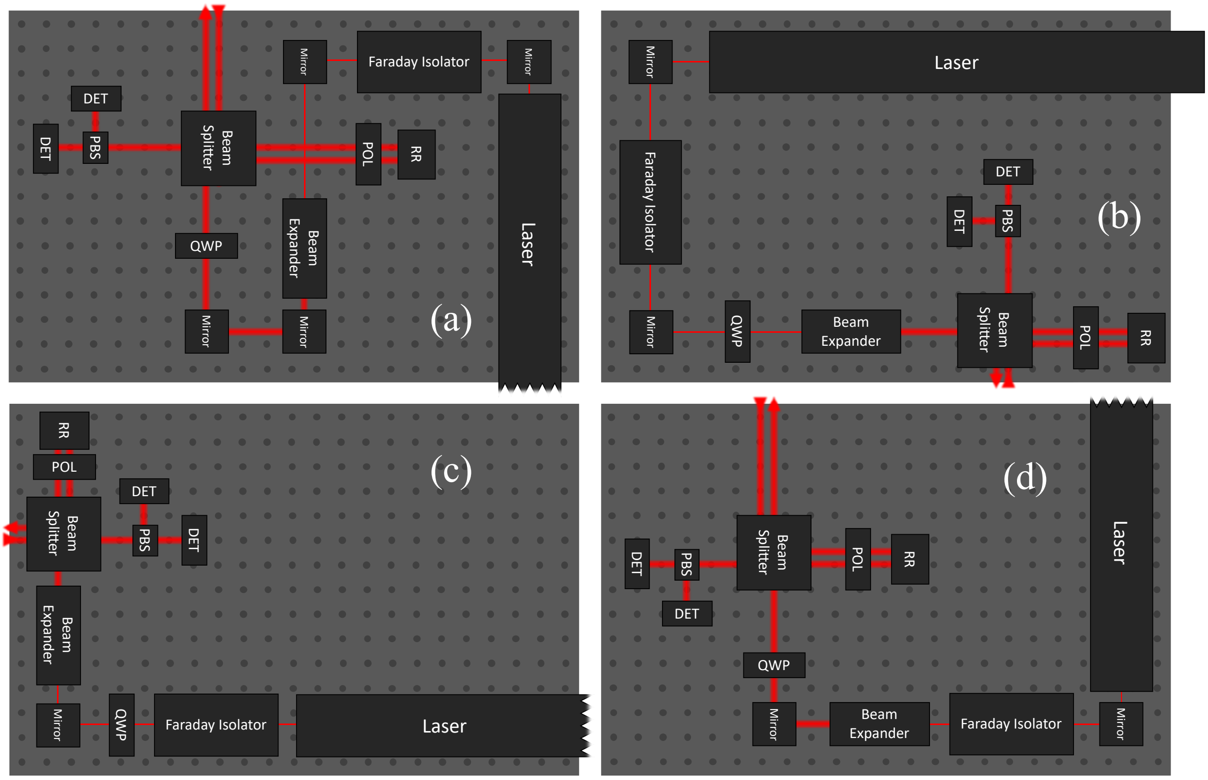

Figure 6.7: Four different schematics considered for the assembly of the interferometer. The representations are all up to scale (approximately 2/125).

Of every proposed schematics it was considered that figure 6.7b was the easiest to implement, not only because of the optimization of the available area but also because of the easy cable management allowed by the position of the detectors and the laser.

In every configuration the beam passes twice through the polarizer, which had 20 mm diameter, while the beam had 4 mm diameter, as is shown in figure 6.8. The ideal distance between the center of the two beams is 10 mm, thus when positioning the retroreflectors it was fundamental to introduce a 10 mm lateral displacement.

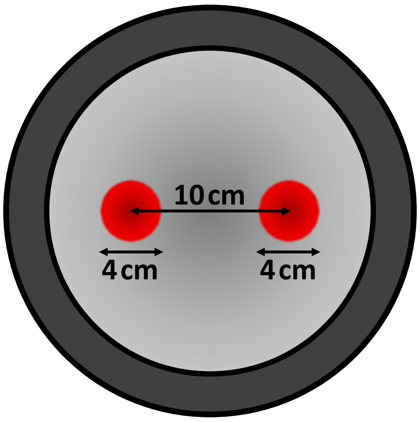

Figure 6.8: Schematic of the ideal distance between both passages of the beam through the polarizer.

Another constraint imposed by the material was the position of the polarizing beamsplitter in its support, as is clarified in figure 6.9. When placing the polarizing beamsplitter the rods holding the vertical support must not be in the path of the reflected beam while always ensuring that the PBS is sturdily mounted.

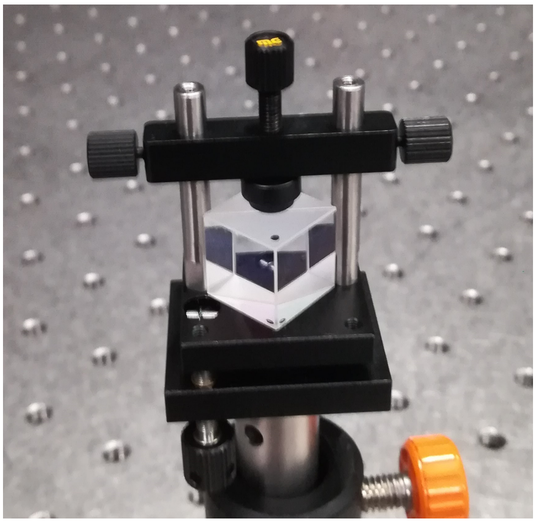

Figure 6.9: Positioning of the polarizing beamsplitter in its support.

Considering all these restrictions and the schematic of figure 6.7b a 3D model of the interferometer was built. Another schematic up to scale 3/100 is represented in figure 6.10 for ease of interpretation of figure 6.11.

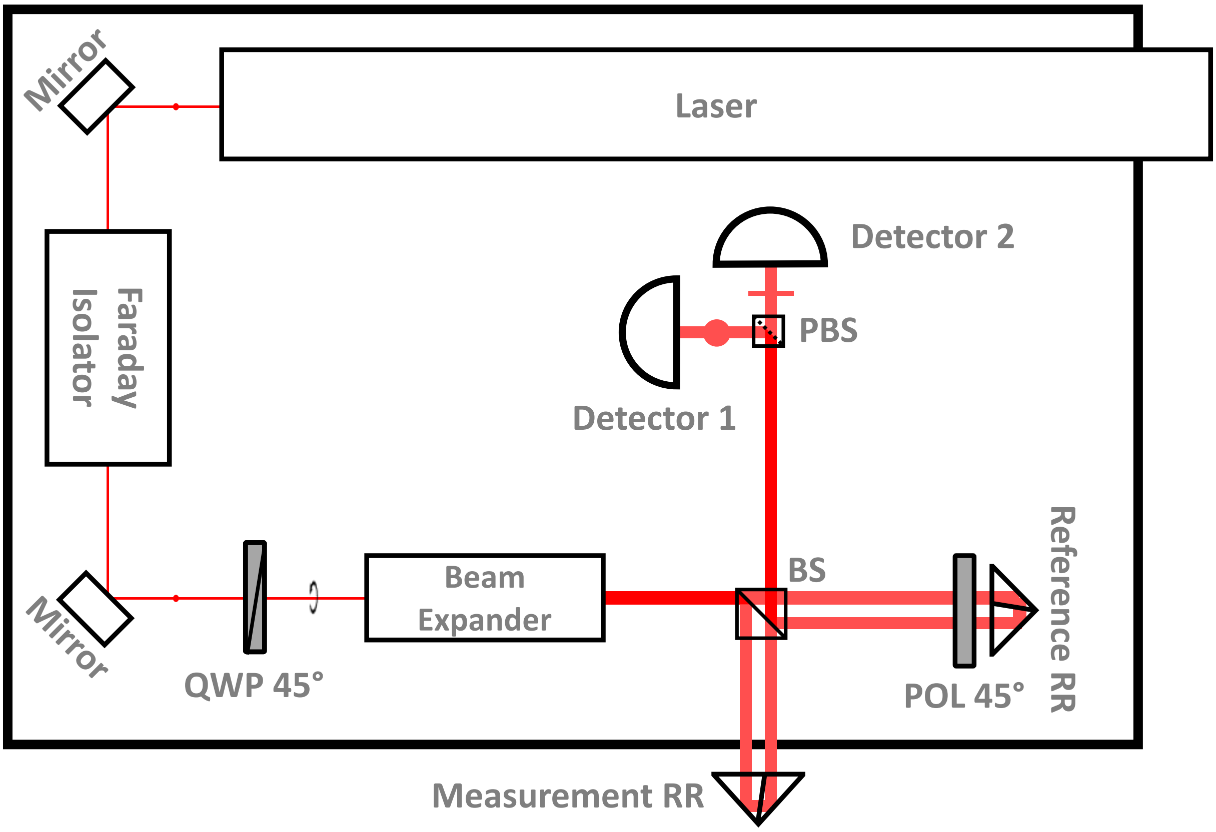

Figure 6.10: Schematic of the 3D model of the interferometer shown below, scaled 3/100.

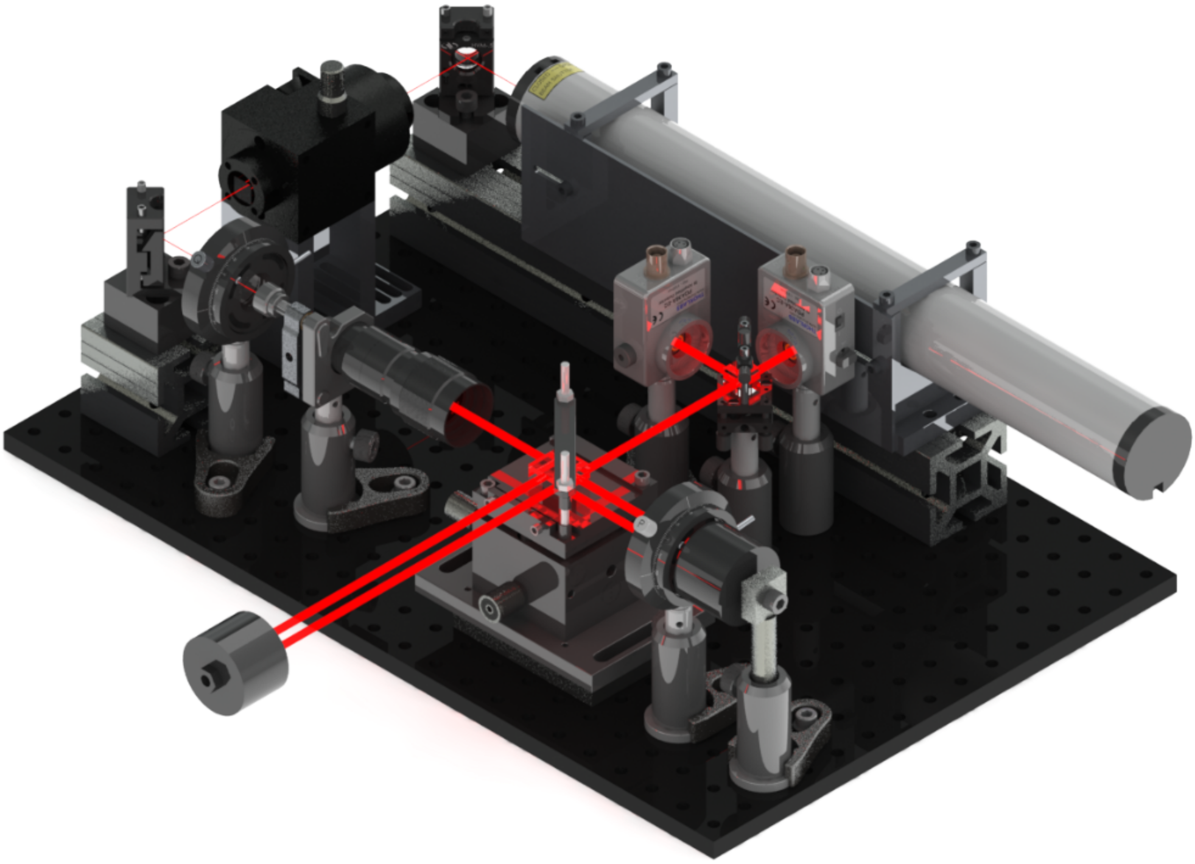

Figure 6.11: 3D model of the interferometer to be assembled.

6.3 Optomechanical System Implementation

Before describing the assembly of the interferometer it is essential to understand how the alignment of laser beams can be done experimentally, afterwards each step of the assembly is detailed. These are critical and complex steps that must be performed carefully in order to not introduce errors in the interferometer, particularly when verifying the polarization.

6.3.1 Laser Beam Alignment

In air a laser beam is not visible, which makes its alignment a complicated task. Knowing that a light beam always travels in a straight line it is possible to guarantee that the beam is aligned as desired in two different ways by using simple concepts of geometry.

The first alignment method used consists of determining the inclination of the beam by means of two longitudinal measurements. By placing an obstacle in the optical path of the beam and marking the position where it hits, we can verify if the beam is misaligned by displacing the obstacle in the direction of the alignment. If the beam does not hit the marked position it means that it is indeed misaligned, as is exemplified in figure 6.12a. As the distance between the two measurements increases so does the alignment error decrease, when performing this alignment it is ideal to measure the two positions as far apart as possible.

The second alignment method used is based in a phenomenon already discussed. If the reflections of an optical component are not superposed with the incident beam this means that the component is not perpendicular to the beam, as is exemplified in figure 6.12b. This method is easier to apply over short distances because the intensity of the reflections can be quite small.

The alignment of components that alter the beam's path such as the mirrors, the beam expander or the beamsplitter was done using the first method because it proved to be easier. However the alignment of components that do not alter the beam's path such as the polarizer or the quarter waveplate is impossible using the first method, so the second method was used for these components.

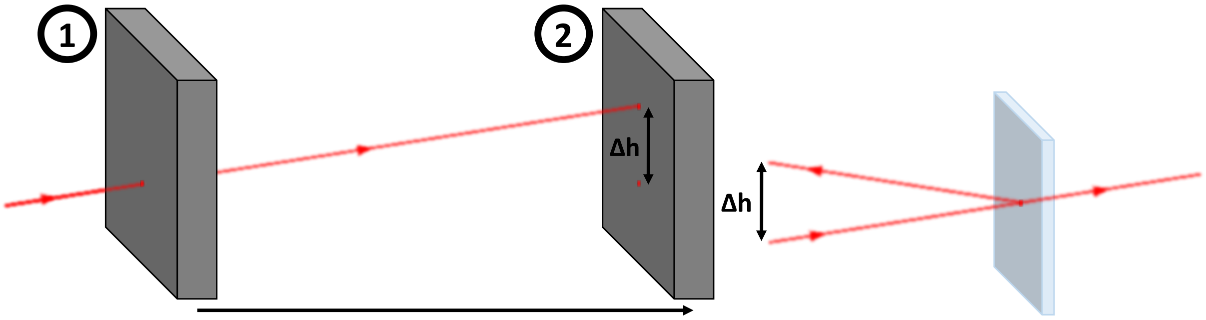

(a) Alignment through displacement.

(b) Alignment through reflection.

Figure 6.12: Two different methods to align a laser beam experimentally.

6.3.2 Interferometer Assembly and Integration

The first step towards assembling the interferometer, before placing the mechanical components, was ensuring that all the materials were ready to be assembled, this included the cutting of screws and also of the 50 mm height block to raise the mirrors and the laser. Once these tasks were done the block, the laser and mirror supports were secured to the optical table. To ensure in the following alignments that the optical table and the laboratory table were parallel they were screwed together.

Once the foundations had been placed it was possible to start introducing optical components in the assembly, beginning by placing the laser in its support. After tightening the laser and ensuring it was properly fixed the first alignment was performed to guarantee that the beam was parallel to the optical table. It was possible to conclude that the laser was tilted 0.4° upwards, as figure 6.13 shows.

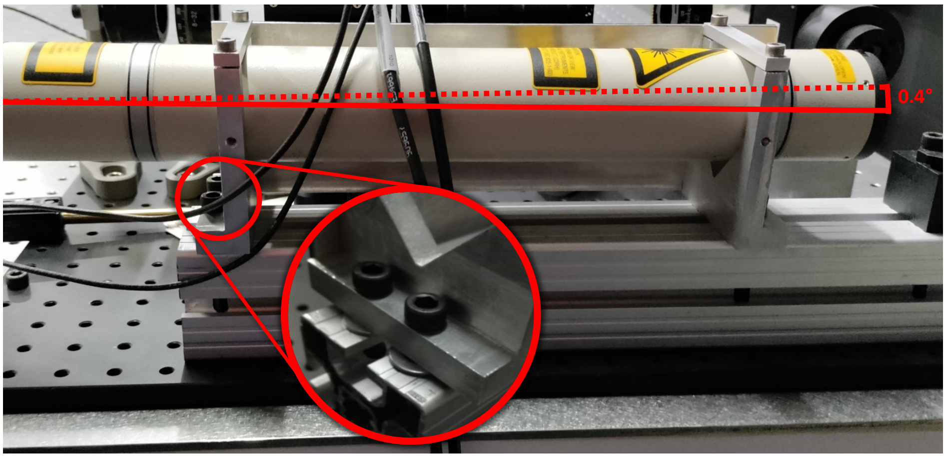

Figure 6.13: Alignment of the laser using washers to level the support. The tilt represented is exaggerated for better comprehension.

Since the length between the two extremes of the laser support is 200 mm it was calculated that the backside of the support needed to be raised 1.4 mm, but the washers available were 1.5 mm thick which was not ideal. Repeating the alignment showed that at the same distance the laser had a 1 mm height difference, which was not a problem because this inclination was corrected during the alignment of the mirrors.

The only concern when placing the mirrors was to guarantee that they were placed between two holes of the table, so that the reflected beam was also centered between two holes. After placing each mirror the first alignment was performed to ensure that there were no vertical or horizontal inclinations, the measured errors were corrected using the mirror support, shown in figure 6.14.

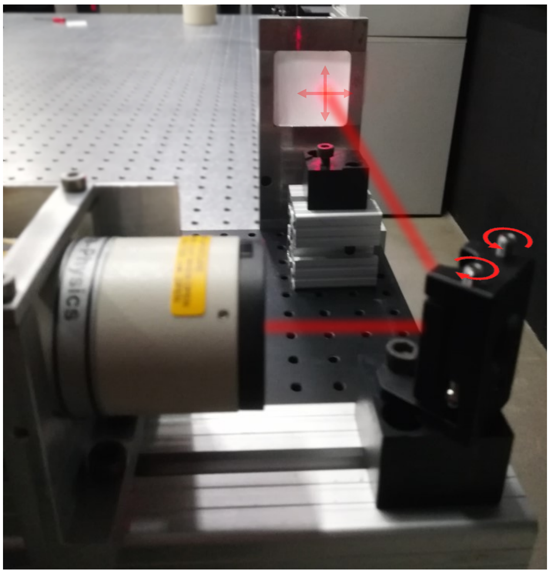

Figure 6.14: Mirror alignment using its support.

After both mirrors were positioned the Faraday Isolator was placed between them and was slightly tilted sideways so that the retroreflections would not fall into the laser cavity, as is shown in figure 6.15. Once the isolator was placed, with the help of a polarimeter the polarization was measured after the reflection on the mirror to ensure that it was vertical and finally the screw on top of the isolator was turned until a peak of irradiance was detected.

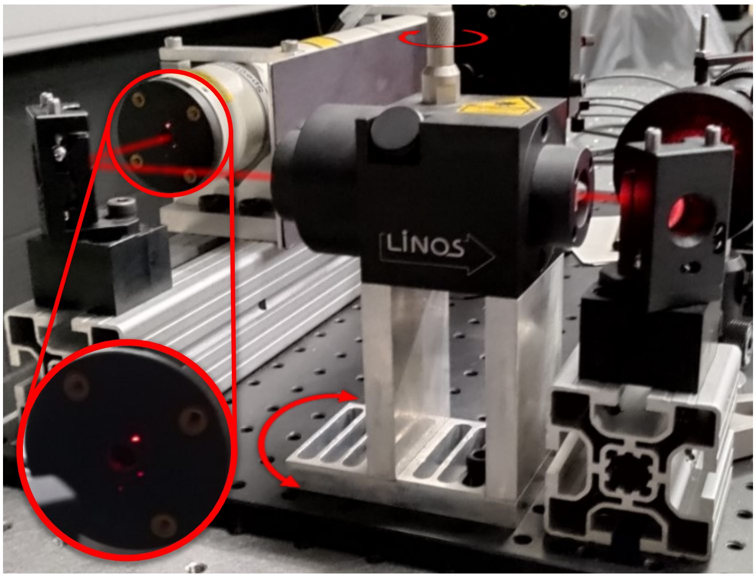

Figure 6.15: Alignment of the Faraday Isolator.

To place the reference arm's retroreflector it was necessary to guarantee that there was no height change in the laser beam and that the horizontal displacement was 10 mm so that the reflected beam was aligned with the holes of the table. To achieve this a cardboard sheet was placed after the mirror and two horizontal holes were made 10 mm apart, figure 6.15, to ensure that the beam was passing in the desired positions.

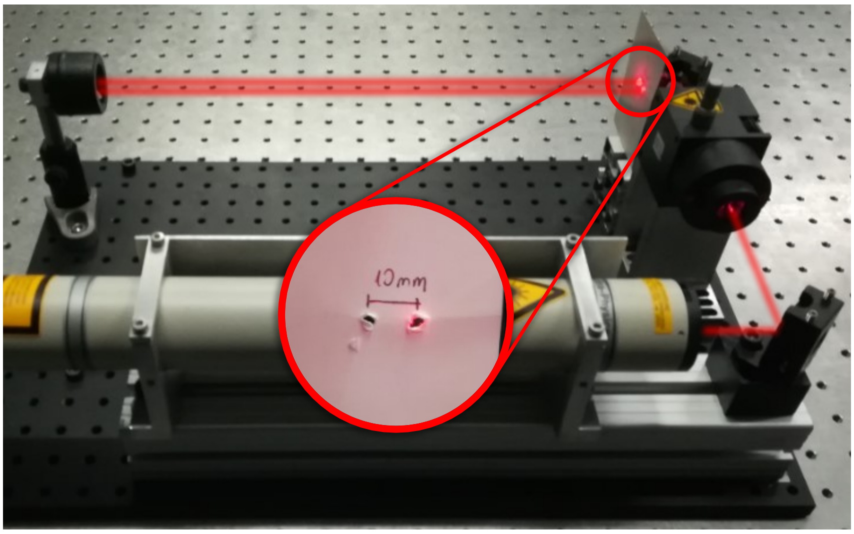

Figure 6.16: Alignment of the reference retroreflector.

There were a lot of degrees of freedom in the placement of the beamsplitter on the support. The first step to ensure a safe and sturdy placement was to guarantee the beamsplitter was positioned against the extremity of the support. To ensure that the incident beam was normal to the beamsplitter the second alignment was performed to confirm that the retroreflection was coincident with the incident beam. Afterwards the beamsplitter was displaced laterally along the edge of the support until the emerging beam hit the detector window, these steps are highlighted in figure 6.17. Finally, the first alignment was performed to correct the tilt of the measurement arm.

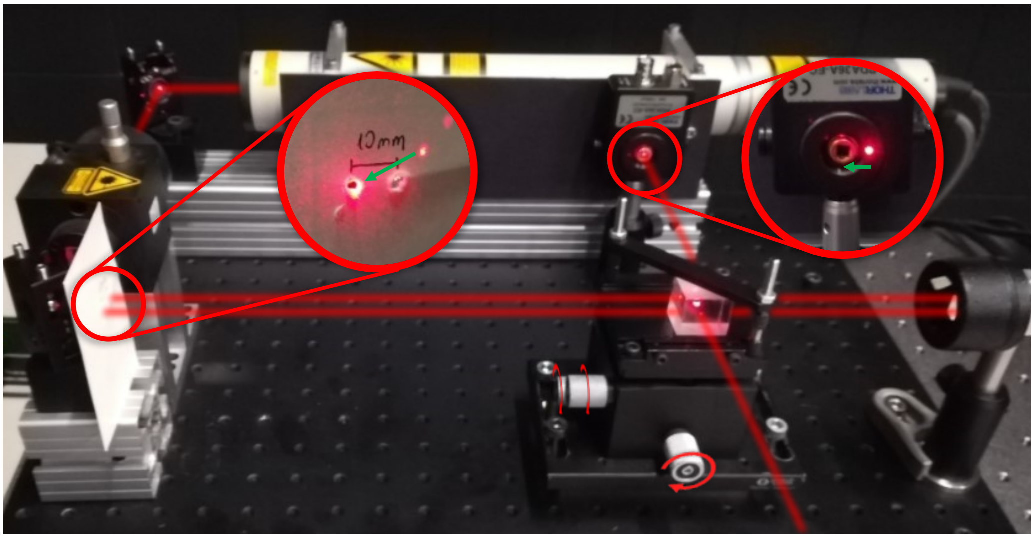

Figure 6.17: Alignment of the beamsplitter.

For the polarizations of the interferometer to be studied it was only necessary to assemble the measurement arm. This is the most important alignment since every time a new stage needs to be calibrated the measurement arm needs to be reassembled. At this point of the assembly with only one detector in place it was not possible to have much rigour in the placement of the measurement arm's retroreflector, but the only objective was to be able to measure the polarizations of each arm of the interferometer so the retroreflector was simply placed in a way that the emergent beam coincided with the detector's window and with the emergent beam of the reference arm.

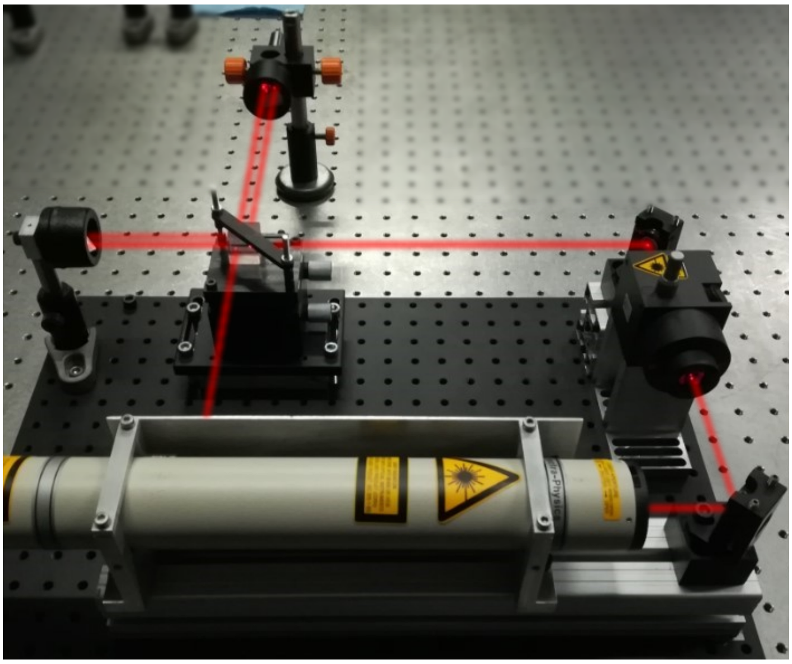

Figure 6.18: Introduction of the measurement retroreflector on a fixed external support.

The quarter waveplate and the polarizer used have a circular scale that was very helpful since the optical axis of the components cannot be seen with the naked eye. In order to know which angles in the scale of the quarter waveplate and the polarizer correspond to 0° and 45°, respectively, both components were tested and the conclusion was that the quarter waveplate's scale needed to be at 101° and the polarizer's scale at 220°.

After placing the quarter waveplate and the polarizer and performing the second alignment for both components to ensure that they were normal to the beam, the polarimeter was placed before the detection module to evaluate the polarization of both interferometer's arms. The measurements with the polarimeter presented some unexpected results, which indicated that the polarization was being changed by the beamsplitter and the retroreflectors so a study was made in order to understand how these components were altering the polarization of the light beam and how to minimize the effects, it is detailed in appendix C. After knowing the optimal components the retroreflectors were replaced and the beamsplitter was placed correctly in order to minimize the impact on the 45° polarization of the reference arm. Finally, the quarter waveplate was rotated until the beam of the measurement arm had a 90° phase difference after passing through the beamsplitter, the polarizations of the interferometer are shown in figure 6.19.

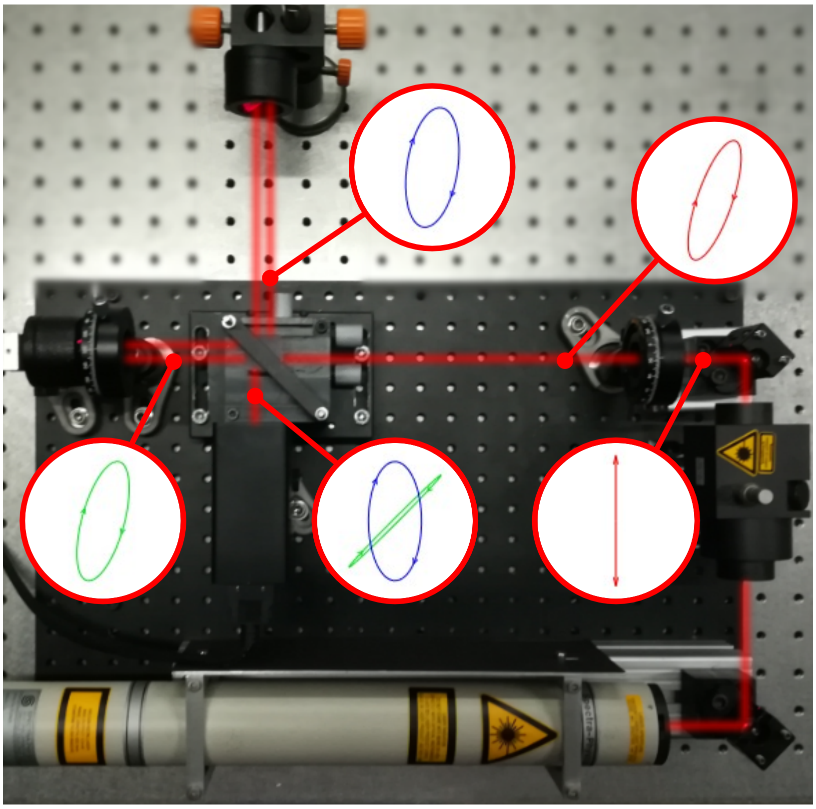

Figure 6.19: Polarizations along the interferometer in order to achieve quadrature.

Once the polarization was correctly defined, the polarizing beamsplitter was placed and aligned using the second method to correct the rotation and tilt of the support and ensure that it was normal to the incident beam. Finally, the last detector was placed in the path of the reflected beam from the PBS.

To complete the interferometer the beam expander was carefully placed, centered on the light beam, figure 6.20. To guarantee that it was not altering the beam's path the measurement arm was pointed at a target 4.5 m away and the beam expander was removed from the interferometer in order to confirm that the beam still hit the target in the same position.

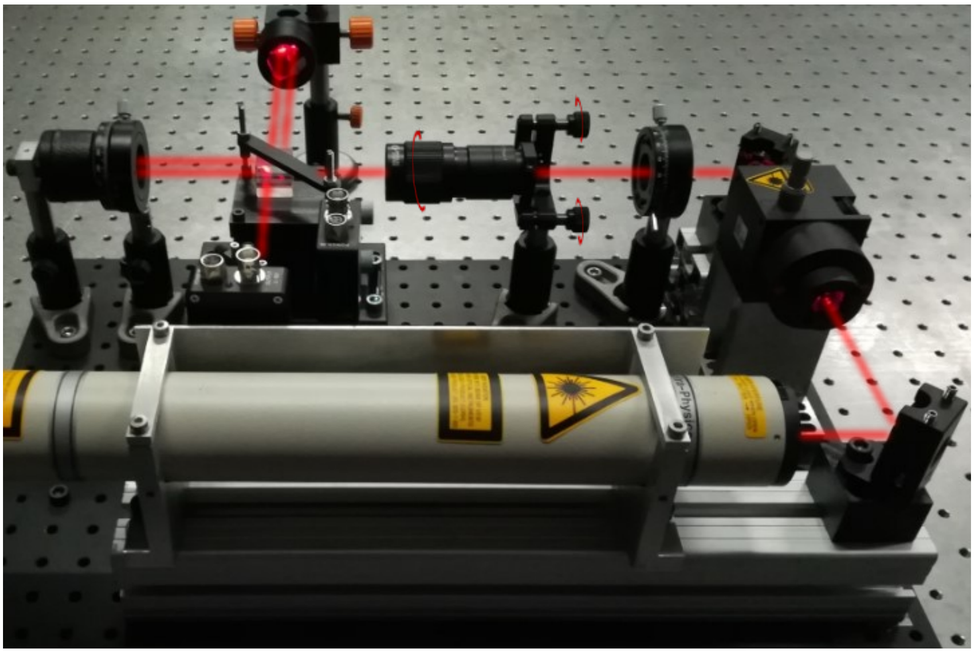

Figure 6.20: Placement and alignment of the beam expander.

6.4 Data Processing Software

The data acquisition and signal processing of chapter 5 was implemented in LabVIEW according to the block diagram represented in figure 6.21.

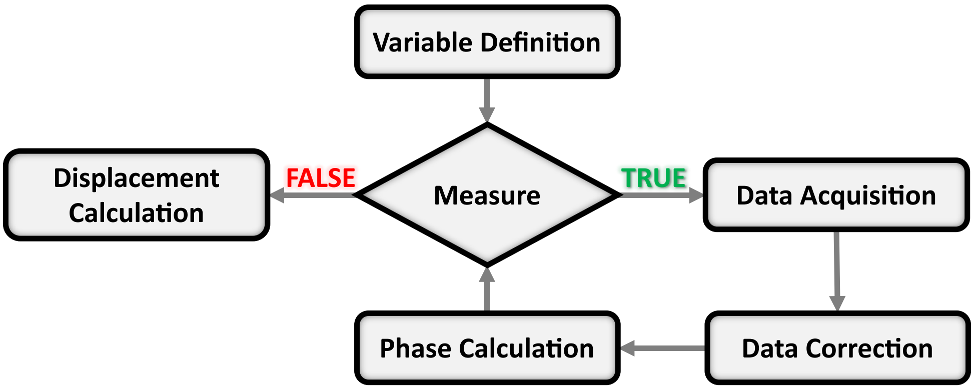

Figure 6.21: Implemented signal processing block diagram.

The LabVIEW code of figure 6.22 is an example of a simple data acquisition and signal processing tool using the NI 6366 data acquisition board, it is detailed below. Note that although the final version of the interface is essentially based on the following steps to calculate the displacement, many different tools were developed to ease the alignment of the measurement arm and to analyze the acquired data.

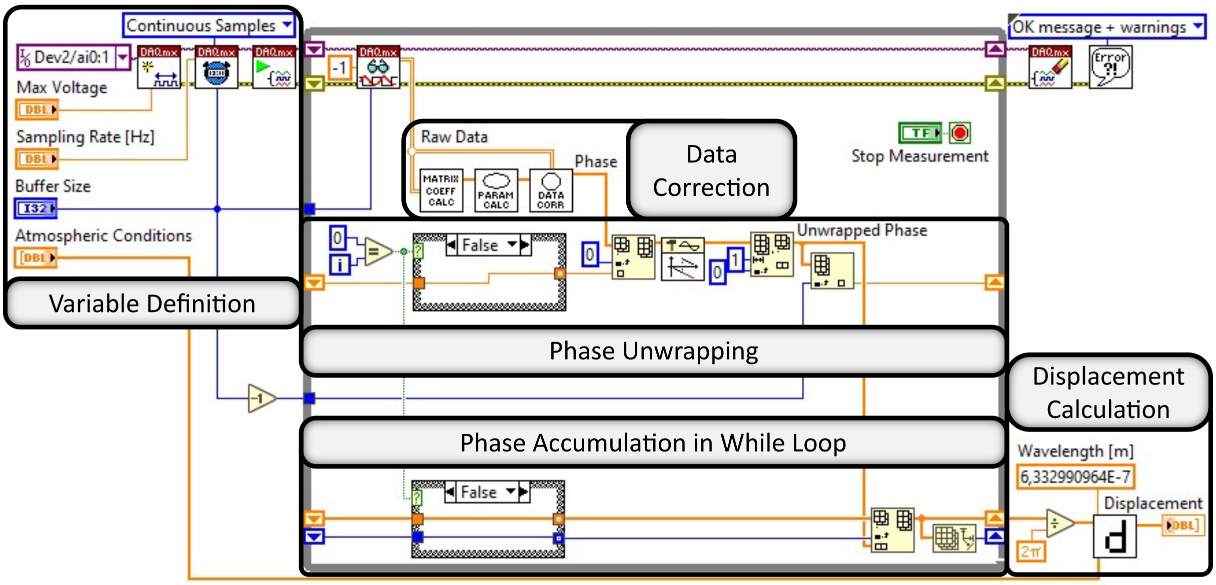

Figure 6.22: Simple implementation of the signal processing in LabVIEW.

6.4.1 Variable Definition and Data Acquisition

Before starting the measurements every system variable must be defined. This not only includes the atmospheric conditions (temperature, pressure and relative humidity) for the calculation of the refractive index, but also the sampling parameters, such as the channels in use, the maximum voltage, the sampling frequency and the data buffer size since the data is transferred in packages. After defining the variables the data is continuously acquired in a while loop until the user manually stops it.

This method to acquire the data continuously revealed a big disadvantage: if the calculations following the data acquisition take longer than the time necessary to acquire one data buffer then some information is lost. One solution to this problem is increasing the buffer size, this proved to be effective in chapter 8.

6.4.2 Data Corrections

With a 2D data array, where each dimension corresponds to the voltage of each detector, the signal processing was implemented. First, using equation 5.12 the elliptical fit is done over all the buffer data. Afterwards the ellipse parameters B, C, D and E are converted into our offset parameters r, α, q and p using equations 5.9a, 5.9b, 5.9c and 5.9d respectively. Finally using the calculated corrections the same data buffer is corrected and the phase is calculated with equation 5.15.

Since the offset parameters change with time the calculations need to be repeated every iteration of the loop. However, to recalculate the parameters over every data buffer it is necessary to guarantee that the amount of data in each buffer is significant, this means that in every data buffer there must be at least one full ellipse so that the elliptical fit is correctly calculated.

6.4.3 Phase Unwrapping

The phase unwrapping can be implemented according to equation 5.18 using the predefined functions in LabVIEW. The fact that these calculations were implemented in a loop created concerns with respect to the continuity of the phase because it must be continuous between iterations. This problem was solved by inserting the last element of the unwrapped phase array into the new wrapped phase array, and after performing the unwrapping this element is removed. To handle the first iteration of the loop a case was defined to set the first element as 0.

6.4.4 Displacement Calculation

The calculation of the displacement is given by equation 3.1. By knowing that the relationship between the number of fringes and the unwrapped phase is:

$$N_f = \frac{\delta_u}{2\pi} \tag{6.1}$$

We can transform the array of unwrapped phases into an array of number of fringes.

It is now only necessary to calculate the refractive index of the air, using equation 3.5, to turn the array of number of fringes into an array of displacements.

6.5 Chapter Conclusions

Starting with the assembly of a prototype to test the model to be assembled was excellent, otherwise the complications that were noticed in the prototype would have to be solved in the interferometer itself, which would have been complicated. It was also a very important stage in the debugging of the developed LabVIEW code. The assembly of the interferometer was a very strenuous process that took several days to accomplish, especially due to the unexpected problems that happened with the polarization. In spite of the difficulties, the developed 3D model helped considerably to understand and plan the alignment of several components.

After implementing and verifying the data processing software was working correctly the interferometer needed to be calibrated in order to determine the uncertainty of the measurements.

Chapter 7

Interferometer Calibration

In the tests performed before the calibration of the interferometer, when multiple translation stages were being used to test the developed LabVIEW code, the α parameter of the elliptical fit was varying with the velocity of the translation stages. The study of this effect is detailed in appendix D, where we ensured that the variations in the α parameter do not affect the measurements.

Several tests were performed to understand how external perturbations affected the interferometer and to evaluate if the stabilization of the system, after the attenuation of such perturbations, was affected. Once the perfect conditions to measure were defined the calibration of the interferometer was performed to determine the uncertainty of the number of fringes.

7.1 Interferometer Sensitivity to External Perturbations

For the calibration to be as correct as possible it was fundamental to comprehend how any external perturbation affected the system in order to know the ideal conditions to perform the calibration. There were two concerns when testing the interferometer, the first one was understanding how efficient the stabilization system of the optical table was in attenuating external perturbations. The second concern was understanding how high frequency noise affected the system. In all of the tests performed it was always necessary to have an initial displacement, defined as $20\,\mu\mathrm{m}$, to determine the best elliptical fit to the data, after the parameters were calculated they were never updated again and the external perturbations were recorded during 60 seconds.

To test the attenuation of “normal” external perturbations two measurements were performed, one during the day without using the optical table stabilization system, another during the night using the stabilization system, figure 7.1.

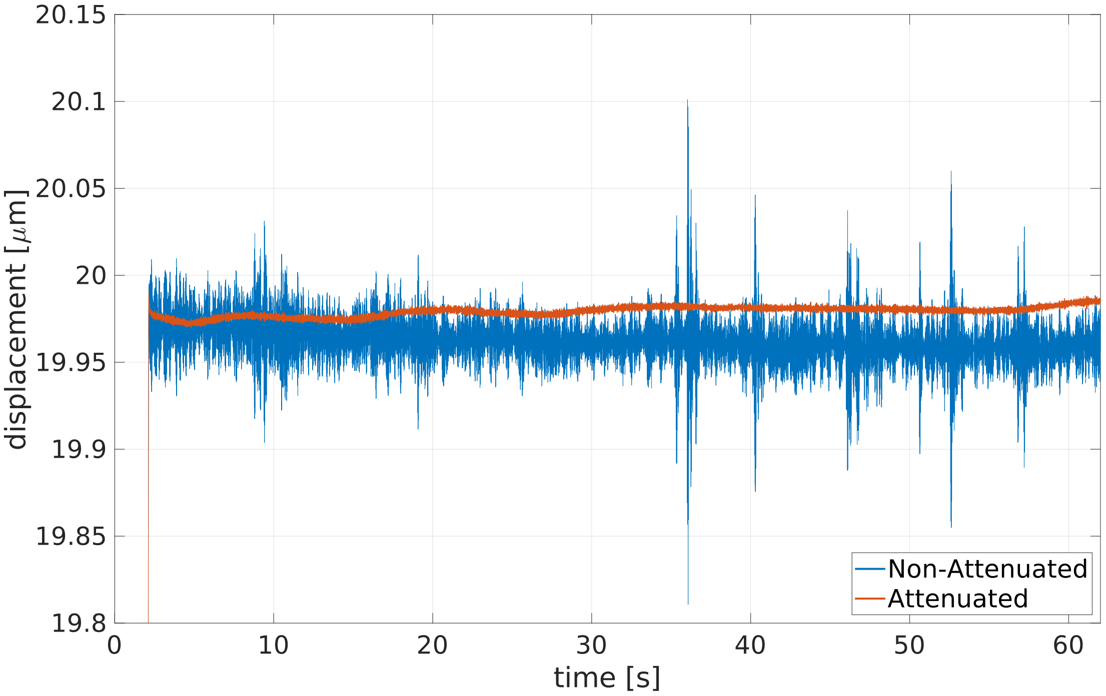

Figure 7.1: Testing of the stabilization system when subjected to external perturbations during the day (in blue) and when no perturbations were applied during the night (in orange).

In figure 7.1 the perturbations during the day are evident, this was caused by closing doors and dragging chairs on the floor above the laboratory. Considering this the calibration needed to be performed during the night when there were no people in the building.

To test the effects of high frequency noise two measurements were done with and without using the optical table attenuation system, where the optical table was tapped every five seconds, figures 7.2 and 7.3, respectively. When comparing the two figures it is evident that the attenuation system is good at eliminating low frequency noise, but high frequency noise is always present. Figure 7.3 also shows that the system did not stabilize on the same distance, which is incorrect. The frequency of the perturbation exceeded the sampling rate, causing the unwrapping algorithm to “skip” some fringes, thus it is essential that no collisions with the optical table occur during the measurement.

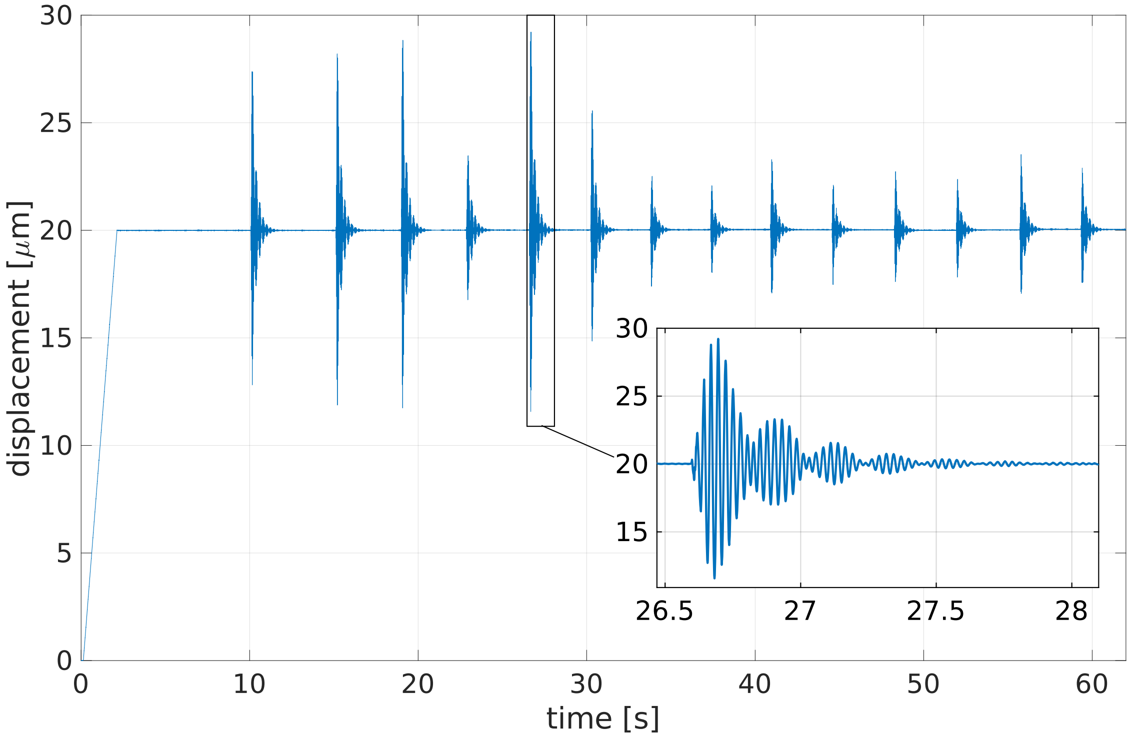

Figure 7.2: High frequency noise recorded by tapping the optical table while the attenuation system was not used.

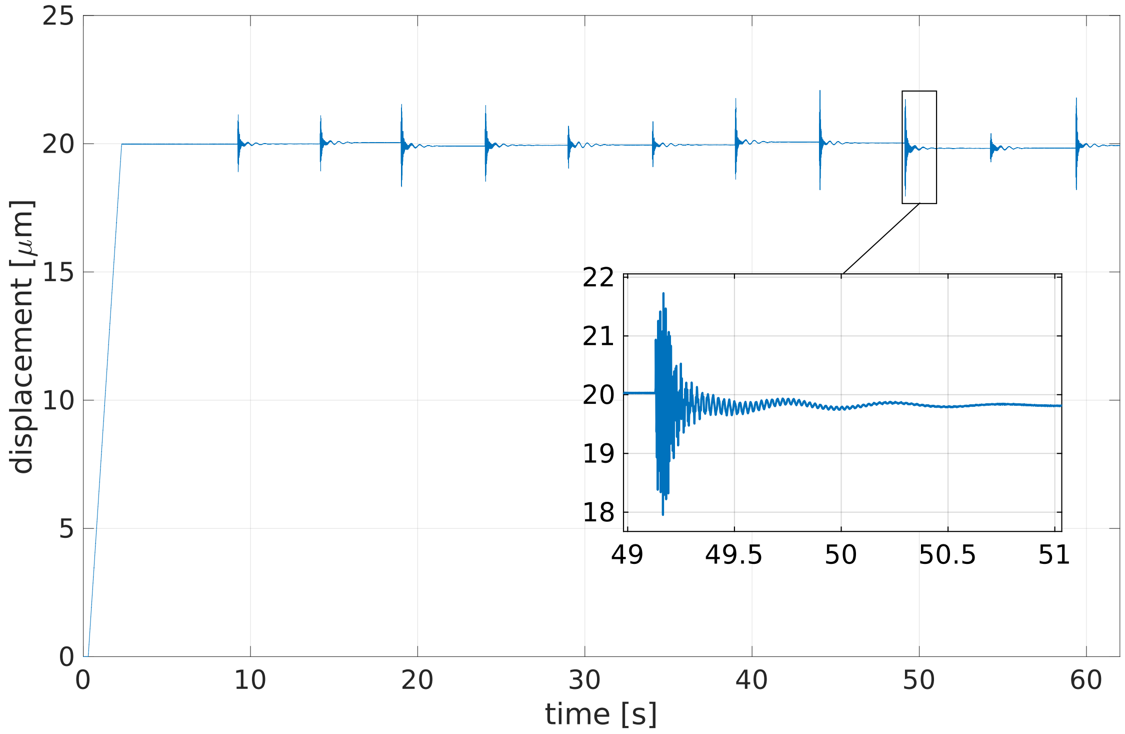

Figure 7.3: High frequency noise recorded by tapping the optical table while the attenuation system was in use.

During the measurements in the absence of perturbations the displacement drifted as the time increased, 14 measurements were performed to study this phenomenon, represented in figure 7.4.

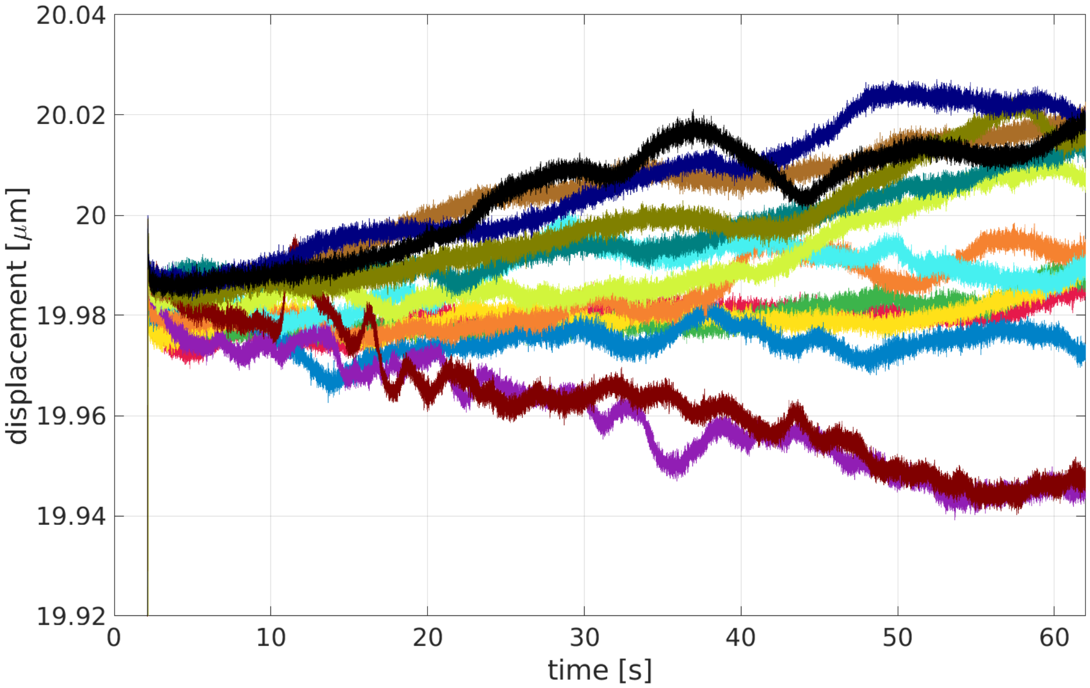

Figure 7.4: 14 measurements without applying any external perturbation to the system. Each color represents a different measurement.

These deviations are inherent to the system and tend to increase with time, but never exceed half a fringe, which was confirmed with a five minute measurement. The cause of these oscillations is not related to the system itself but to the atmospheric conditions because even with the optical table in study turned off there still existed some drift. This indicates that the measurements should be performed as quickly as possible to ensure that the high performance of the measurement instrument is not impaired by changes in the atmospheric conditions.

7.2 Calibration

The calibration of the interferometer had the purpose of determining the only unknown uncertainty in the system: the number of fringes. The uncertainty model represented in equation 3.2 reveals that the uncertainty of the number of fringes (U_{N_f}) is dominant in smaller displacements (under $100\,\mathrm{mm}$), because it is not multiplied by the number of fringes, contrary to the two uncertainties (U_n and U_λ) that dominate bigger displacements (over $100\,\mathrm{mm}$). This suggested that for the calibration to be as correct as possible the optical path difference between both arms of the interferometer needed to be as small as possible.

To correctly determine the uncertainty of the number of fringes not only was it necessary to have a small optical path difference between both arms of the interferometer, but it was also critical to know every other variable of the system. To monitor the ambient conditions the PCE-THB 40 thermo hygrometer barometer was used along with the Hart Scientific 1521 thermometer to have more rigour in the temperature measurement since it is an unstable parameter. The wavelength of the used laser, Model 117A of Spectra-Physics, was specified by the manufacturer and to ensure it was not varying during the measurements using a wavelength meter the wavelength was monitored for 10 minutes without noticing any changes. Finally, as a displacement standard the PI P-621.CD piezoelectric stage was used. To determine the uncertainty of the displacement the standard deviation of the measurements performed must be calculated.

7.2.1 Displacement Setup

The piezoelectric element used for the calibration had a maximum displacement of $100\,\mu\mathrm{m}$, however due to problems with impedance matching between the piezoelectric controller and the DAQ device used to inject the signal, we decided to limit the displacement at $80\,\mu\mathrm{m}$ in order not to damage the equipment and to ensure that the displacements were as precise as possible. The $80\,\mu\mathrm{m}$ were divided in 16 steps where measurements were performed.

Given that the relationship between the phase and the detector's voltage is not linear but an arctangent we had to ensure that the phase in each displacement corresponded to different positions in the range of the arctangent function, that is, each displacement was such that the $[0{,}2\pi]$ range was uniformly sampled. Since the measurement range was divided in 16 intervals, each displacement was defined as an integer multiple of a fringe plus 1/16 of a fringe.

Another concern was the monitoring of the atmospheric conditions during the measurements. It was defined that the pressure, temperature and relative humidity used for the calculations was the average between the start and the end of the measurements and that the respective uncertainties were half of the oscillation amplitude. If the atmospheric conditions did not vary then only the uncertainty of the measuring instrument was used. Although we attempted to mitigate the impact of fluctuations in the atmospheric condition in the measurements performed, the refractive index of the air will always fluctuate along the interferometer so it is wise to round the calculated uncertainty up as a safety measure.

50 measurements were executed with both interferometer arms having approximately with the same size ($12.5\,\mathrm{cm}$) in order to determine the uncertainty of the number of fringes.

7.2.2 Results

Figure 7.5 shows that the different steps performed by the piezoelectric stage have a Gaussian distribution, note that 9 outliers were excluded (values with a deviation to the mean over 3σ).

Since the standard deviation of all the measurements was $3.1\,\mathrm{nm}$, which for a confidence interval of 95 % represents an expanded uncertainty of $6.2\,\mathrm{nm}$, the initial uncertainty budget was used to estimate the necessary uncertainty of the number of fringes to achieve an uncertainty of $6.2\,\mathrm{nm}$ for the displacement. This process revealed that the uncertainty of the number of fringes is 0.0196 (almost 1 part in 50) for a 95 % interval of confidence (2σ).

According to the piezoelectric manufacturer the typical bidirectional repeatability of the stage is $1\,\mathrm{nm}$ (1σ) which would translate to an uncertainty of 0.006 (2σ) fringes. The uncertainty determined experimentally for the number of fringes of the interferometer was only 3 times bigger than the repeatability of the stage used so we were clearly influenced (but not limited) by the piezoelectric stage in the calibration. Nonetheless, since we did not have any better means to calibrate the system the uncertainty of 0.020 for the number of fringes was used, even though the interferometer can have a better performance, because this value was more than enough for the requirements defined in figures 1.1 and 3.1.

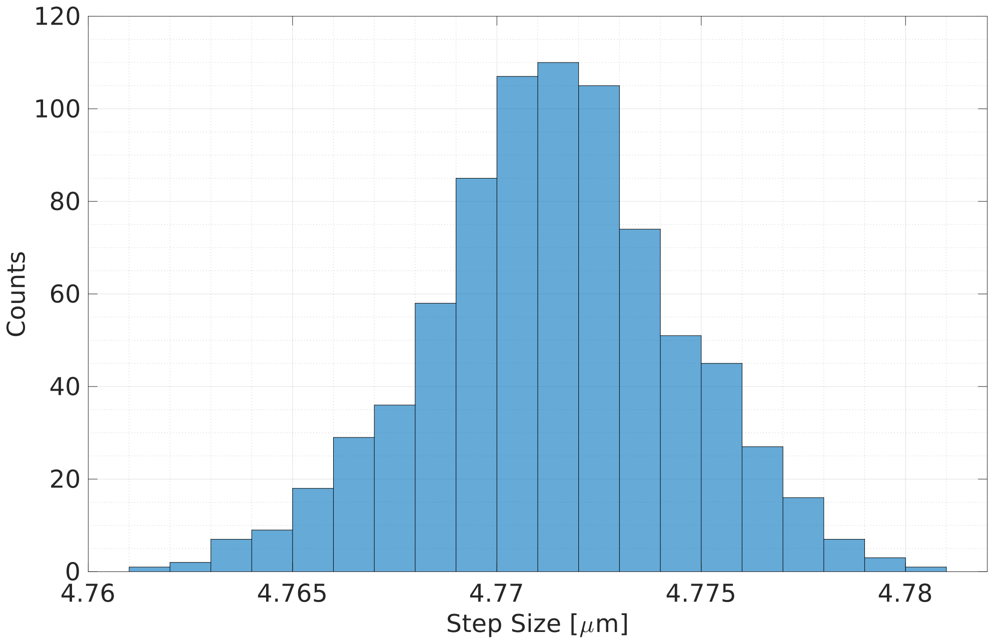

Figure 7.5: Histogram of each of the 791 displacements performed during the calibration.

Once all the uncertainties of the measurement system were determined the displacement uncertainty was be estimated as a function of the measuring distance, represented in figure 7.6, assuming the following ambient conditions:

- $P = (100.500 \pm 0.014)\ \mathrm{kPa}$
- $T = (20.00 \pm 0.28)\ ^{\circ}\mathrm{C}$
- $RH = (50.0 \pm 1.1)\ \%$

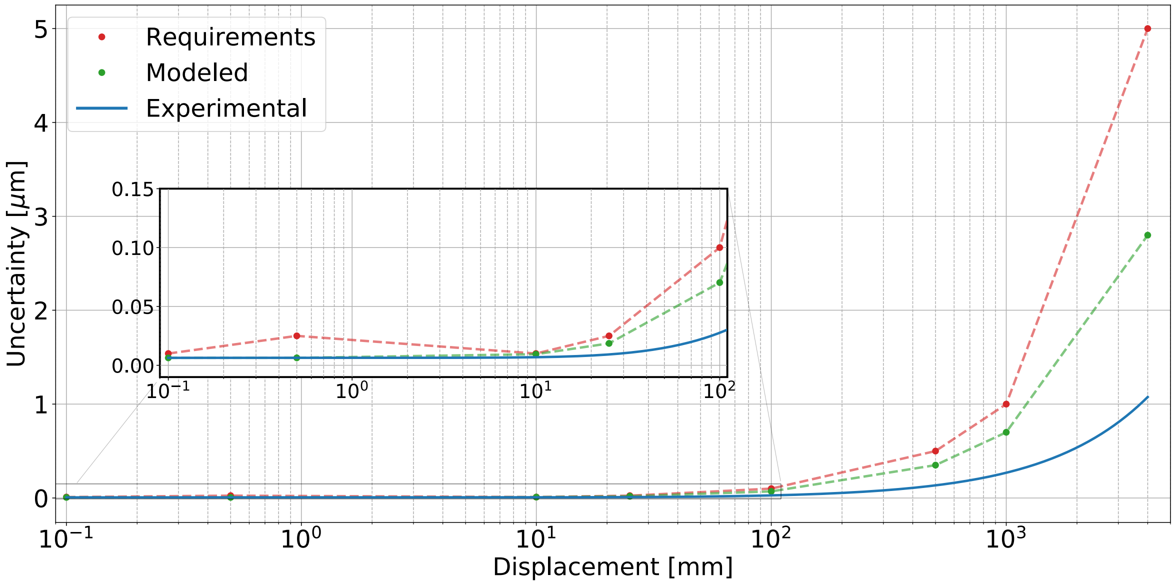

Figure 7.6: Experimental displacement uncertainty of the interferometer. We can also compare the requirements of figure 1.1 and the estimations of figure 3.1.

Figure 7.6 shows that the measurement uncertainty of the interferometer is even better than the estimations done in chapter 3, which is due to the uncertainty of the atmospheric conditions being smaller than was assumed.

7.3 Chapter Conclusions

Under normal conditions the system is not very sensitive to external perturbations, because walking around the optical table did not seem to affect the measurements, although care must be taken not to collide with the table otherwise the measurements are rendered useless. Outside vibrations and the echo provoked by loud noise in the laboratory do affect the system, but to a negligible degree when compared to the repeatability of the stages to be calibrated. Overall the calibration went better than expected, the piezoelectric stage used was only partially limiting the performance of the interferometer. However, as was mentioned, this is not a problem for the requirements set and that can be confirmed in figure 7.6.

Having the measurement system calibrated and ready to operate the only remaining task was to calibrate the translation stages available in the laboratory.

Chapter 8

Translation Stage Calibration

Having defined the uncertainties related to the measurement, to calibrate any translation stage only the repeatability must be determined. In order to represent the vast range of translation stages available in the market, several stages with a different travel range and performance were calibrated. There are two steps to calibrate any translation stage: first and foremost, the repeatability of the origin (or home position) needs to be determined to understand if there will be problems once the stage is restarted. Secondly the repeatability of displacements along the stage's course needs to be determined and should always be bigger than the origin's repeatability.

The home position is often times defined by an optical or magnetic sensor in the translation stage designed for this sole purpose. The error of the home position is given by the difference between any displacement forward and backward to the home position (not to the 0 position, otherwise the magnetic/optical sensor is not used), by repeating this test multiple times the origin repeatability is given by the standard deviation of the difference between both displacements. To characterize the displacements along the stage's course we defined that each stage should be divided in 10 steps, each one a multiple of one tenth of the stage's range. For each of this steps the measurements were repeated 25 times in both directions to have an estimate of the bidirectional repeatability and to verify if there existed any hysteresis.

To display the displacement of any stage we chose to represent the error, defined as the difference between the measured displacement and the expected displacement, as a function of the expected displacement for better visualization of the stage's characteristics. Since the measurements were performed forward and backward (relative to the home position) we acquired positive and negative displacements, respectively. After the displacement error of each stage was known this quantity was minimized by adjusting the stage's encoder by 1 plus the slope of a linear fit to the error (the slope is summed by one because we do not display displaying the measured displacement in the figures). To further minimize the errors and completely eliminate the systematic errors of the stages a lookup table could be made for each stage.

Besides the calibration, some stages were also subjected to load tests in order to understand how the effect of having weight over the stage affected the displacement. Another stage was also subjected to velocity tests, not only to test the impact of the increase in velocity in the displacement, but also to test the limits of the data acquisition system of the interferometer.

8.1 PI's P-621.CD piezoelectric stage

In the calibration of the piezoelectric element used to characterize the uncertainty of the number of fringes we were limited by the uncertainty of the measurement, however we did verify that there were offsets between the expected position and the measured position. Since the signal that controlled the movement was being injected externally in the stage's controller for this particular case the home position corresponded to 0 V, the same as the 0 μm position, thus only the bidirectional repeatability was analysed.

On the following graph and in all the performed tests we display the repeatability in red (random uncertainty), the interferometer measurement uncertainty in green (systematic uncertainty) and the final uncertainty in blue. In the calculation of the final uncertainty the repeatability is reduced by averaging, according to [1] and [17]. All the uncertainties correspond to a confidence interval of 95% (2σ).

The displacements of figure 8.1 were performed 25 times in multiples of 10 μm at a velocity of 10 $\mu\mathrm{m/s}$, forward and backward.

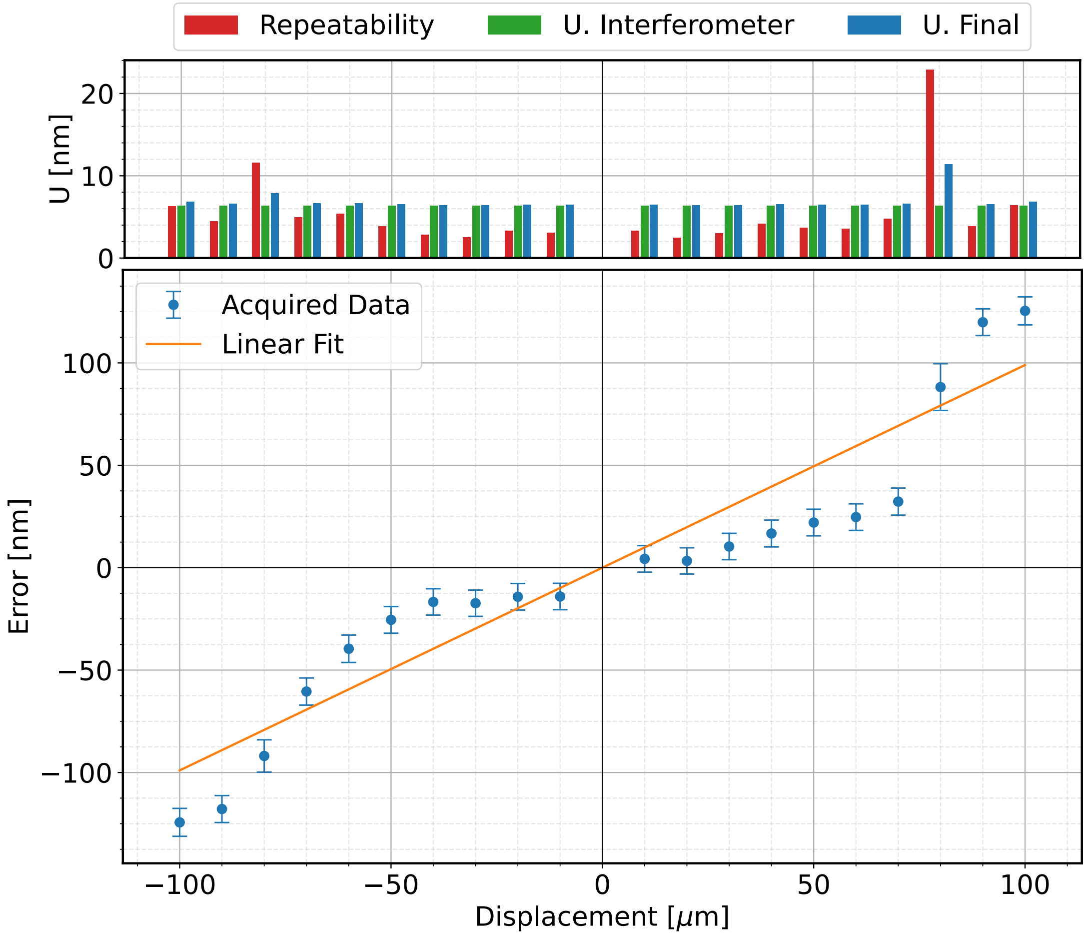

Figure 8.1: Displacement error of the P-621.CD stage. The linear fit is: $\mathrm{Error[nm]} = d[\mu\mathrm{m}]\,(0.99{\pm}0.08)$

Figure 8.1 shows that the error increases with the displacement and it is not symmetric, to better visualize this phenomenon we can mirrored the backward displacement and overlapped both directions of the movement, represented in figure 8.2, where hysteresis can be observed.

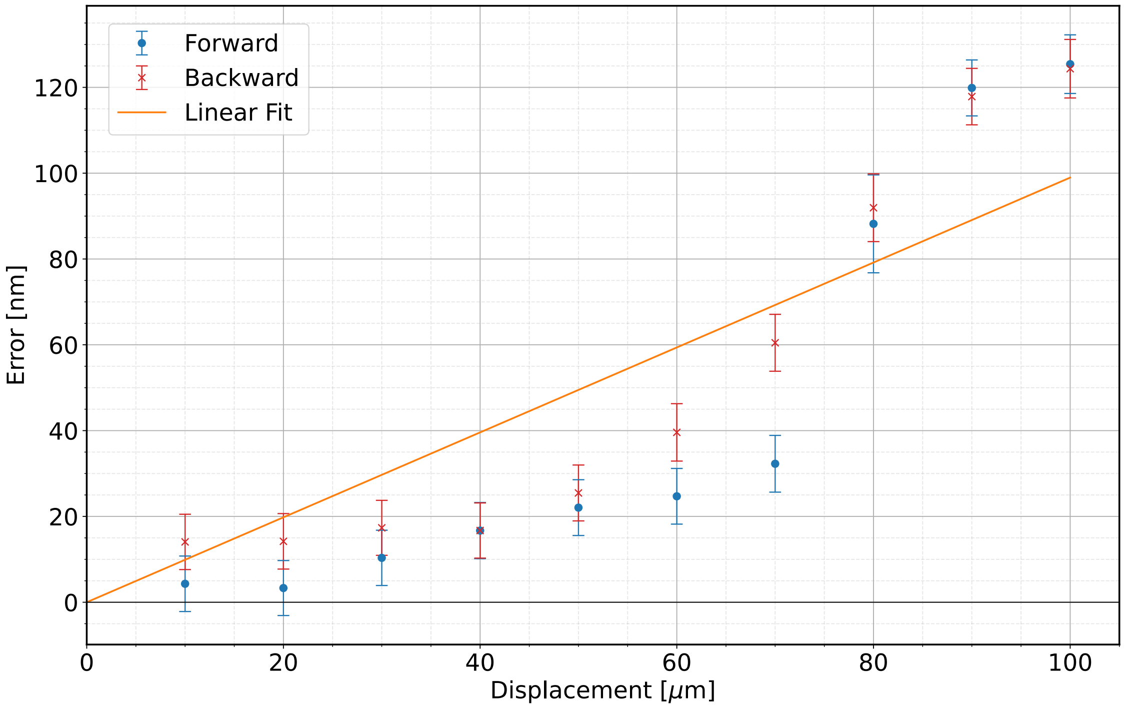

Figure 8.2: Overlapped error of the P-621.CD stage, similar to figure 8.1 but the backward displacement is mirrored to visualize the hysteresis. The linear fit is: $\text{Error[nm]} = d[\mu\text{m}]\,(0.99 \pm 0.08)$

By performing a linear fit to the data, which is forced to intercept the origin, we determined the relationship between the stage's displacement and the expected displacement. To reduce the error the stage's encoder value must be multiplied by 1 plus the slope of the linear fit. For this stage, the encoder value must be multiplied by 1.00099, which would yield the corrected error represented in figure 8.3.

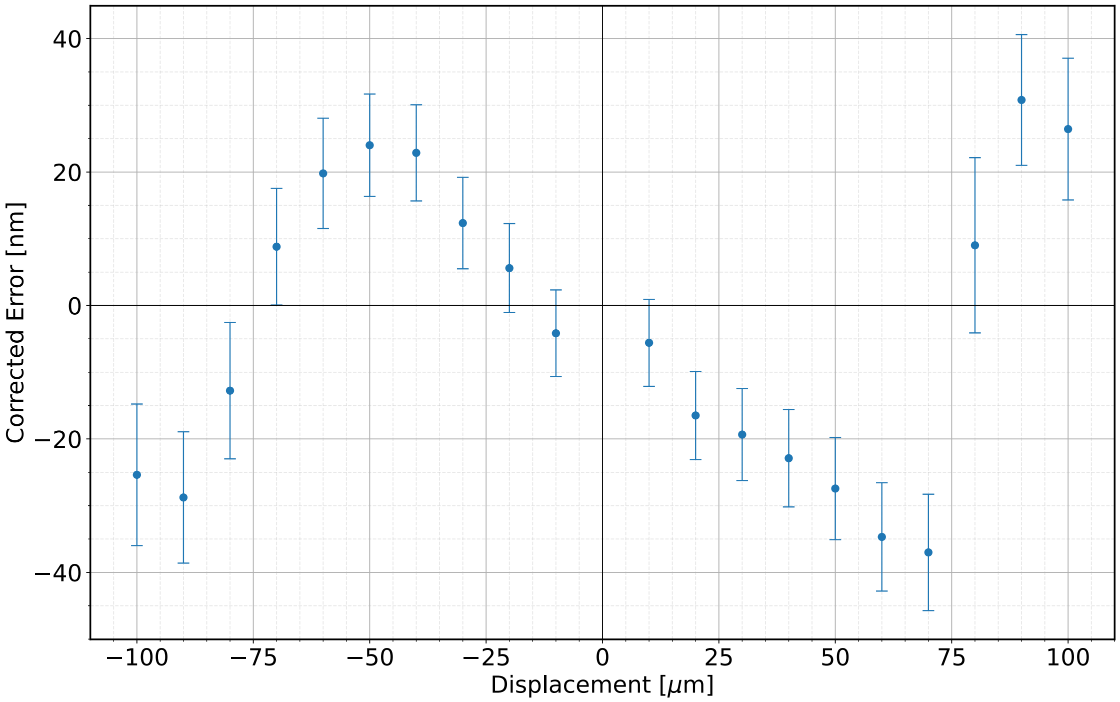

Figure 8.3: Displacement error of the P-621.CD stage after applying the corrections to the stage's encoder.

Although the error of figure 8.1 was not exactly linear, we reduced the maximum error from 125 nm to 37 nm. Gathering all the acquired data we can compare the measured parameters with the manufacturer's specifications in table 8.1

Table 8.1: Comparison of the measured parameters of PI's P-621.CD piezoelectric stage and the values specified by the manufacturer.

	Measured	**Manufacturer**
Repeatability [nm]	23	1
Largest Error [nm]	125 ± 7	-
Conversion Factor Correction	1.00099	-
Largest Error with Correction [nm]	37 ± 9	-

As we can see in table 8.1 we did not have much information about the translation stage, only the repeatability was known. Although the worst measured repeatability was 23 nm this was an outlier because during the calibration of the interferometer the repeatability near 80 $\mu\mathrm{m}$ was 7 nm, which would have been the repeatability of the stage (excluding the outlier). Figure 8.1 reveals, as expected, that the uncertainty was limited by the interferometer and not by the repeatability of the stage, this was the only translation stage where we this problem surged.

8.2 Newport's MFA-CC stage

This translation stage was used in Inês Leite's master's thesis [26] in which the uncertainty of the methods used was partially limited by the absolute accuracy and repeatability of the translation stage. By performing a displacement of $1\,\mathrm{mm}$ and sending the stage back to the origin 25 times, we verified that the home repeatability was $76\,\mathrm{nm}$, which is much smaller than the $2.5\,\mu\mathrm{m}$ indicated by the manufacturer.

The measurements of figure 8.4 were performed 25 times for each of the 10 steps, at a speed of 1 $\mathrm{mm/s}$.

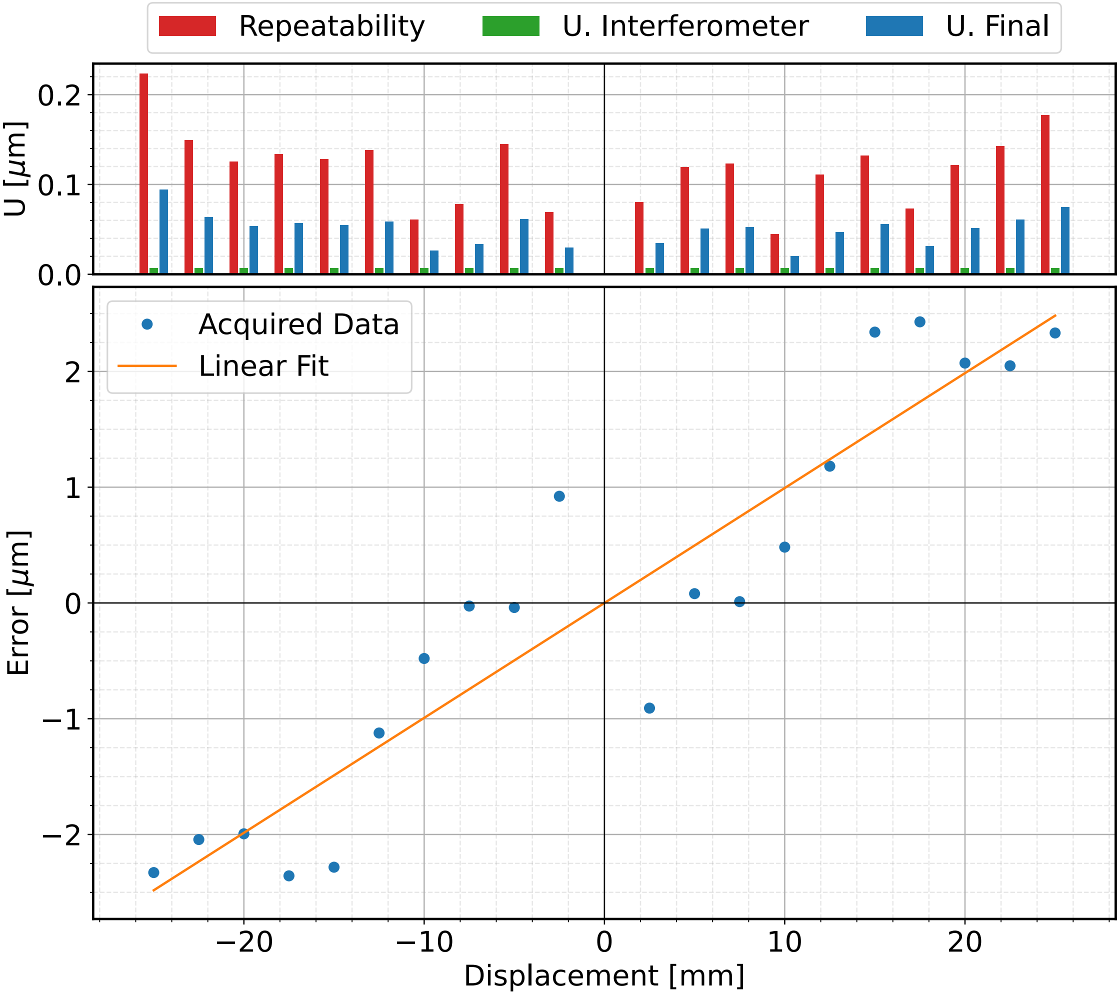

Figure 8.4: Displacement error of the MFA-CC stage. Note that the error bars are considerably small and cannot be represented in the lower graph. The linear fit is: $\mathrm{Error}[\mu\mathrm{m}] = d[\mathrm{mm}]\,(0.099 \pm 0.009)$

Although the error shown in figure 8.4 is not exactly linear we can see that both directions of the movement have a symmetric error. The maximum error is $2.4\,\mu\mathrm{m}$, which is still within the manufacturer's specifications ($3\,\mu\mathrm{m}$), nonetheless by multiplying the encoder value by 1.000 099 we can still reduce the error and obtain the new values represented in figure 8.5.

After the corrections the maximum error becomes $1.2\,\mu\mathrm{m}$, which is half of the previous error and approximately 3 times better than the value specified by the manufacturer.

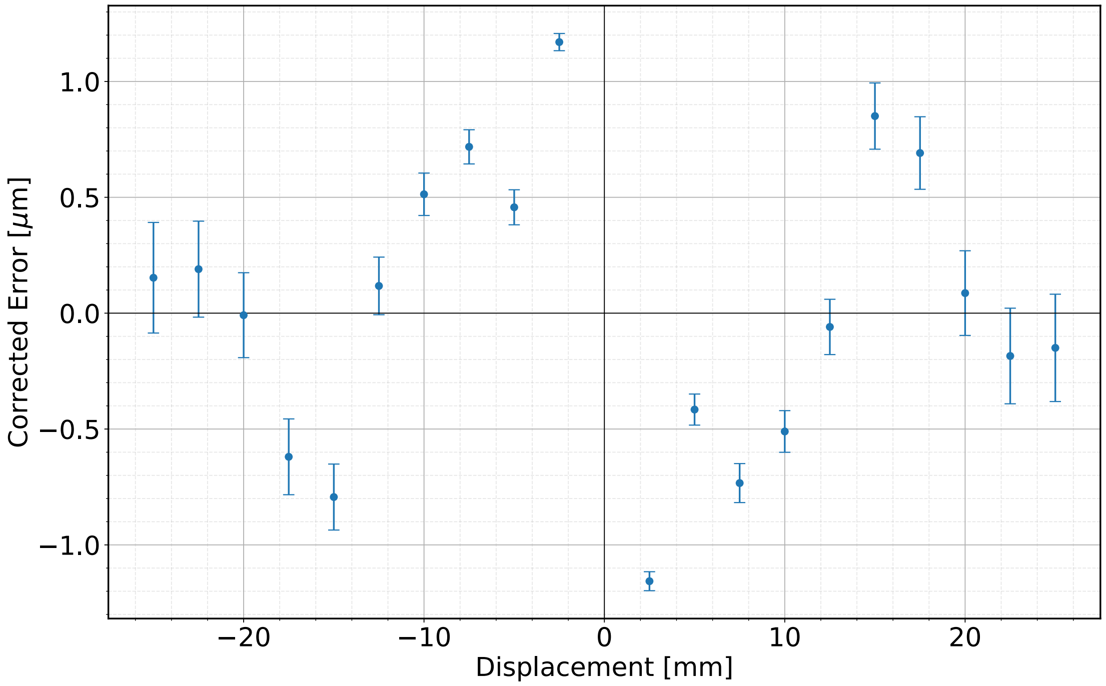

Figure 8.5: Displacement error of the MFA-CC stage after applying the corrections to the stage's encoder.

Table 8.2: Comparison of the measured parameters of Newport's MFA-CC stage and the values specified by the manufacturer.

	Measured	**Manufacturer**
Home Repeatability [nm]	76	2 500
Repeatability [nm]	223	750
Largest Error [nm]	2 428 ± 32	-
Conversion Factor Correction	1.000 099	-
Largest Error with Correction [nm]	1 170 ± 37	3 000

As we can see in table 8.2 the stage performed much better than specified by the manufacturer, not only on the home repeatability but also on the absolute accuracy and repeatability of the displacements. With this new knowledge of the accuracy and precision of the movement the uncertainty of the method used by Inês would have been smaller.

8.3 PI's VT-80 stage

The VT-80 stage was used in Guilherme Roque's master's thesis [27] and will be integrated in an international project. During Guilherme's work and in the following calibration some irregularities were noted in the movement of the stage, we concluded later that this problem was related to the fact that this stage was loosened in order to work properly in dry conditions with low accuracy requirements. Now that the stage is operating at "normal" atmospheric conditions it was too loose which caused some wobbling. To better diagnose this condition another stage of the same model was calibrated in order to confirm that the measurement instrument was not introducing any error in the measurements. To distinguish both stages named them according to their serial number (SN): the one used by Guilherme had a SN 81 and the other one had a SN 79.

Regarding the origin repeatability, the measurements were performed between the origin and the 20 mm at a velocity of $10\,\mathrm{mm/s}$, and were repeated 25 times for each stage. The values obtained for the origin repeatability were $0.4\,\mu\mathrm{m}$ for the stage SN 79 and $0.6\,\mu\mathrm{m}$ for the stage SN 81. The calibration was also performed at $10\,\mathrm{mm/s}$ and every step was repeated 25 times. After doing the usual 10 steps we decided to measure 12 more displacements closer to the origin to better characterize the increase in the error that is shown in the "RR in corner" plot of figures 8.6 and 8.7.

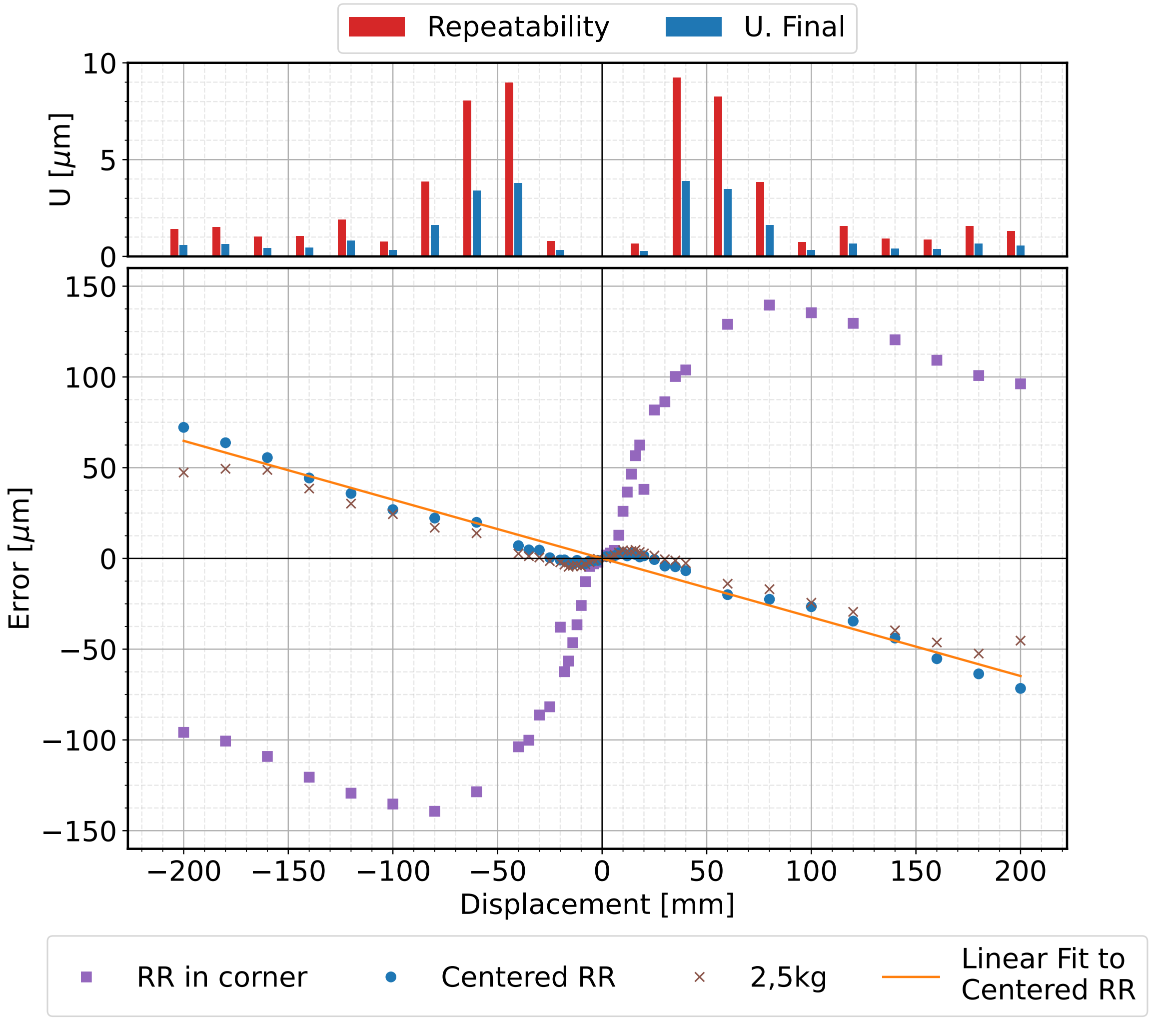

Figure 8.6: Displacement error of the VT-80 SN 79 stage.
The linear fit is: Error[μm]=d [mm] (-0.32±0.01)

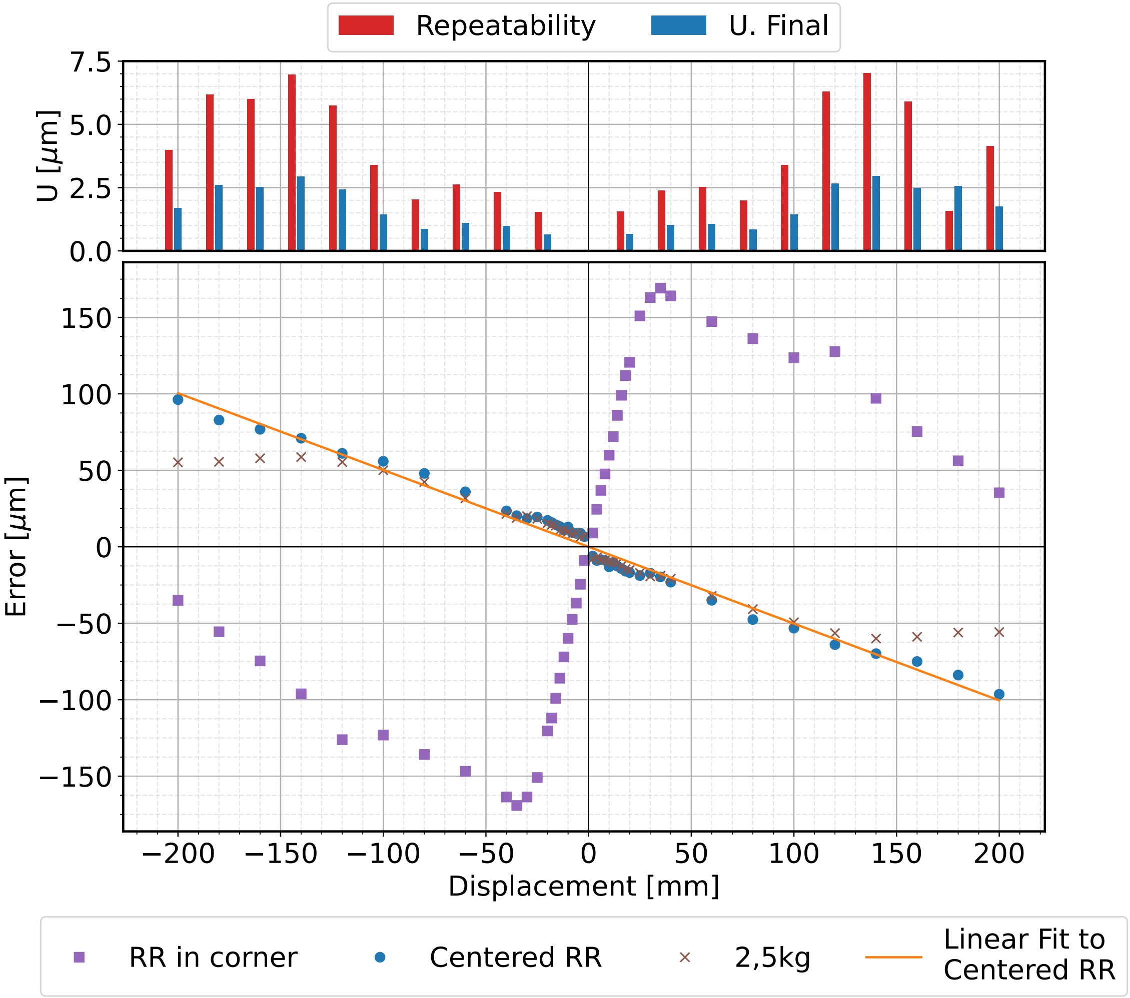

Figure 8.7: Displacement error of the VT-80 SN 81 stage.
The linear fit is: Error[μm]=d [mm] (-0.50±0.01)

After some consideration we decided to repeat these measurements with the retroreflector centered above the stage instead of it being fixed to a corner, and afterwards by applying half the maximum load over the stage (2.5 kg), which is represented in the "Centered RR" and "2.5 kg" plots of figures 8.6 and 8.7. The different positions and conditions of the measurements are shown in figures 8.8a, 8.8b and 8.8c.

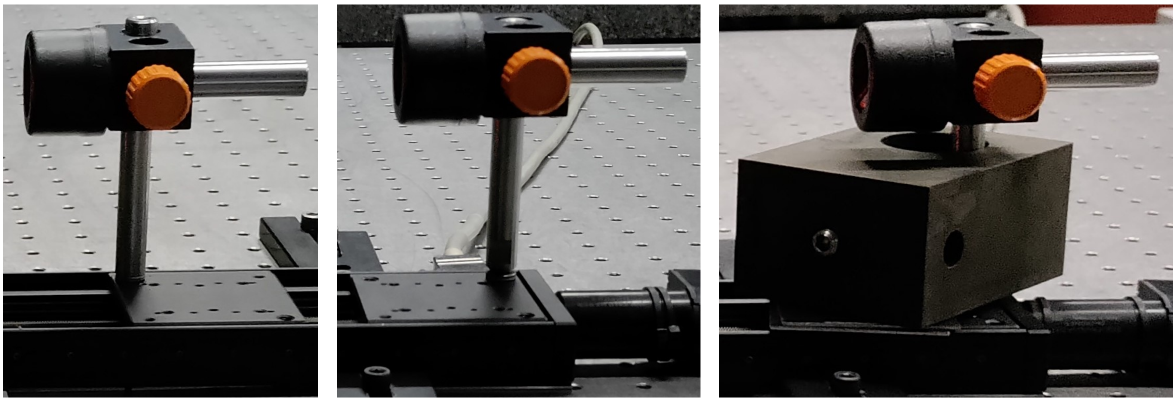
(a) RR in corner.

(b) Centered RR.

(c) 2.5 kg.

Figure 8.8: Different conditions of the measurements performed in figures 8.6 and 8.7.

The data represented in figures 8.6 and 8.7 suggests that the weight distribution over the stages is more important than the amount of cargo. As we can see the error is almost linear when the retroreflector was centered above the stage, so using the slope of both linear fits we can correct the encoder value and achieve the errors displayed in figures 8.9 and 8.10.

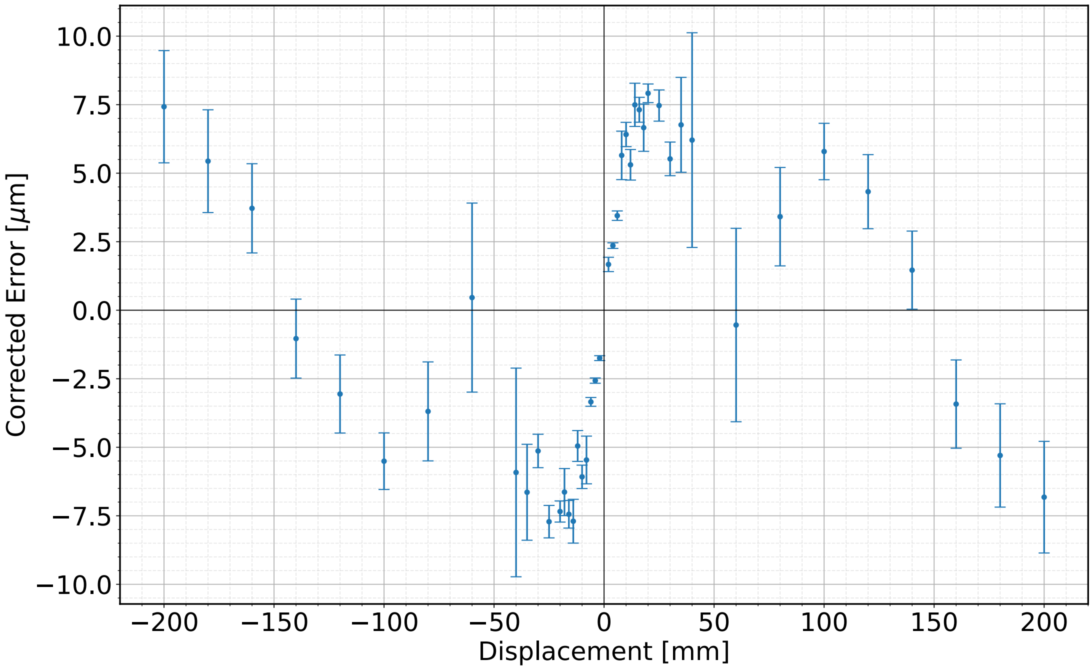

Figure 8.9: Displacement error of the VT-80 SN 79 stage after applying the corrections to the stage's encoder.

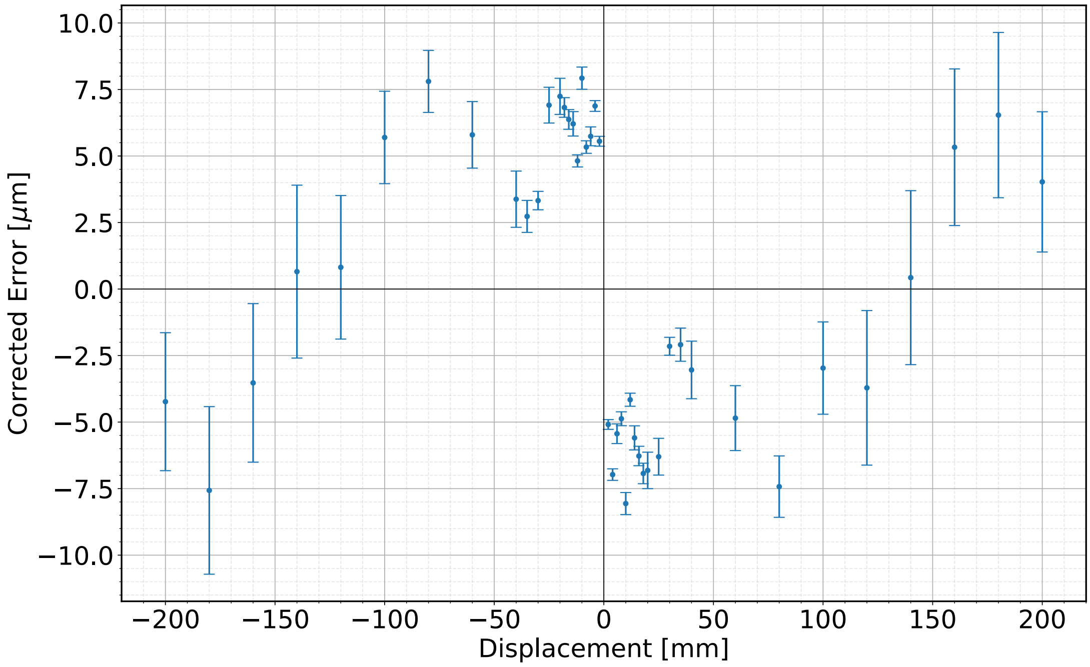

Figure 8.10: Displacement error of the VT-80 SN 81 stage after applying the corrections to the stage's encoder.

After the corrections to the encoder values the maximum error of both stages is about $10\,\mu\mathrm{m}$ (when considering the uncertainties), with a repeatability of $9.3\,\mu\mathrm{m}$ for the SN 79 stage and $7.1\,\mu\mathrm{m}$ for the SN 81 stage.

Table 8.3: Comparison of the measured parameters of PI's VT-80 stages and the values specified by the manufacturer. The values of the largest error are relative to the "Centered RR" plots of figures 8.6 and 8.7.

	SN 79	**SN 81**	**Manufacturer**
Home Repeatability [nm]	378	567	-
Repeatability [nm]	9 288	7 073	10 000
Largest Error [nm]	72 210 ± 590	96 400 ± 1 800	-
Conversion Factor Correction	0.999 68	0.999 50	-
Largest Error with Correction [nm]	6 200 ± 3 900	7 600 ± 3 200	-

When evaluating both stage's specifications we can once again see that the knowledge we had about the performance of this model of stages was scarce. Due to all the irregularities of these stages they were very hard to align with the interferometer, nonetheless we still managed to conclude that even after loosening the stages they still comply with the repeatability indicated by the manufacturer. This calibration was interesting because even though we were executing longitudinal measurements we can see that the angular behaviour of the stage (wobbling) was not ideal due to the changes of the position of the retroreflector over the stage during the displacement.

8.4 Newport's M-IMS300PP stage

This stage from Newport was the best stage available in the laboratory because it allowed accelerations of up to 400 $\mathrm{mm/s^2}$, velocities of 100 $\mathrm{mm/s}$, displacements of 300 mm and it also supports a load of 60 kg. Due to these extraordinary capabilities this stage was a candidate for ESA's Athena project, so it needed to be calibrated as best as possible.

It is important to mention that the maximum displacement allowed by the stage's controller was 293 mm so the calibration was performed in steps multiple of 29 mm instead of 30 mm. 24 measurements were performed between the origin and the 29 mm and the obtained origin repeatability was 93 nm which is more than 5 times better than the origin repeatability indicated by the manufacturer ($\pm 0.5\,\mu\mathrm{m}$). For the calibration, after repeating each step 25 times at 10 $\mathrm{mm/s}$ the displacement error displayed in figure 8.11 was obtained.

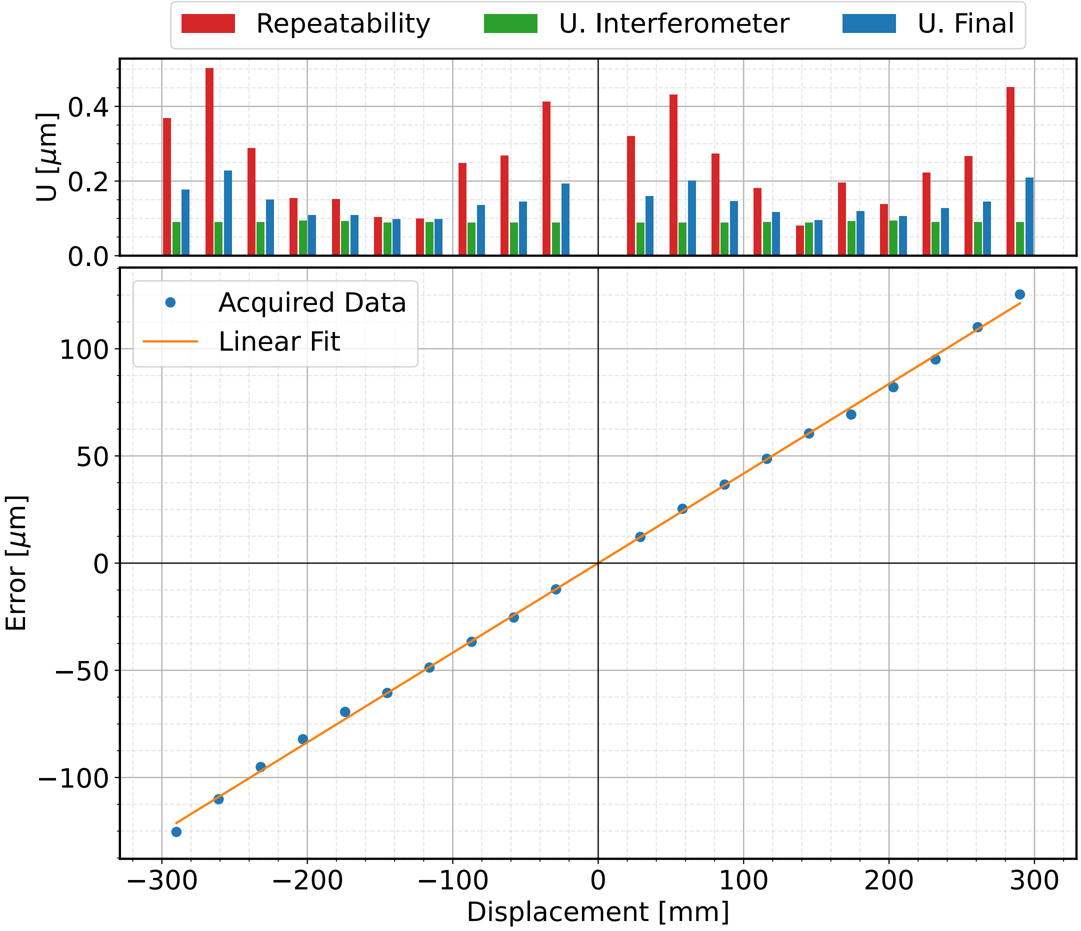

Figure 8.11: Displacement error of the M-IMS300PP stage.
The linear fit is: Error[μm]=d [mm] (0.418$\pm$0.003)

Although the error on the extreme positions is considerable for a stage of this quality, we can see that the displacement error is almost linear which suggests that the encoder value was not defined correctly. Multiplying it by the adjusting factor given by the slope, 1.000 418, gives us the corrected error displayed in figure 8.12, where the displacement error is reduced from 130 $\mu\mathrm{m}$ to 5 $\mu\mathrm{m}$.

As an example of another analysis the same measurements were repeated with a load of 10 kg, which gives us figure 8.13.

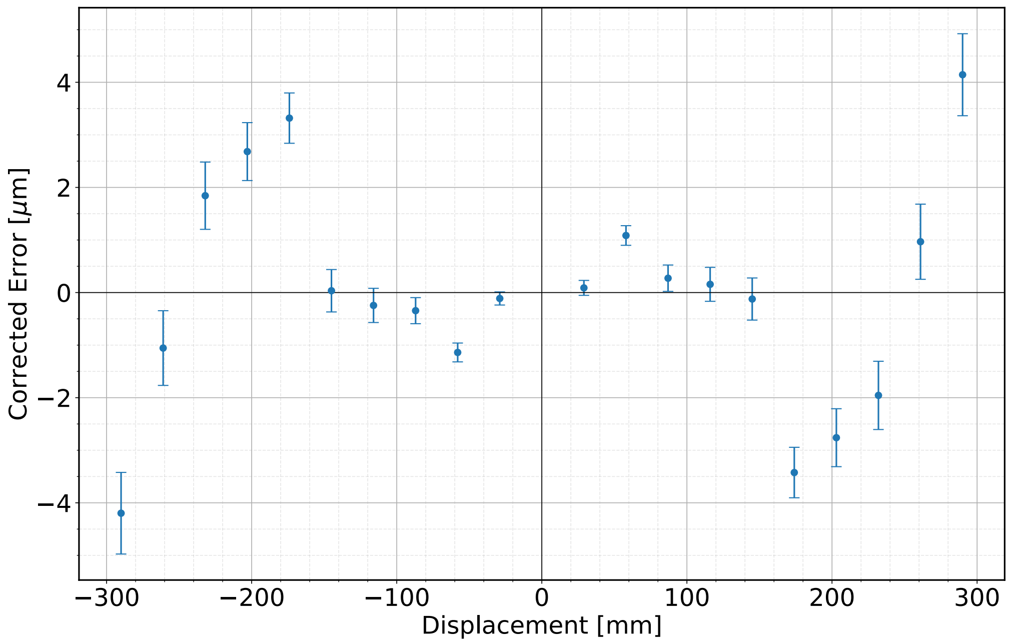

Figure 8.12: Displacement error of the M-IMS300PP stage after applying the corrections to the stage's encoder.

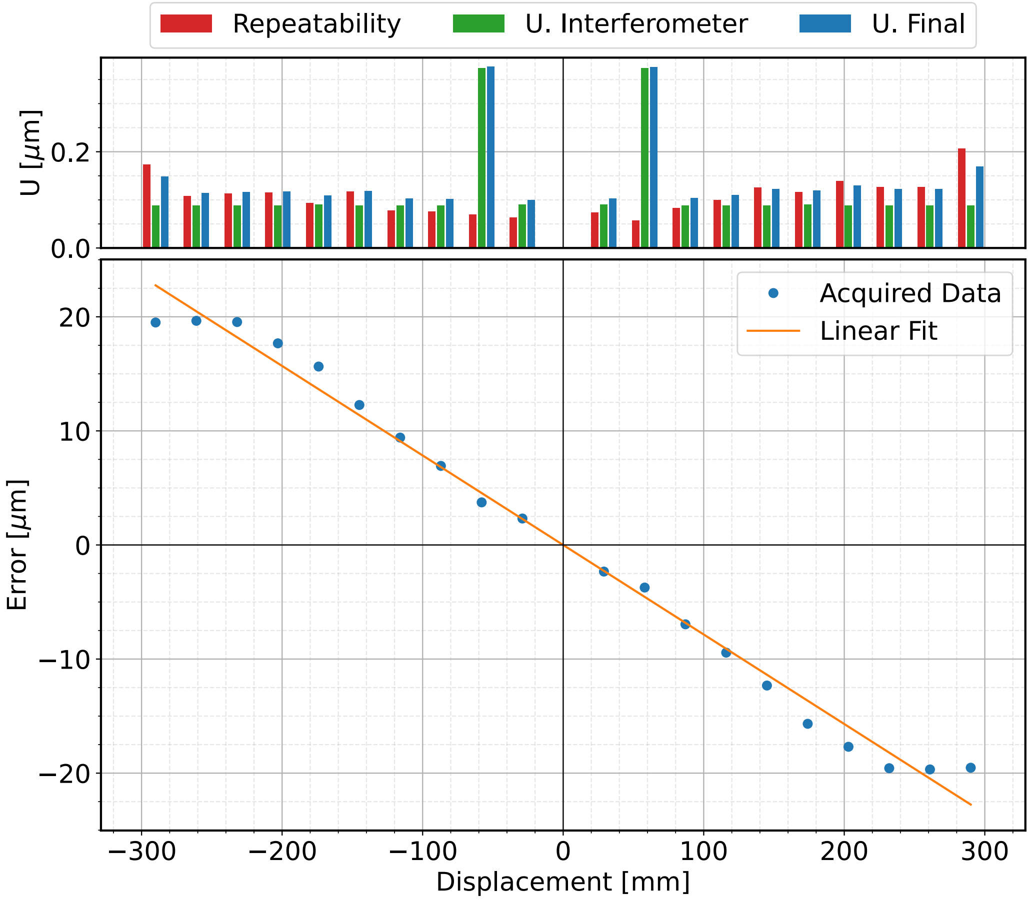

Figure 8.13: Displacement error of the M-IMS300PP stage with a load of 10kg. The linear fit is: Error[μm]=d [mm] (-0.078±0.002)

The reduction of the displacement error from +100 μm to -20 μm is quite significant, we can also see that the error was inverted becoming negative for positive displacements and symmetric in the other direction. Assuming the displacement error change with the load is linear this test suggests that the calibration performed by the manufacturer was done with a load of about 8 kg. Using the new linear fit we can correct the error and obtain figure 8.14, where we can see that the corrected error is an attenuation of figure 8.12.

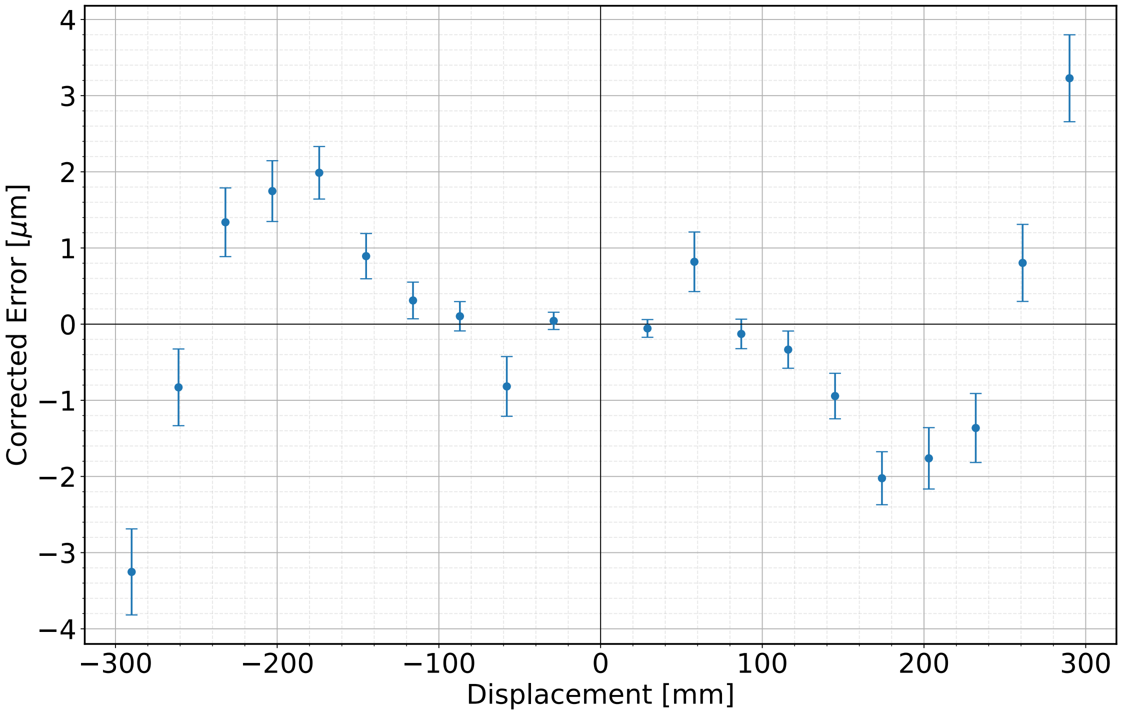

Figure 8.14: Displacement error of the M-IMS300PP stage with a load of 10 kg after applying the corrections to the stage's encoder.

Curiously, with one sixth of the maximum load, figure 8.13 is the symmetric of one sixth of figure 8.11. This suggests that with the maximum cargo figure 8.11 is inverted, so we can guarantee that the maximum error of this stage will never exceed the calibration, independently of the load applied. This test was very important because we saw that the manufacturer's specification depend on the load applied, so it is fundamental to test the stage with the final load it will have. These effects are only visible on stages with a good performance. All the calibration information is gathered in table 8.4.

Table 8.4: Comparison of the measured parameters of Newport's M-IMS300PP stage and the values specified by the manufacturer.

	Without Load	**With Load**	**Manufacturer**
Home Repeatability [nm]	93	-	500
Repeatability [nm]	503	207	1 250
Largest Error [nm]	125 400 ± 160	19 680 ± 120	-
Conversion Factor Correction	1.000 418	0.999 922	-
Largest Error with Correction [nm]	4 200 ± 780	3 250 ± 570	5 000

Analyzing the overall performance of the stage we can see that the home repeatability and the displacement's repeatability is better than the manufacturer indicated and after applying the corrections to the encoder the largest error can also be within the absolute accuracy indicated by the manufacturer. The increased measurement uncertainties observed in figure 8.11 and 8.13 were due to the length of this translation stage, at this distance from the interferometer the uncertainty of the refractive index starts to overcome the uncertainty of the number of fringes. The absurd measurement uncertainty of the $\pm 50\,\mu\mathrm{m}$ of figure 8.13 was due to an increase in the ambient pressure during the measurements, which was only detected after performing the calibration.

Finally, considering that the stage allowed velocities higher than all the other calibrated stages we decided to test not only the effects of the velocity on the displacement but also the limits of the measurement system. 10 measurements to the $150\,\mathrm{mm}$ were performed for 12 different velocities, the obtained results are represented in figure 8.15. In order for the unwrapping to be done correctly the sampling frequency was progressively increased from $50\,\mathrm{kHz}$ to $1.4\,\mathrm{MHz}$ because there always need to be at least 4 samples per fringe, as a precaution. Even at the higher frequencies the signal processing never raised any issues, all samples were acquired correctly.

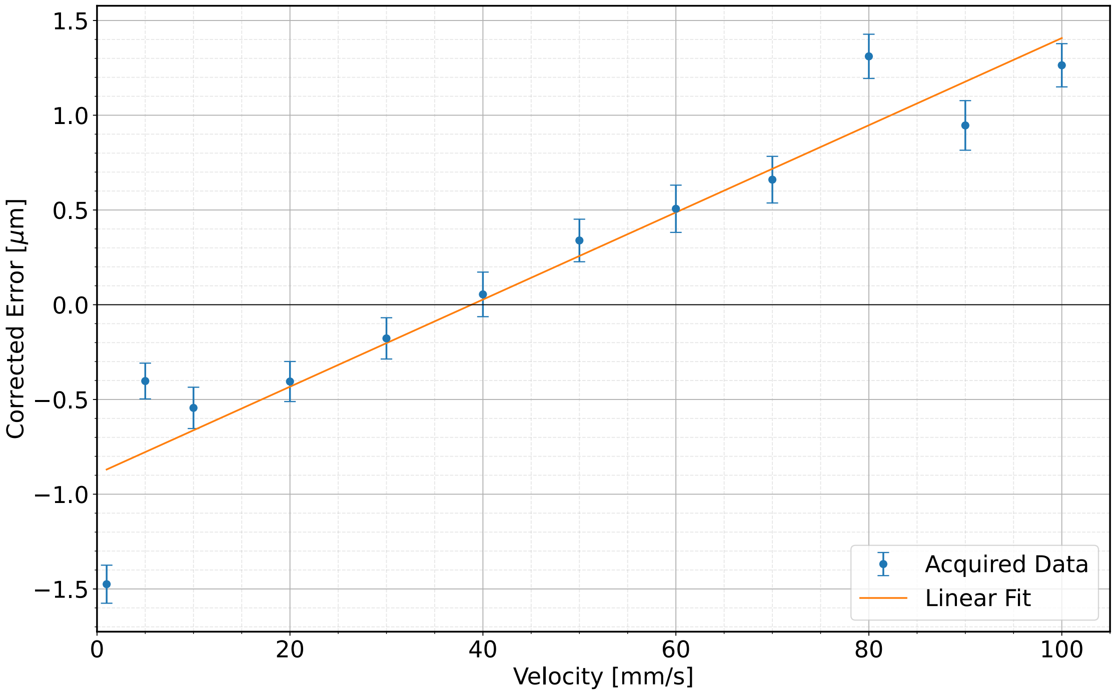

Figure 8.15: Displacement error of the M-IMS300PP stage with different velocities.

According to figure 8.15 the increase in velocity does change the displacement error. Although the error is varying around the expected value and is smaller than the stage's absolute accuracy determined in figure 8.12, it is still important to execute the calibration with the velocity the stage will use after the calibration. When the maximum performance possible of the stage is necessary, the calibration must be done under the desired load and velocity the stage will be subjected to.

The velocity measurements also unveiled new insight on the variation of the α parameter with the displacement's velocity, detailed in appendix D.

Chapter 9

Conclusions

An instrument capable of measuring displacements with a repeatability of a few nanometers was built, it reached an uncertainty level under 50 nanometers for displacements under 100 millimeters and 1 micrometer for displacements under 4 meters. The uncertainty budget led to an uncertainty estimate that can be approximated by the following linear fit:

$$U_d[\mathrm{m}] = (6.3\times10^{-9} + 2.7\times10^{-7}\times d)[\mathrm{m}] \tag{9.1}$$

This work went over main fundamental aspects in the development of an interferometer, from an analysis of the theoretical aspects to the calibration of four different translation stage models, resulting in a "turn-key" system ready to be used along with its user manual (not included in this thesis due to its size).

The following steps are the usage of the interferometer in projects that require high accuracy, its use is already planned for the characterization of translation stages for the ESA-Athena project (an XY translation of $400\,\mathrm{mm}$ range). The studies of the theory, uncertainty modeling, optical configurations, polarization and above all the experimental practices detailed in this work serve as key starting points for the development of other interferometers tailored to specific needs.

In terms of the developed work and personal experience it was extremely interesting to conjugate so many different areas in the same project. Starting from an intensive study of the theory behind interferometry that led us to several simulations, to the modeling and construction of mathematical models that allowed us to develop an uncertainty model, from where we extracted the requirements for each of the components. The engineering aspect of this work where we did the simulations, designed and built the interferometer proved to be an exceptional challenge and overcoming the difficulties that arose was very gratifying. Finally, creating and tuning the user interface was also a very satisfying part of this work because the intention in building this instrument is that any colleague from the laboratory can, by consulting the interferometer's user manual and this work, use the interferometer.

This measurement tool was fully described and characterized, evaluating the main parameters that contributed with significant relevance to the uncertainty budget. The system can be considered ready for integration in new projects, in particular, in the characterization and estimation of the measurement errors of other tools, with high accuracy and measurement stability. This system is particularly useful in applications where the knowledge of the performance of the tools used to displace and align optical components is fundamental.

References

[1] Joint Comitee for Guides in Metrology, “Guide to the expression of Uncertainty in Measurement pack”, 1ed., 2008. Consulted on the 26th February 2021, available at: https://www.bipm.org/en/publications/guides/gum.html.

[2] A. J. Fleming, “A review of nanometer resolution position sensors: Operation and performance”, *Sensors and Actuators A: Physical*, vol. 190, pp. 106–126, 2013.

[3] Thorlabs, Inc. Consulted on the 16th February 2021, available at: https://www.thorlabs.com/.

[4] Physik Instrumente, Inc. Consulted on the 16th February 2021, available at: https://www.physikinstrumente.com/en/.

[5] A. A. Michelson, *Studies in Optics*, ch. 13. Dover Publications, 1 ed., 1995.

[6] BIPM, “SI Base Units”, consulted on the 13th March 2021, available at: https://www.bipm.org/en/si-base-units/metre.

[7] E. O. Göbel and U. Siegner, *The New International System of Units (SI)*, ch. 2. Weinheim, Germany: John Wiley & Sons, Ltd, 2019.

[8] M. A. Martin-Delgado, “The new SI and the fundamental constants of nature”, *European Journal of Physics*, vol. 41, p. 063003, oct 2020.

[9] P. Hariharan, *Basics of Interferometry*, ch. 2. Academic Press, 2 ed., 2007.

[10] P. Hariharan, *Optical Interferometry*, ch. 1. Academic Press, 2 ed., 2003.

[11] E. Collett, *Field Guide to Polarization*. Bellingham, Washington: SPIE Press, 2005.

[12] D. G. Smith, *Field Guide to Physical Optics*. Bellingham, Washington: SPIE Press, 2013.

[13] C. Akcay, P. Parrein, and J. P. Rolland, “Estimation of longitudinal resolution in optical coherence imaging”, *Appl. Opt.*, vol. 41, pp. 5256–5262, Sep 2002.

[14] J. Watchi, S. Cooper, B. Ding, C. M. Mow-Lowry, and C. Collette, “A review of compact interferometers”, 2018.

[15] M. Pisani, A. Yacoot, P. Balling, N. Bancone, C. Birlikseven, M. Çelik, J. Flügge, R. Hamid, P. Köchert, P. Kren, U. Kuetgens, A. Lassila, G. B. Picotto, E. Şahin, J. Seppä, M. Tedaldi, and C. Weichert, “Comparison of the performance of the next generation of optical interferometers”, *Metrologia*, vol. 49, pp. 455–467, may 2012.

[16] M. Bass, C. DeCusatis, J. Enoch, V. Lakshminarayanan, G. Li, C. Macdonald, V. Mahajan, and E. Van Stryland, *Handbook of Optics, Third Edition Volume I: Geometrical and Physical Optics, Polarized Light, Components and Instruments*, ch. 32. USA: McGraw-Hill, Inc., 3 ed., 2009.

[17] European Accreditation Laboratory Comitee, "EA-4/02 M:2021 Evaluation of the Uncertainty of Measurement in calibration", 2021. Consulted on the 20th November 2021, available at: https://european-accreditation.org/publications/ea-4-02-m/.

[18] N. Bobroff, "Recent advances in displacement measuring interferometry", *Measurement Science and Technology*, vol. 4, p. 907, 01 1999.

[19] J. H. Zimmerman and J. A. Stone, "Index of refraction of air", consulted on the 17th February 2021, available at: https://emtoolbox.nist.gov/Wavelength/Documentation.asp#IndexofRefractionofAir.

[20] J. D. Ellis, *Field Guide to Displacement Measuring Interferometry*. Bellingham, Washington: SPIE Press, 2014.

[21] H. Bai, M. Shan, Z. Zhong, L. Guo, and Y. Zhang, "Parallel-quadrature on-axis phase-shifting common-path interferometer using a polarizing beam splitter", *Appl. Opt.*, vol. 54, pp. 9513–9517, Nov 2015.

[22] University of Minnesota, "Quadrature Michelson Interferometer", consulted on the 7th April 2021, available at: https://sites.google.com/a/umn.edu/mxp/advanced-labs/quadrature-michelson-interferometer.

[23] P. Gregorčič, T. Požar, and J. Mozina, "Quadrature phase-shift error analysis using a homodyne laser interferometer", *Optics express*, vol. 17, pp. 16322–31, 09 2009.

[24] P. L. M. Heydemann, "Determination and correction of quadrature fringe measurement errors in interferometers", *Appl. Opt.*, vol. 20, pp. 3382–3384, Oct 1981.

[25] C. Wu, C. Su, and G. Peng, "Correction of nonlinearity in one-frequency optical interferometry", *Measurement Science and Technology*, vol. 7, pp. 520–524, apr 1996.

[26] I. Leite and A. Cabral, "An optical metrology system for the measurement of the refractive index of glass", 2020.

[27] G. Roque and A. Cabral, "Development of a metrology method for the alignment of optical systems", 2022.

[28] W. H. Steel, "Polarization-preserving retroreflectors", *Appl. Opt.*, vol. 24, pp. 3433–3434, Nov 1985.

[29] J. Liu and R. M. A. Azzam, "Polarization properties of corner-cube retroreflectors: theory and experiment", *Appl. Opt.*, vol. 36, pp. 1553–1559, Mar 1997.

[30] W. He, F. Yuegang, Y. Zheng, L. Zhang, J. Wang, Z. Liu, and J. Zheng, "Polarization properties of a corner-cube retroreflector with three-dimensional polarization ray-tracing calculus", *Applied optics*, vol. 52, pp. 4527–4535, 07 2013.

Appendix A

Jones Computation of Irradiances

The evaluation of each optical configuration is done in the following three steps:

First there is the need to define the Jones equations for each arm of the interferometer, which yields two different electric fields, one corresponding to the reference arm ($\vec{\mathrm{E}}_{\mathrm{ref}}$) and another corresponding to the measurement arm ($\vec{\mathrm{E}}_{\mathrm{meas}}$). Note that these equations only describe the electric fields before the detection module.

Secondly, according to the superposition principle the total electric field before the detection module is given by:

$$\vec{\mathrm{E}}_{\mathrm{net}} = \vec{\mathrm{E}}_{\mathrm{ref}} + \vec{\mathrm{E}}_{\mathrm{meas}} \tag{A.1}$$

Finally, the irradiance is given by equation 2.20.

A.1 Quadrature with two polarizing beamsplitters

For the configuration represented in figure 4.1, the two electric fields are:

$$\vec{\mathrm{E}}_{\mathrm{ref}} = \mathbf{J}_{\mathrm{WP}} \left(45°; \frac{\pi}{2}\right) \mathbf{J}_{\mathrm{POL}}(22.5°)\mathbf{J}_{\mathrm{PBS}_y}\mathbf{J}_{\mathrm{PBS}_y}\vec{\mathrm{E}}_0 \tag{A.2}$$

$$\vec{\mathrm{E}}_{\mathrm{meas}} = \mathbf{J}_{\mathrm{WP}} \left(45°; \frac{\pi}{2}\right) \mathbf{J}_{\mathrm{POL}}(22.5°)\mathbf{J}_{\mathrm{PBS}_x}\mathbf{J}_{\mathrm{OPD}}\mathbf{J}_{\mathrm{PBS}_x}\vec{\mathrm{E}}_0 \tag{A.3}$$

After computing the sum of the last two equations, the net electric field is approximately given by:

$$\vec{\mathrm{E}}_{\mathrm{net}} \approx 0.19 \begin{bmatrix} e^{i\frac{7\pi}{8}} + e^{i(\delta - \frac{3\pi}{8})} \\ e^{-i\frac{3\pi}{8}} + e^{i(\delta + \frac{7\pi}{8})} \end{bmatrix} \tag{A.4}$$

Finally, using equation 2.20, we have:

$$I \approx 0.072 \begin{bmatrix} 1 + \sin\left(\delta + \frac{\pi}{4}\right) \\ 1 + \sin\left(\delta + \frac{3\pi}{4}\right) \end{bmatrix} \tag{A.5}$$

A.2 Quadrature with a non-polarizing beamsplitter

For the configuration represented in figure 4.2, the two electric fields are:

$$\vec{\mathrm{E}}_{\mathrm{ref}} = \mathbf{J}_{\mathrm{BS}}\mathbf{J}_{\mathrm{POL}}(45°)\mathbf{J}_{\mathrm{POL}}(45°)\mathbf{J}_{\mathrm{BS}}\mathbf{J}_{\mathrm{WP}} \left(45°; \frac{\pi}{2}\right) \vec{\mathrm{E}}_0 \tag{A.6}$$

$$\vec{\mathrm{E}}_{\mathrm{meas}} = \mathbf{J}_{\mathrm{BS}}\mathbf{J}_{\mathrm{OPD}}\mathbf{J}_{\mathrm{BS}}\mathbf{J}_{\mathrm{WP}}\left(45^\circ; \frac{\pi}{2}\right)\vec{\mathrm{E}}_0 \tag{A.7}$$

After computing the sum of the last two equations, the net electric field is given by:

$$\vec{\mathrm{E}}_{\mathrm{net}} = \frac{1}{2\sqrt{2}}\begin{bmatrix} \frac{1}{\sqrt{2}}e^{i\frac{3\pi}{4}} + e^{i(\delta+\frac{\pi}{2})} \\ \frac{1}{\sqrt{2}}e^{-i\frac{\pi}{4}} + e^{i\delta} \end{bmatrix} \tag{A.8}$$

Finally, using equation 2.20 the irradiance is approximately:

$$I \approx 0.19\begin{bmatrix} 1 + 0.94\sin\left(\delta + \frac{\pi}{4}\right) \\ 1 + 0.94\sin\left(\delta - \frac{\pi}{4}\right) \end{bmatrix} \tag{A.9}$$

A.3 Quadrature with two quarter waveplates

For the configuration represented in figure 4.3, the two electric fields are:

$$\vec{\mathrm{E}}_{\mathrm{ref}} = \mathbf{J}_{\mathrm{WP}}\left(45^\circ; \frac{\pi}{2}\right)\mathbf{J}_{\mathrm{BS}}\mathbf{J}_{\mathrm{WP}}\left(22.5^\circ; \frac{\pi}{2}\right)\mathbf{J}_{\mathrm{WP}}\left(22.5^\circ; \frac{\pi}{2}\right)\mathbf{J}_{\mathrm{BS}}\vec{\mathrm{E}}_0 \tag{A.10}$$

$$\vec{\mathrm{E}}_{\mathrm{meas}} = \mathbf{J}_{\mathrm{WP}}\left(45^\circ; \frac{\pi}{2}\right)\mathbf{J}_{\mathrm{BS}}\mathbf{J}_{\mathrm{OPD}}\mathbf{J}_{\mathrm{BS}}\vec{\mathrm{E}}_0 \tag{A.11}$$

After computing the sum of the last two equations, the net electric field is given by:

$$\vec{\mathrm{E}}_{\mathrm{net}} = \frac{1}{2\sqrt{2}}\begin{bmatrix} e^{i\frac{\pi}{4}} + e^{i(\delta+\frac{\pi}{2})} \\ e^{-i\frac{3\pi}{4}} + e^{i\delta} \end{bmatrix} \tag{A.12}$$

Using equation 2.20 the irradiance is:

$$I = 0.25\begin{bmatrix} 1 + \sin\left(\delta + \frac{\pi}{4}\right) \\ 1 + \sin\left(\delta + \frac{3\pi}{4}\right) \end{bmatrix} \tag{A.13}$$

A.4 Quadrature with an octadic waveplate

For the configuration represented in figure 4.4, the two electric fields are:

$$\vec{\mathrm{E}}_{\mathrm{ref}} = \mathbf{J}_{\mathrm{BS}}\mathbf{J}_{\mathrm{WP}}\left(0^\circ; \frac{\pi}{4}\right)\mathbf{J}_{\mathrm{WP}}\left(0^\circ; \frac{\pi}{4}\right)\mathbf{J}_{\mathrm{BS}}\vec{\mathrm{E}}_0 \tag{A.14}$$

$$\vec{\mathrm{E}}_{\mathrm{meas}} = \mathbf{J}_{\mathrm{BS}}\mathbf{J}_{\mathrm{OPD}}\mathbf{J}_{\mathrm{BS}}\vec{\mathrm{E}}_0 \tag{A.15}$$

After computing the sum of the last two equations, the net electric field is given by:

$$\vec{\mathrm{E}}_{\mathrm{net}} = \frac{1}{2\sqrt{2}}\begin{bmatrix} e^{i\frac{\pi}{4}} + e^{i\delta} \\ e^{-i\frac{\pi}{4}} + e^{i\delta} \end{bmatrix} \tag{A.16}$$

Using equation 2.20 the irradiance is:

$$I = 0.25\begin{bmatrix} 1 + \sin\left(\delta + \frac{\pi}{4}\right) \\ 1 + \sin\left(\delta + \frac{3\pi}{4}\right) \end{bmatrix} \tag{A.17}$$

Appendix B

Interference Pattern

An interference pattern is composed by a large number of fringes. Although equation 2.19 expresses the irradiance at the center of the interference pattern, the detected signal is not equal to this equation because the detector will not detect only the center of the pattern. In our case the detector window was a 3.6 mm sided square, but we will assume for simplicity that it was a circle of radius 1.8 mm.

The output of the detector is proportional to the average of the detected irradiance, which is never equal to equation 2.19, in fact, as the number of fringes detected increases, the impact of the interference term is more and more attenuated, to the point of no interference being detected. With some geometric approximations it is possible to calculate if there is more than one fringe inside the detector window, allowing us to estimate the total irradiance on the detector and determine the modulation of the signal.

B.1 Spherical Wavefronts with Different Radii

Since a laser emits spherical waves and there is a difference in the optical paths of the interfering waves, the radius of curvature of the two wavefronts differs. This phenomenon is important because when the distance between the two wavefronts becomes bigger than one wavelength another fringe appears, as is exemplified in figure B.1.

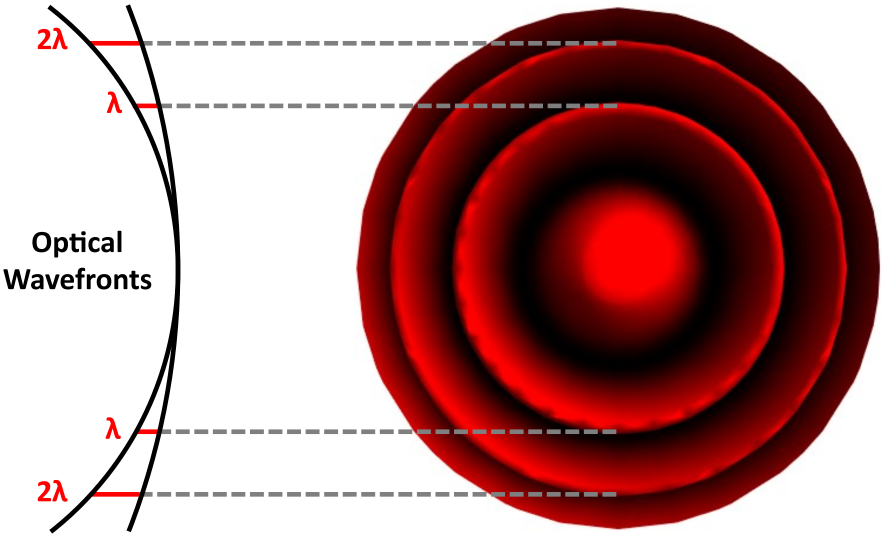

Figure B.1: Interference pattern schematic explaining the appearance of more than one fringe.

A new term corresponding to the distance between wavefronts appears in the phase difference between the two waves. We can rewrite equation 2.19 as:

$$I = I_1 + I_2 + 2\sqrt{I_1 I_2}\cos(\Delta\varphi_{\mathrm{OPD}} + \Delta\varphi_{\mathrm{WF}}) \tag{B.1}$$

Where $\Delta\varphi_{\mathrm{OPD}}$ corresponds to the phase difference introduced by the optical path difference in the interferometer arms and $\Delta\varphi_{\mathrm{WF}}$ corresponds to the phase difference introduced by the distance between wavefronts, which is related to the distance between wavefronts (d'_{WF}) by:

$$d'_{\mathrm{WF}} = \frac{\Delta\varphi_{\mathrm{WF}}}{2\pi}\frac{\lambda}{n} \tag{B.2}$$

The distance between the two wavefronts can be expressed as a function of the distance to the optical axis (d'_{OA}) and of the two different radii (R'_1 and R'_2), according to the notation in figure B.2, as:

$$d'_{\mathrm{WF}} = R'_1 - R'_2 + \sqrt{R'^2_2 + d'^2_{\mathrm{OA}}} - \sqrt{R'^2_1 - d'^2_{\mathrm{OA}}} \tag{B.3}$$

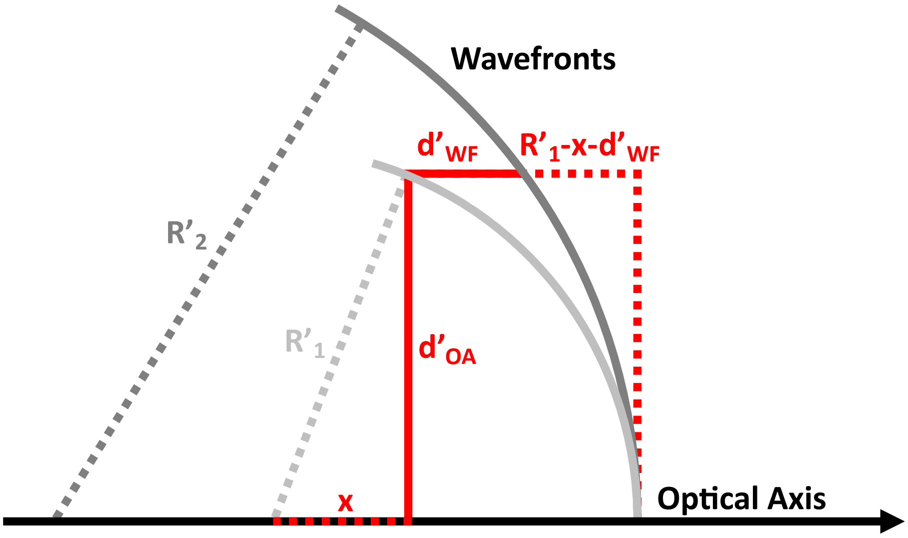

Figure B.2: Schematic for the calculation of the distance between two spherical waves.

B.2 Calculation of the Radius of Curvature of the Wavefronts

To estimate the size of the two different radii the center of curvature of the laser beam waves must be determined. By knowing the laser beam divergence ($\theta = 1.8\,\mathrm{mrad}$) and the beam radius ($d'_{\mathrm{OA}_0} = 0.25\,\mathrm{mm}$) it is possible to calculate the center of curvature, according to figure B.3 the distance from the center of curvature of the waves to the opening of the laser cavity (d'_{LC}) is:

$$d'_{\mathrm{LC}} = \frac{d'_{\mathrm{OA}_0}}{\tan\theta} \approx 0.14\,\mathrm{m} \tag{B.4}$$

Any distance beyond the laser, summed by d'_{LC}, equals the radius of curvature of the wavefront. Since the beam expander increases the curvature radius four times, with the distances in figure B.4 we have:

$$R'_{ref} \approx 2.67\,\mathrm{m} \qquad R'_{meas} \approx 2.78\,\mathrm{m} + 2d'_{\mathrm{OPD}} \tag{B.5, B.6}$$

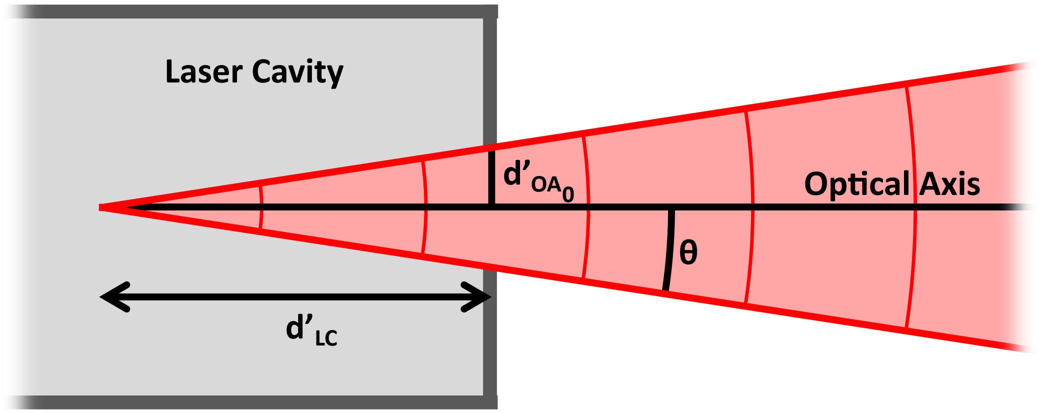

Figure B.3: Schematic of spherical wavefronts produced by a laser.

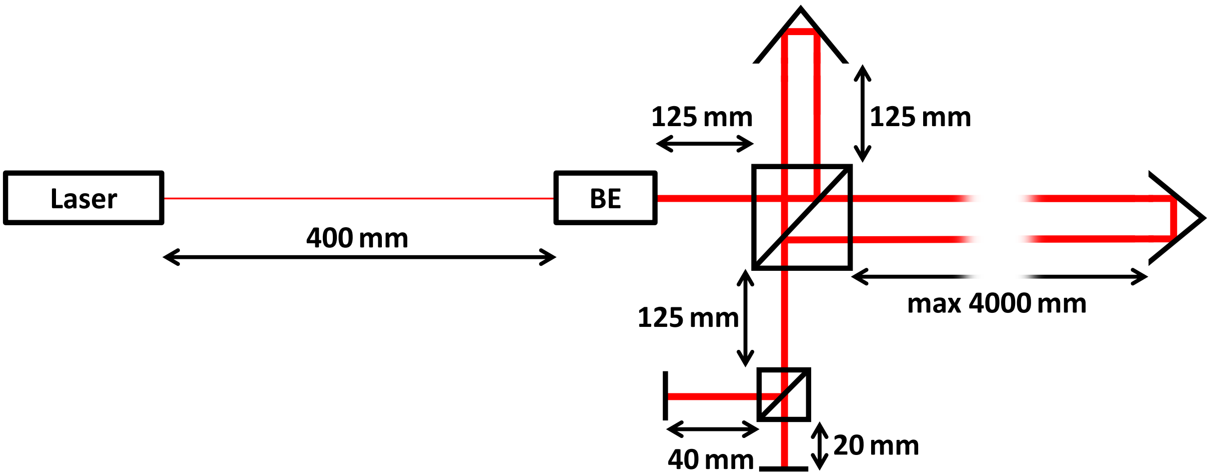

Figure B.4: Optical path distances in the chosen configuration.

B.3 Mathematical Model for the Interference Pattern

To simplify the model in equation B.1 we can normalize the irradiance by assuming $I_1 = I_2 = 0.25$. Finally, the Gaussian profile is attained by multiplying the model by an adequate Gaussian function:

$$I = [0.5 + 0.5\cos(\Delta\varphi_{\mathrm{WF}} + \Delta\varphi_{\mathrm{OPD}})]e^{-\frac{d'^2_{\mathrm{OA}}}{2\pi\lambda}} \tag{B.7}$$

Using equations B.7, B.6, B.5 and B.3 the interference pattern for any optical path difference can be calculated. To test the developed model, an interferometer was built according to figure B.4 and at three different optical path differences (20 cm, 1 m and 4 m) the observed interference pattern was in agreement with the simulation.

B.4 Signal Modulation Evaluation

By simulating the detected irradiance for an optical path difference of 4 m with different detection radii, figure B.5 shows that the irradiance is attenuated with the increase of detection radius.

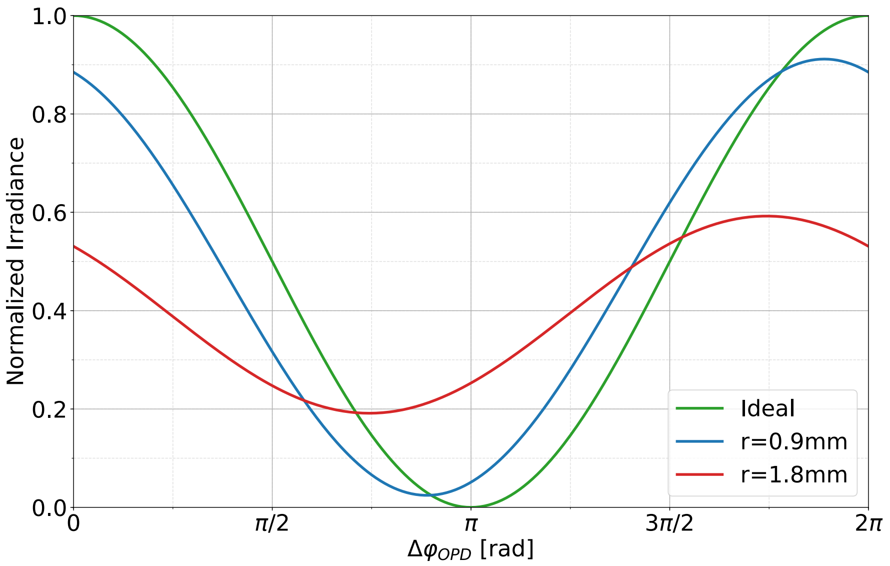

Figure B.5: Simulation of the detected irradiance as the detection radius increases, for an optical path difference of $4\,\mathrm{m}$.

Since the ideal signal is normalized the modulation of the detected signals is defined as simply the amplitude of the signal. In figure B.5 with a diaphragm of radius $0.9\,\mathrm{mm}$ the modulation is $88.7\,\%$ while without a diaphragm the modulation is $40.1\,\%$. This reveals that with an optical path difference of $4\,\mathrm{m}$ it is better to use a diaphragm to reduce the number of fringes detected.

Repeating this process for multiple distances and for various diaphragm radii offers a better understanding of how the modulation of the signal varies with the diaphragm radius.

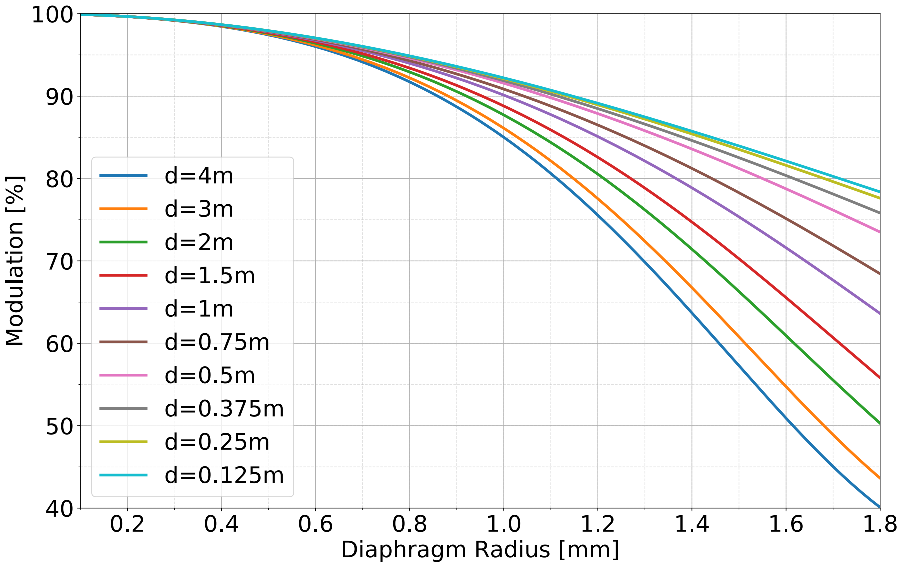

Figure B.6: Simulation of the detected irradiance modulation for different diaphragm radii and for multiple sizes of the measurement arm.

As expected, figure B.6 reveals that for longer optical path differences the modulation tends to be worse, which suggests the use of a diaphragm. Although for smaller distances the change is negligible. We can also conclude that the ideal length for the measurement arm is $0.125\,\mathrm{mm}$, when the optical path difference is null, because both wavefronts have the same radius of curvature.

Appendix C

Component Polarization Studies

While assembling the interferometer some polarization changes that did not agree with the theoretical model were observed after the beamsplitter. This suggested that either the beamsplitter or the retroreflectors were altering the polarization of the incident radiation. To better comprehend this phenomenon two different studies were done to understand how the beamsplitter and the retroreflectors altered the polarization of incident radiation and how to minimize this effect to guarantee quadrature.

C.1 Retroreflectors

The changes in polarization caused by retroreflectors have been a subject of interest since 1985 [28, 29, 30]. Depending on the incident sextant of the retroreflector, or even on the coating, the reflected light's polarization can be changed. With the goal of maintaining the polarization of the incident radiation every retroreflector available was characterized.

To test every retroreflector's behaviour to the relevant polarizations (45° and RCP) a configuration that directly measures the polarization of the radiation reflected by the retroreflector, figure C.1, was assembled.

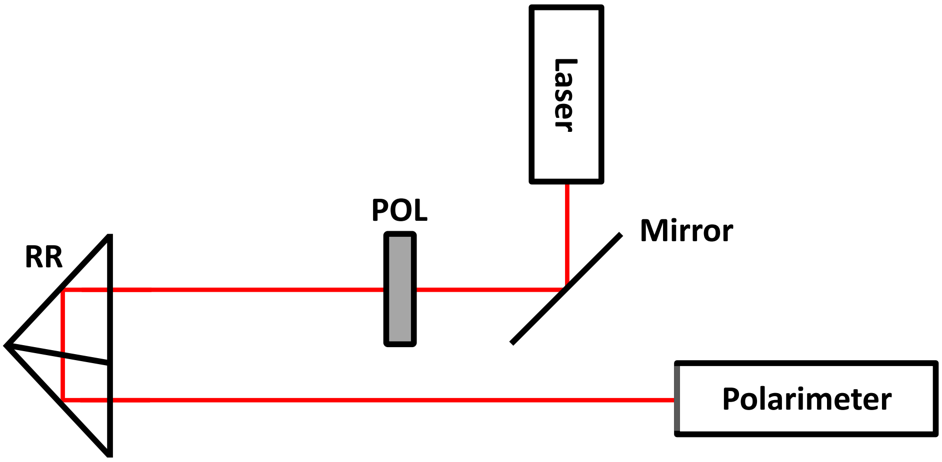

Figure C.1: Schematic of the configuration used to measure the polarization changes in the retroreflectors. The polarizer was replaced by a quarter waveplate to create circular polarization.

By rotating the retroreflector every sextant was tested, the conclusions are presented in figures C.2 and C.3.

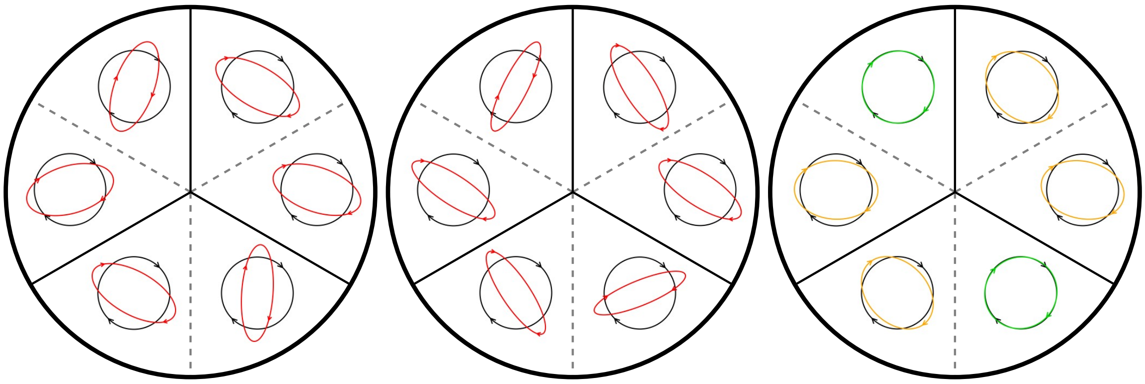

(a) First Retroreflector. (b) Second Retroreflector. (c) Third Retroreflector.

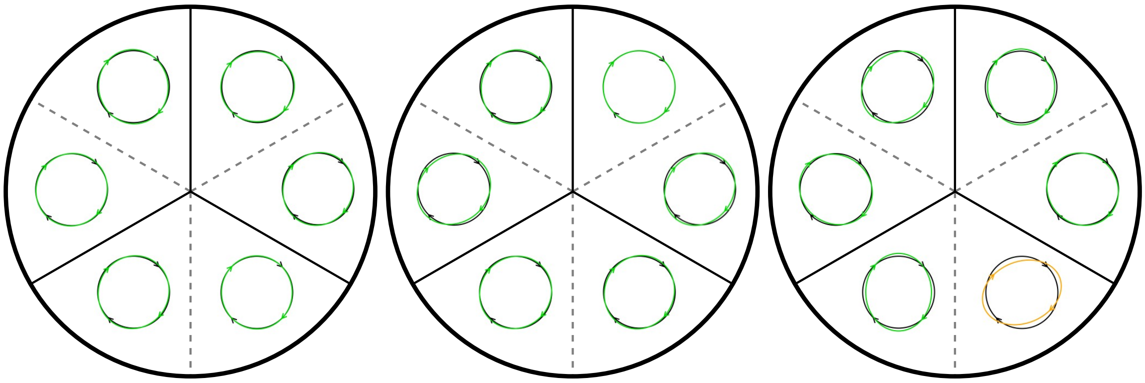

(d) Fourth Retroreflector. (e) Fifth Retroreflector. (f) Sixth Retroreflector.

Figure C.2: Reflected polarization of each retroreflector's sextant when the incident radiation is right handed circularly polarized. In black we have the incident radiation and the colored plot represents the reflected polarization in each sextant.

Although the fifth and the sixth retroreflectors proved to be good choices for both polarizations, they could not be used because the mirrors were not properly fixed to the retroreflector frame and as a consequence oscillated, this would introduce errors in the measurement since the movement of the translation stage would perturb the mirrors. Only the first four retroreflectors are viable candidates.

As we can see in figure C.2, the first, second and third retroreflectors alter circular polarization considerably, independently of the incident sextant, so the only possible choice for the measurement arm is the fourth retroreflector.

For the measurement arm it was not essential that the polarization was maintained because the radiation passed through the polarizer after being reflected, although if the polarization is changed by the retroreflector then unnecessary losses of irradiance would happen at the polarizer. Excluding the retroreflector necessary for the measurement arm and the last two cases, figure C.3 shows that the best option was the second retroreflector. For the placement of this retroreflector it was necessary to have particular attention to the incident sextant, because as we can see in figure C.3b not all sextants maintain the 45° polarization.

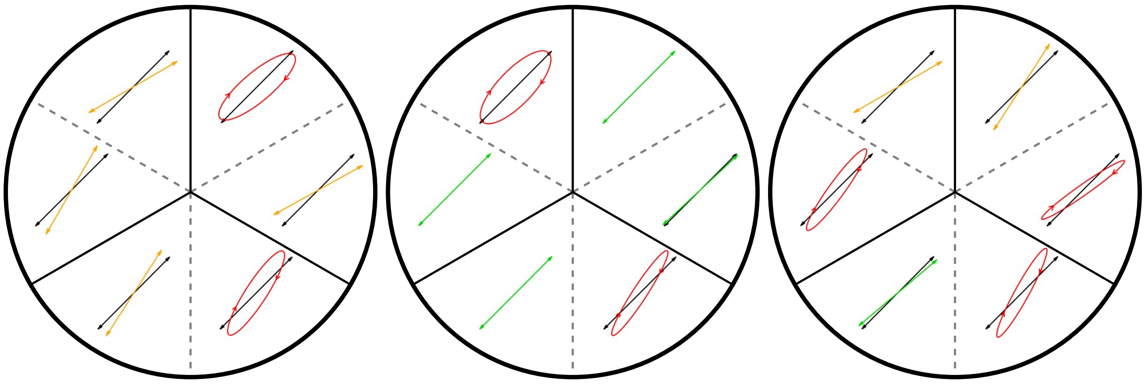

(a) First Retroreflector. (b) Second Retroreflector. (c) Third Retroreflector.

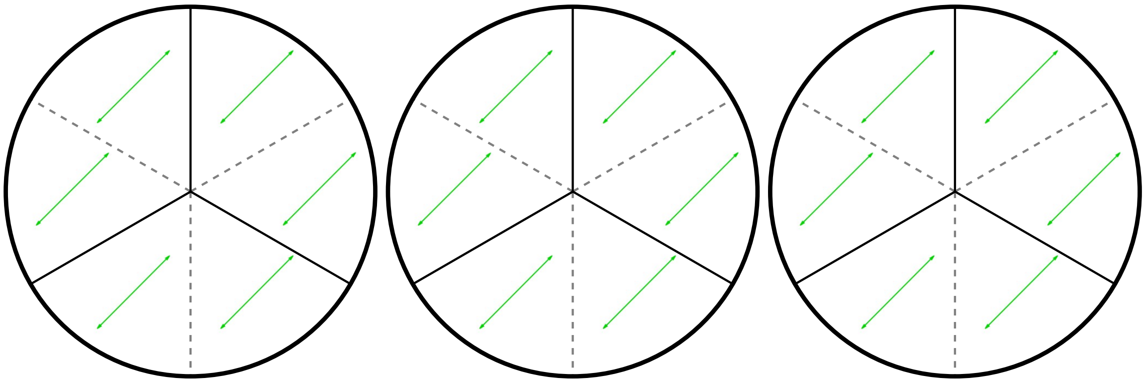

(d) Fourth Retroreflector. (e) Fifth Retroreflector. (f) Sixth Retroreflector.

Figure C.3: Reflected polarization of each retroreflector when the incident radiation is polarized at 45°. In black we have the incident radiation and the colored plot represents the reflected polarization in each sextant.

C.2 Beamsplitter

Beamsplitters have a preferential side for incident radiation, usually marked with a dot. Since both sides of the beamsplitter were used to transmit and reflect radiation it was important not only to characterize the dotted side of the beamsplitter, but also the non-dotted side. For the characterization of transmissions and reflections through both sides of the beamsplitter a simple setup was assembled according to figure C.4.

After measuring the changes of transmitted and reflected right handed circular polarization (figure C.5) we concluded that maintaining circular polarization after two passes through the beamsplitter was impossible because after the first pass the polarization was no longer circular. The focus of the beamsplitter positioning was on maintaining the 45° polarization.

For the 45° polarization it was only important that the last reflection on the beamsplitter maintained the polarization. Figure C.6 indicates that a reflection in the dotted face of the beamsplitter alters the polarization more than a reflection on the non-dotted face, so the beamsplitter needed to be placed in a way that the last reflection happened on the non-dotted face.

For quadrature to happen it was essential that the phase difference between both polarizations of the radiation in the measurement arm was as close to 90° as possible. This does not imply the polarization needed to be circular, which we have already concluded cannot happen. If the amplitudes of both polarizations are not equal, a 90° offset will represent a vertical ellipse. By rotating the quarter waveplate it was possible, with the nonlinear effects of the beamsplitter, to achieve the 90° offset.

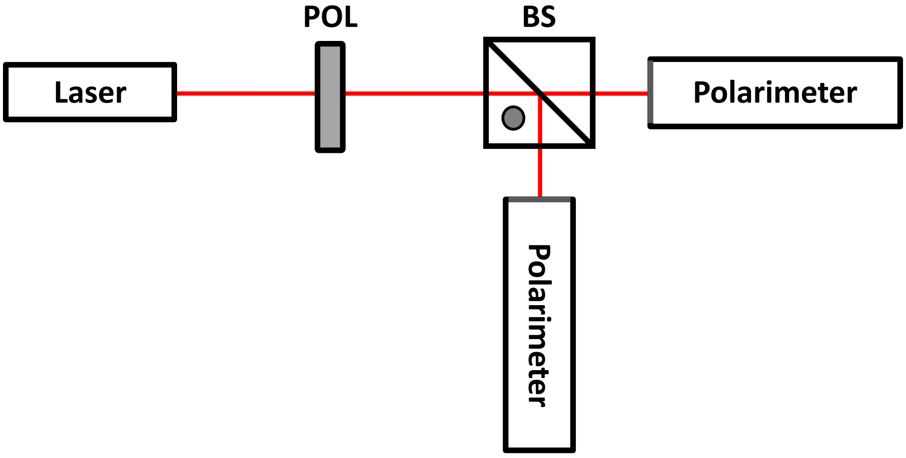

Figure C.4: Schematic of the configuration used to measure the polarization changes in the beamsplitter. The polarizer was replaced by a quarter waveplate to create circular polarization and the beamsplitter was rotated 180° to test the non-dotted face.

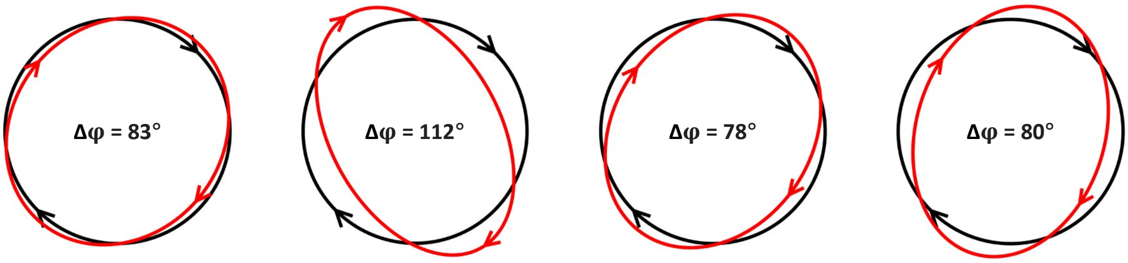

(a) Transmission through the dotted face.

(b) Reflection through the dotted face.

(c) Transmission through the non-dotted face.

(d) Reflection through the non-dotted face.

Figure C.5: Lissajous figure of the reflections and transmissions of the beamsplitter when the incident radiation is right handed circularly polarized. In black we have the incident polarization and in red the corresponding transmitted/reflected polarization.

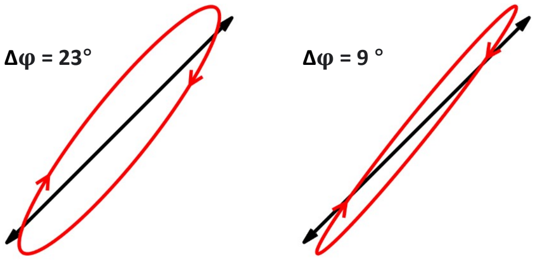

(a) Reflection through the dotted face.

(b) Reflection through the non-dotted face.

Figure C.6: Lissajous figure of the reflections and transmissions of the beamsplitter, when the incident radiation has a phase difference of 45°. In black we have the incident polarization and in red the reflected polarization.

Appendix D

Phase Difference Variation with Velocity

During the development and improvement of the LabVIEW interface we noticed that the phase difference was being altered during the movement of the translation stages, which translates into a variation of the α parameter of the elliptical fit. In order to diagnose this variation of the α parameter we started by testing all the available translation stages. With this we noticed that the variation of α was positive in one direction (when the movement was away from the interferometer) and negative in the other. We also realized that this problem was not related with the alignment of the translation stages, or the stages themselves, because the effect was equal for any of the three used stages.

To characterize the variation of α with the stage's speed we decided to register the mean value of α during the movement for 40 different velocities, because the value of α did not change significantly once the movement is uniform. For this purpose, two different translation stages were used, one with a maximum displacement of $25\,\mathrm{mm}$ for velocities under $1\,\mathrm{mm/s}$ and another with a maximum displacement of $200\,\mathrm{mm}$ for velocities over $1\,\mathrm{mm/s}$, the results are presented in figures D.1 and D.2 and the respective linear fits are repeated below:

$$\alpha = (1.322 \pm 0.006)v - 0.42 \pm 0.04 \tag{D.1}$$

$$\alpha = (1.34 \pm 0.04)v - 0.29 \pm 0.03 \tag{D.2}$$

We can see that for the smaller displacement the linear fit is worse, this is due to α being the average of less samples than for the longer displacement. However, when considering the uncertainty of both slopes we can conclude that the slopes intersect which confirms that the problem was not related to the stages in use since the fits overlap for different stages. Note that the different intersections of the y axis represent the two different alignment errors of each stage

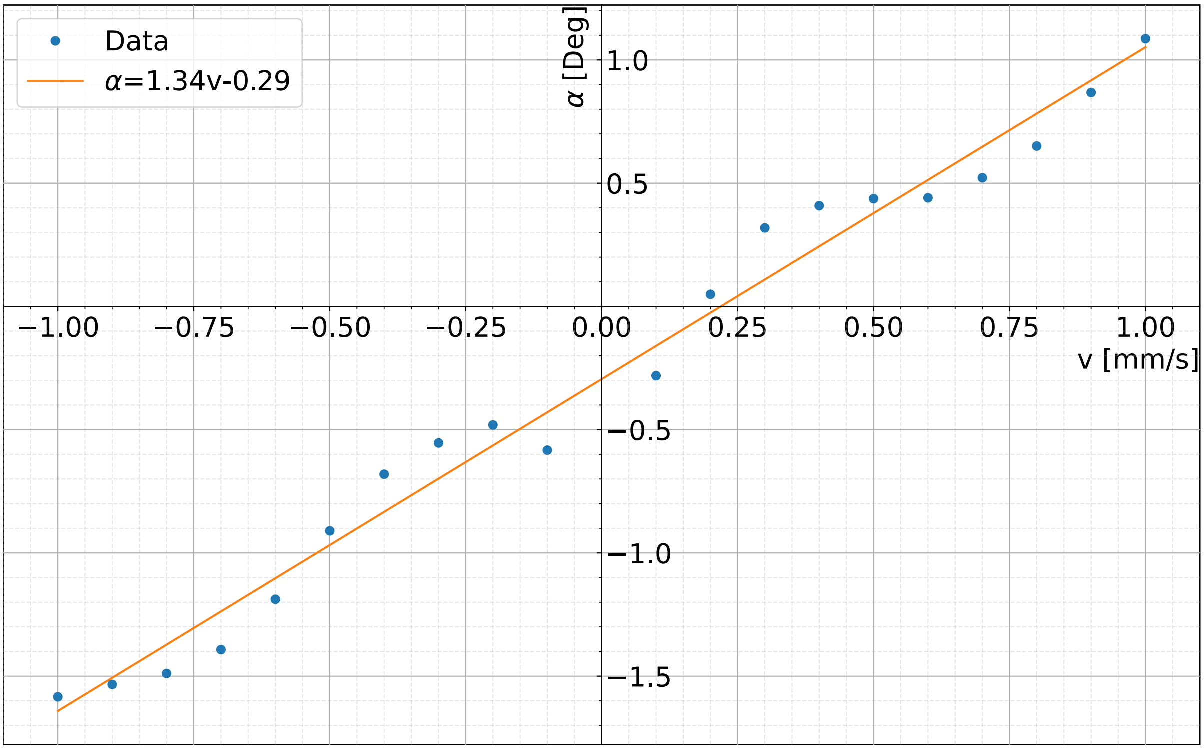

Figure D.1: Phase difference variation for speeds under 1 mm/s.

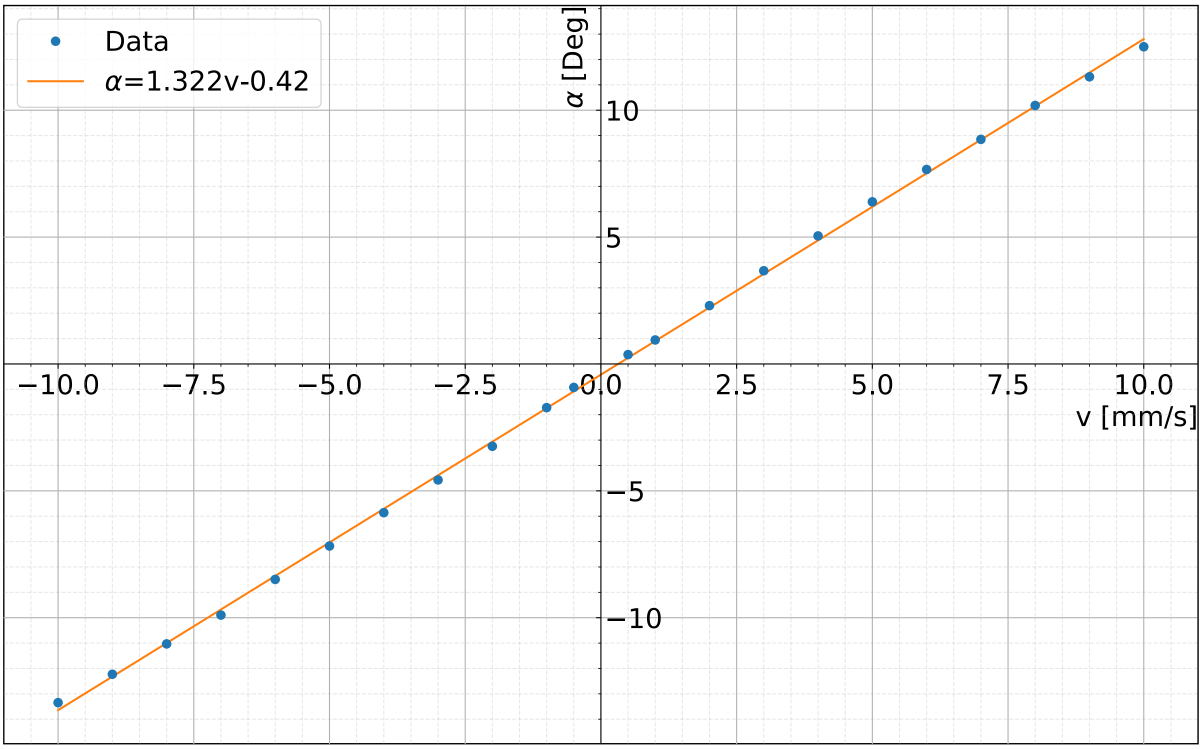

Figure D.2: Phase difference variation for speeds over 1 mm/s.

D.1 Doppler Effect

We decided to study the impact of the Doppler Effect on the system to ensure that the variations of α were not related to this effect.

As was mentioned on chapter 2 when considering the Doppler Effect the irradiance is proportional to:

$$I \propto I_0 \cos(2\pi(f_1 - f_2)t + \delta(t)) \tag{D.3}$$

Where f_1 represents the frequency of the measurement arm and f_2 the frequency of the reference arm. According to the Doppler Effect, if the stage is moving away from the interferometer with velocity v_s, f_2 can be related to f_1 by:

$$f_2 = \frac{c}{c + v_s} f_1 \tag{D.4}$$

In equation D.3 it is also important to notice that δ is a function of time because the number of fringes is directly related to the displacement of the stage, which can be represented as a function of the velocity using d=$v_s t$. So we have:

$$\delta(t) = \frac{N_f(t)}{2\pi} + \delta_0 = \frac{v_s}{\pi} \frac{n}{\lambda} t + \delta_0 \tag{D.5}$$

Where δ_0 represents the initial phase of the movement.

We can now rewrite equation D.3 as:

$$I \propto I_0 \cos\left[\left(2\pi \frac{v_s}{c + v_s} \frac{c}{\lambda} + \frac{v_s}{\pi} \frac{n}{\lambda}\right) t + \delta_0\right] \tag{D.6}$$

As we can see in equation D.6 there isn't a single term of v_s that does not depend on the time, so the Doppler effect does not justify a constant phase difference change with v_s. However, the new frequency of the signal is worth considering because of possible restrictions over the sampling frequency. For small velocities the frequency of the signal becomes:

$$f = \frac{1}{2\pi} \frac{2\pi^2 + n}{\pi\lambda} v_s \tag{D.7}$$

If we compare this new frequency with the criteria defined in equation 5.20 we can conclude that the sampling frequency criteria already imposed forces the sampling frequency to be almost 4 times bigger than the new frequency of the signal, this implies that there is no problem with the Doppler effect.

D.2 Further Studies With Higher Velocities

When calibrating the last translation stage, detailed in section 8.4, we had the opportunity of testing the interferometer's performance when the stage's velocity was as big as $100\,\mathrm{mm/s}$. To better characterize the α parameter's variation with the translation stage's velocity we measured 20 more velocities in order to confirm the linearity demonstrated in figures D.2 and D.1, the results are represented in figure D.3.

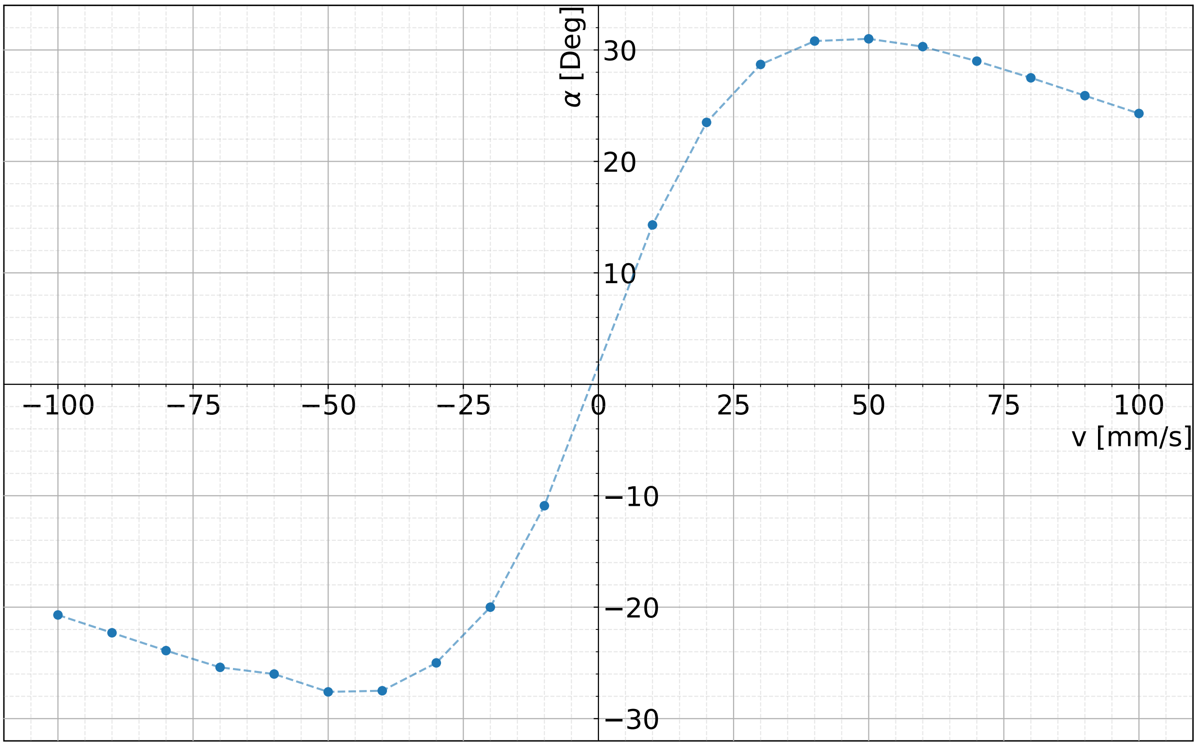

Figure D.3: Phase difference variation for speeds over 10 mm/s. We can now see that the phase difference variation is not linear with the velocity of the translation stage.

As we can see the phase difference variation is quasi-linear for velocities under 10 mm/s but the tests performed show that this variation is not at all linear, achieving a maximum value of 31° at 50 mm/s.

D.3 Conclusions

As we saw the cause of the phase difference variation with the velocity of the translation stages was not the Doppler Effect, after all the tests we placed the reference retroreflector on a translation stage and inverted the interferometer's arms, which also did not resolve the problem. Considering that some components that are altering the polarization undesirably, as was shown in appendix C, it is possible that the cause of this problem is related to these components, in particular with the beamsplitter because it is not specifically coated for 633 nm but is instead a broadband component.

Nonetheless, the changes in phase difference along the movement are not a problem with the way the signal processing is implemented, because as was shown in chapter 5 it is not necessary to have a phase difference of exactly 90° to achieve quadrature.